MINIMUM DETECTABLE ACTIVITY AS A FUNCTION OF DETECTOR SPEED

A Dissertation

by

JAMES T. FALKNER

Submitted to the Office of Graduate and Professional Studies of
Texas A&M University
in partial fulfillment of the requirements for the degree of

DOCTOR OF PHILOSOPHY

Chair of Committee,	Craig M. Marianno
Committee Members,	Dylan A. Shell
	John Ford
	Sunil S. Chirayath
Head of Department,	Yassin A. Hassan

May 2018

Major Subject: Nuclear Engineering

ABSTRACT

A radiation detector's sensitivity is important when designing survey plans. A measure of sensitivity is minimum detectable activity (MDA) which is the lowest amount of activity required for a signal to be distinguished above background. It has been known for some time that the efficiency of a moving detector can be improved by slowing the speed of travel. This decreasing efficiency at higher speeds results in higher MDAs and thus less sensitive detectors. The effect of speed on detector efficiency was mentioned in the Multi-Agency Radiation Survey and Site Investigation Manual (MARSSIM). However, the relationship between speed and efficiency was not quantified in this manual. This research derived this relationship by modeling detector efficiency as a function of detector travel speed and fitting a modified four parameter logistic function (M4PL) to the data. The M4PL function was then verified in a controlled laboratory setting using a 2 x 2 in sodium iodide (NaI) detector at speeds between 20-120 cm s^{-1} and in a parking lot using a 2 x 4 x 16 in NaI detector at speeds between 10-40 mph. Finally, the M4PL function was validated using a priori gathered gamma radiation survey data from two aerial systems. The M4PL function begins with a region of relatively high detector efficiency and ends with a region of relatively low detector efficiency. In between is a transition region of decreasing detector efficiency. This decrease is gradual within initial speeds but, quickly steepens, and then shallows out at higher detector speeds. This general shape was observed for all modeled systems. The M4PL function was used to develop a relationship between speed and MDA. There are three uses of the M4PL function. The first is to verify the accuracy of current survey plans. The second is to optimize survey plans for speed and accuracy. The third is to identify the limits of detection accuracy based on operational speed. This foundational relationship between detector speed and detection efficiency has the potential to improve detector performance in various applications for both the academic and operational fields.

DEDICATION

For Dad

ACKNOWLEDGMENTS

I would like to first thank Dr. Marianno for his unwavering enthusiasm in completing this degree in the very short time-frame the Navy allowed me. From my very first conversation with him to the final push to defend his only attitude was "Hell Yeah! Let's do this!" A special thank you to Matt Grypp. He was the person that introduced me to Dr. Marianno, and without his implicit endorsement I'm sure Dr. Marianno's enthusiasm would not have been so effusive. Thank you to my committee for providing feedback along the way.

I would also like to thank the Navy for allowing me this opportunity and funding my tuition. Thank you to CAPT John Cardarelli in the CBRN Consequence Management Advisory Division at the Environmental Protection Agency and Dr. Piotr Wasiolek in the Aerial Measuring System group at the Remote Sensing Laboratory for providing field data to test my findings. Thank you to the ASPECT team for allowing me to fly with you and see how the aerial data sausage is made.

Thank you to Derek and Matt in Radiation Safety at A&M. Their assistance in getting permission to run experiments and then carry those experiments out was invaluable. Thank you to Dr. Evans Kitcher for helping me optimize the MCNP simulations. Especially thank you to Katie, Rainbow, and Barb for helping me gather field data.

Finally and most importantly thank you to my wife, Pamela. Those that have done this before with a family know what a truly supportive spouse means to accomplishing your academic goals. Without a doubt her love, support, and encouragement were vital during this process. Whether it was taking the kids to the park so I could work in peace, staying up late and editing with me, or even just kicking me out of bed in the morning she was there every step of the way.

CONTRIBUTORS AND FUNDING SOURCES

Contributors

This work was supported by a dissertation committee consisting of Professors Craig Marianno, advisor, Sunil Chirayath, and John Ford of the Department of Nuclear Engineering and Professor Dylan Shell of the Department of Computer Science and Engineering.

The data collected for Chapter 4 was provided in part by Captain John Cardarelli of the Environmental Protection Agency and Dr. Piotr Wasiolek of the Remote Sensing Laboratory.

All other work conducted for the dissertation was completed by the student independently.

Funding Sources

This work was supported by Navy Medicine Professional Development Center as part of my Duty Under Instruction program.

Disclaimers

The views expressed in this article reflect the results of research conducted by me and do not necessarily reflect the official policy or position of the Department of the Navy, Department of Defense, nor the United States Government.

I am a military service member of the United States government. This work was prepared as part of my official duties. Title 17 U.S.C. 105 provides that 'copyright protection under this title is not available for any work of the United States Government.' Title 17 U.S.C. 101 defines a U.S. Government work as work prepared by a military service member or employee of the U.S. Government as part of that person's official duties.

NOMENCLATURE

AMS	Aerial Measuring System
ASPECT	Airborne Spectral Photometric Environmental Collection Technology
DOE	Department of Energy
EPA	Environmental Protection Agency
M4PL	Modified Four Parameter Logistic Function
MARSSIM	Multi-Agency Radiation Survey and Site Investigation Manual
MCS	Multi Channel Scaler
MDA	Minimum Detectable Activity
MDC	Minimum Detectable Concentration
NaI	Sodium Iodide
RPM	Radiation Portal Monitor
RSL	Remote Sensing Laboratory

TABLE OF CONTENTS

Page

LIST OF FIGURES

FIGURE Page

LIST OF TABLES

TABLE Page

1. INTRODUCTION

1.1 Motivation

Radiation detectors are used in several applications, many of which often involve a dynamic source-detector geometry. Traditional applications range from decontamination and decommissioning of commercial facilities to the screening of nuclear medicine patients. Increasingly, they are being used for the search for illicit material through the use of radiation portal monitors (RPMs) and roving vehicle detectors. As detectors were increasingly used on mobile platforms it was noticed that detector efficiency would decline as detector speed increased. Trade-offs in detector design must be made between performance, cost, and ease of use. A detector can be inexpensive to build and perform sweeps in a short time-frame but have questionable results; can perform sweeps quickly with very accurate results but be prohibitively expensive to construct; or can be inexpensive to build and have a high accuracy but require prohibitively long survey times. A measure of a detector's sensitivity is its minimum detectable activity (MDA). The motivation for this research was to derive a function between a detector's speed and its achievable MDA. This relationship will then allow surveyors to tailor their survey plans or purchase the appropriate detector to meet their mission objectives.

1.1.1 MARSSIM

The concept of detector sensitivity was addressed in the industry standard for performing site surveys, the Multi-Agency Radiation Survey and Site Investigation Manual (MARSSIM), (U.S. NRC, 2000). MARSSIM describes a scanning technique for assessing survey-site contamination and calculating a detector's minimum detectable concentration (MDC) based on those scan parameters. Here MDC and MDA are synonymous. The scan is conducted at a set speed by the surveyor with the detector maintained at a defined height above the surface for the duration of the survey. With this information detector efficiency can be calculated and a MDC for

that survey deduced. The efficiency of the detector used is assessed by obtaining a static count of a reference source. MARSSIM's efficiency variables include detector size (probe area) and source-to-detector distance and source geometry, (U.S. NRC, 2000). Each of these effect the solid angle of the detector and are influenced by a detector's speed.

MARSSIM obtains MDC by using a conversion factor, C, that is a function of a detector's area and efficiency. It discusses scanning sensitivity as a surveyor's ability to detect predetermined levels of contamination. It does not explicitly define MDC in terms of a variable efficiency but does state that detection sensitivity "can be improved by 1) selecting an instrument with higher detection efficiency or a lower background [such as through the use of shields], 2) decreasing scanning speed, and 3) increasing size of the effective probe area." Only the second improvement is a reference to a variable MDC as a function of speed. This effect is not quantified thus surveyors are left to trial and error to determine the best speed to conduct their surveys. This research derived a mathematical expression for a detector's efficiency as a function of its travel speed.

1.2 Previous Work

1.2.1 Addressing MDA Changes Via Integration Times

Schroettner et.al. investigated the detector sensitivity as a function of source travel speed by experimentally determining a relationship between the speed of a moving source and the integration time for static RPMs (Schroettner et al., 2009). In this case a source was first shuttled past a single detector and then later multiple detectors at various constant speeds. Speeds chosen ranged from 1 to 50 m s^{-1} and approximated the speeds at which a train might pass through the monitor. The aim of their research was to develop a way to calculate the optimal detector integration time to achieve the lowest MDA based on the speed of the source, Fig. 1.1.

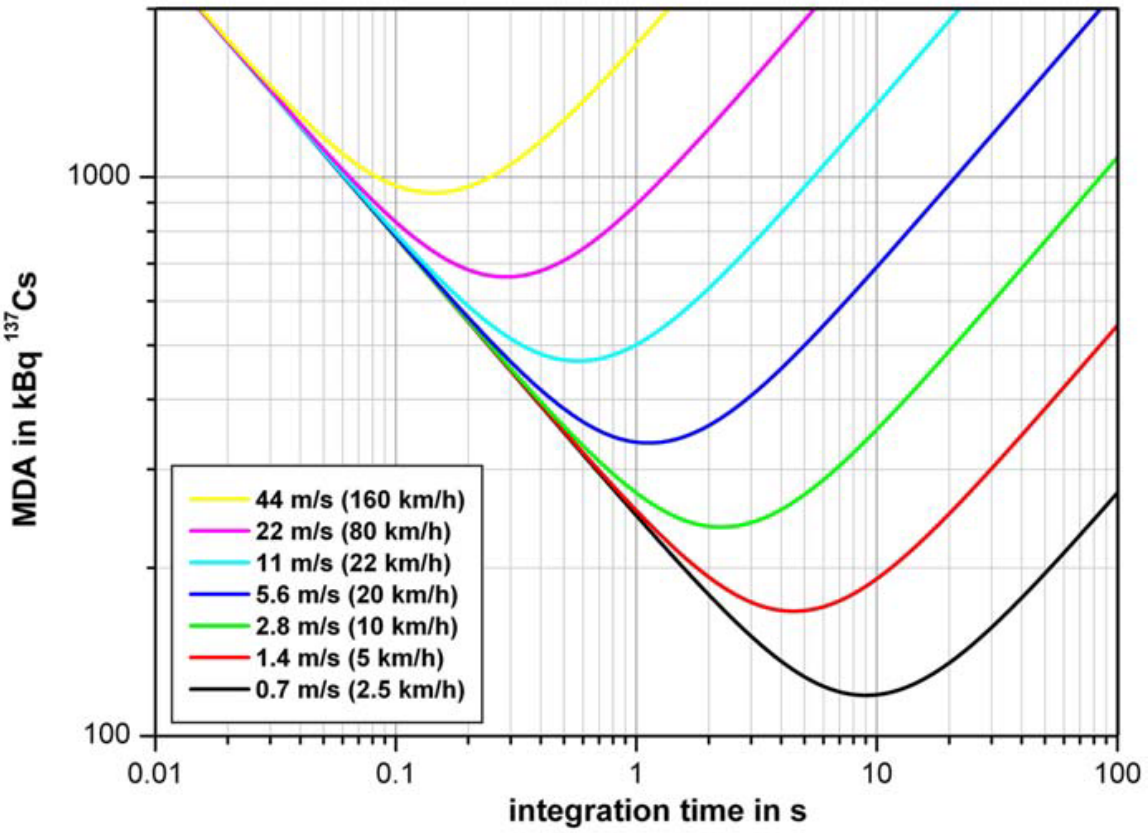

Figure 1.1: MDA depending on the integration time (off axis distance 2.5m) (Schroettner et al., 2009). Reprinted from Applied Radiation and Isotopes, 67(10), Schroettner, T., Kindl, P., and Presle, G., "Enhancing Sensitivity of Portal Monitoring at Varying Transit Speeds", 1878-1886, 2009 with permission from Elsevier.

The approach in Schroettner is very similar to this present research, however their correction method for speed effects is very different. Schroettner chose to alter the integration time of the detection system to maximize detection efficiency, Table 1.1. This is undesirable for two reasons. First, the ability to change integration time, either automatically or by the operator, must be manually coded into the detection system's software. Second, the speed of the object being surveyed must be assessed and again input manually into the detection system. This approach of changing integration time based on each counting scheme, although technically feasible, is needlessly complicated.

Table 1.1: Dependence of the MDA on the integration time at various speeds. Reprinted with permission from Schroettner et al., 2009.

Speed		MDA in kBq depending on the integration time							
km h^{-1}	m s^{-1}	10 ms	25 ms	50 ms	100 ms	250 ms	500 ms	1 s	3 s
5	1.4	440	278	196	140	91	71	64	81
10	2.8	440	278	198	142	100	90	100	156
20	5.6	440	280	201	151	127	141	182	305
50	14	318	288	223	200	239	318	442	761
80	22	446	302	256	266	363	500	703	1215
100	28	450	315	283	314	449	314	886	1521
160	44	465	362	376	468	708	994	1403	2430

1.2.2 Modeling Scan MDCs

Alecksen and Whicker extended the MARSSIM approach to calculate MDCs for various combinations of detectors, source materials, and source geometries (Alecksen & Whicker, 2016). Their work comprised modeling a detector as it passed over a source placed in soil, Fig. 1.2. They then calculated the detector's total efficiency. The results for their simulations are collected in a database they maintain and which are freely available for download.

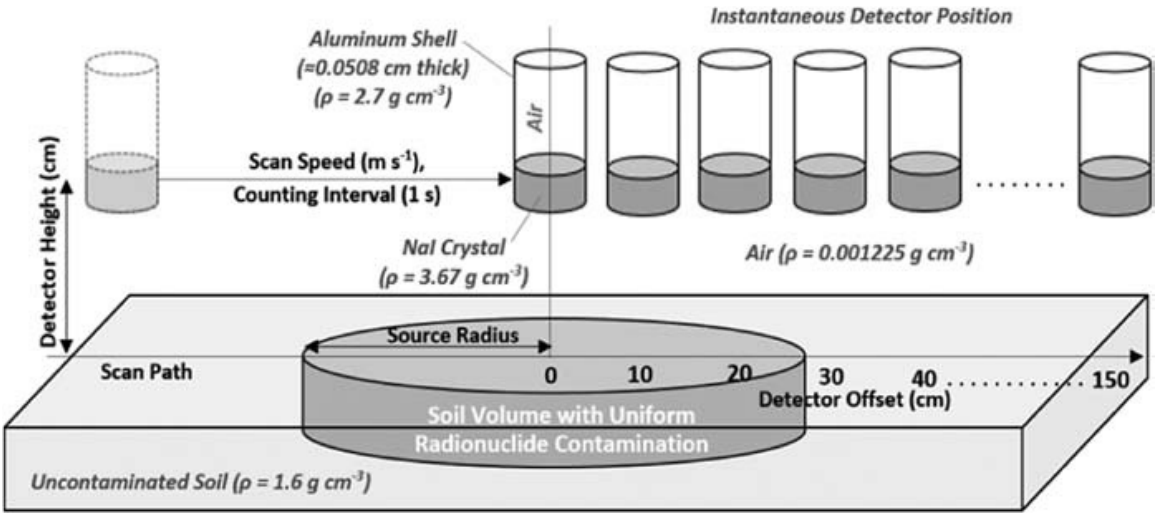

Figure 1.2: Conceptual parameters, assumptions and geometries used to model the total integrated counting efficiency of a NaI detector while scanning over a contaminated volume of soil. Reprinted from Health Physics, 111(2), Alecksen, T., and Whicker, R., "Scan MDCs for GPS-Based Gamma Radiation Systems", S123-S132, 2016 with permission from Wolter Kluwer Health, Inc.

Their effort, while extensive across multiple configurations of sources and detectors, was only conducted for one speed, 1.5 m s^{-1}. This does not address the phenomenon of decreasing efficiency with increasing speed. Another shortcoming of Alecksen's research is that it was not experimentally verified or tested against field data.

1.2.3 Efficiency Vs. Speed Depicted

An example of the decrease in efficiency as speed is increased is provided by Marianno et al., (Marianno, Higley, & Palmer, 2000; Marianno, 2015). This work consisted of modeling a Field Instrument for the Detection of Low Energy Radiation (FIDLER) response, gathering data from the detector in experiments, and then comparing the two together to show the real world operates in much the same way that the modeling world works. His results show a decreasing trend in efficiency with increasing speed, Fig. 1.3. He modeled the FIDLER passing over a ^{241}Am source at different speeds and with the source at different depths within soil. All trend lines show an

initially rapid decrease that shallows out around 50 cm s^{-1} to a flat profile. The trend is similar at all depths modeled but the influence of depth is beyond the scope of this current research.

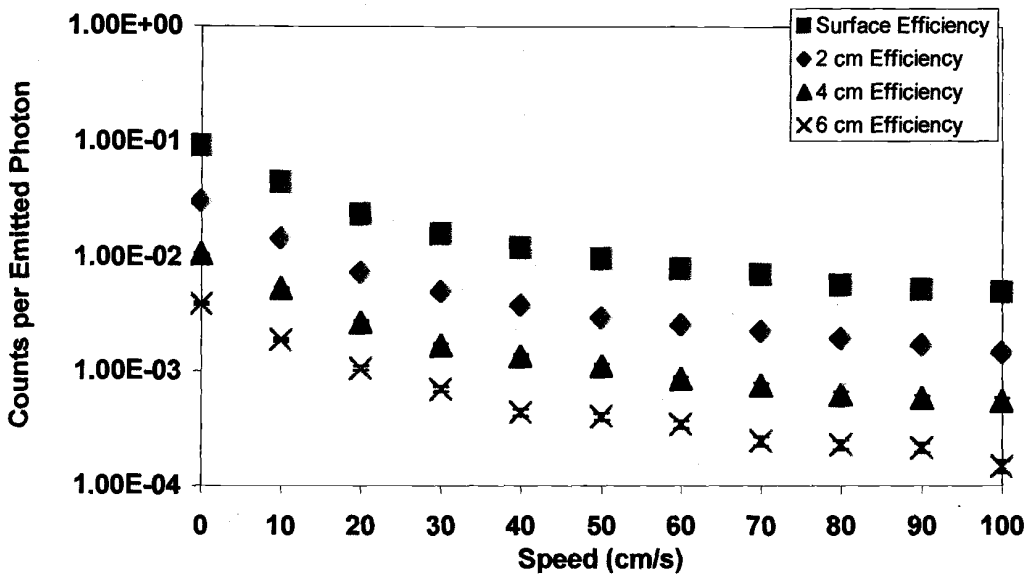

Figure 1.3: Theoretical FIDLER scanning efficiency for a point source as a function of depth and scanning speed. As speed increases, efficiency decreases. Reprinted from Marianno, C., Higley, K., and Palmer, T., 2000.

The reason for this trend is hinted at in further results in his work, Fig. 1.4. He modeled the same detector over the same source (and source depths) as their moving detector but in static configurations at defined offsets away from the source. The trend is for the efficiency to decrease as the detector is moved away from the source, and for that decrease to sharpen the farther from the source the detector is moved. This implies that it is the detector/source orientation that is critical in determining the efficiency/speed relationship. The fraction of a count's integration time the detector will spend near the source decreases as the speed of the detector increases and result in successively smaller fractions of photons to be incident upon the detector.

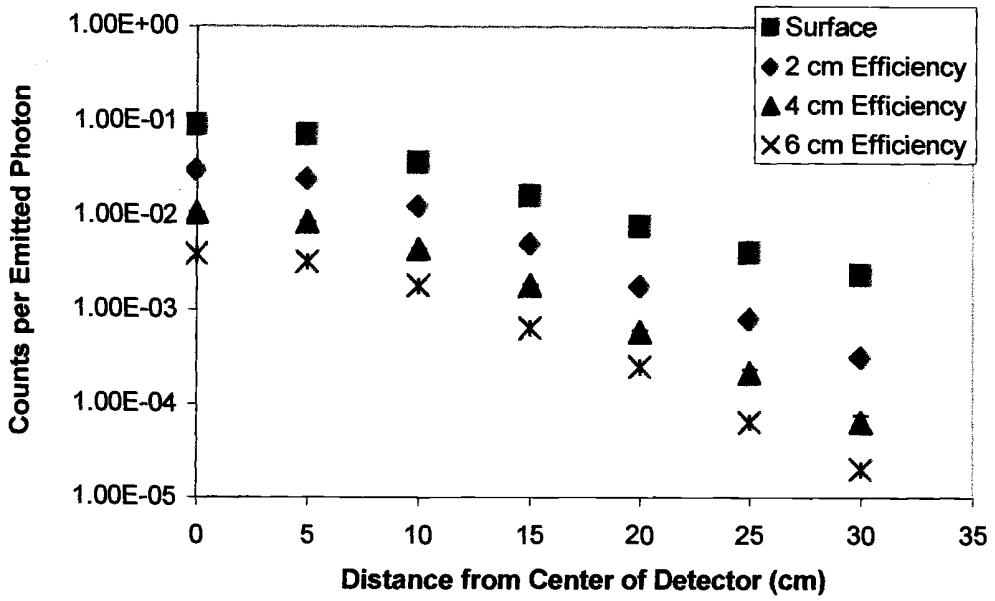

Figure 1.4: FIDLER theoretical static detection efficiency for 60 keV photons as a function of depth and distance. For a point source, as depth and distance from the detector increases, detection efficiency rapidly decreases. Reprinted from Marianno, C., Higley, K., and Palmer, T., 2000.

Experimental FIDLER results were then compared to simulated results (Marianno, 2015). Both data sets show a decrease in efficiency correlated with an increase in detector speed, as expected. In all cases the simulation results are approximately 10% higher than the experimental results, Fig. 1.5. Marianno attributes this difference to signal processing. With the exception of the 20 cm and 30 cm data points, all results are within two standard deviations of each other. Marianno proposed that the reason for the difference at those offsets is the topographical influence in source placement with 60 keV photons being easily attenuated by soil. The source prevented consistent distancing in source placement as found in the simulation. Additionally, ground irregularities resulted in the source being placed on the backside of a small mounds of soil which provided a small amount of shielding when the detector was in certain locations.

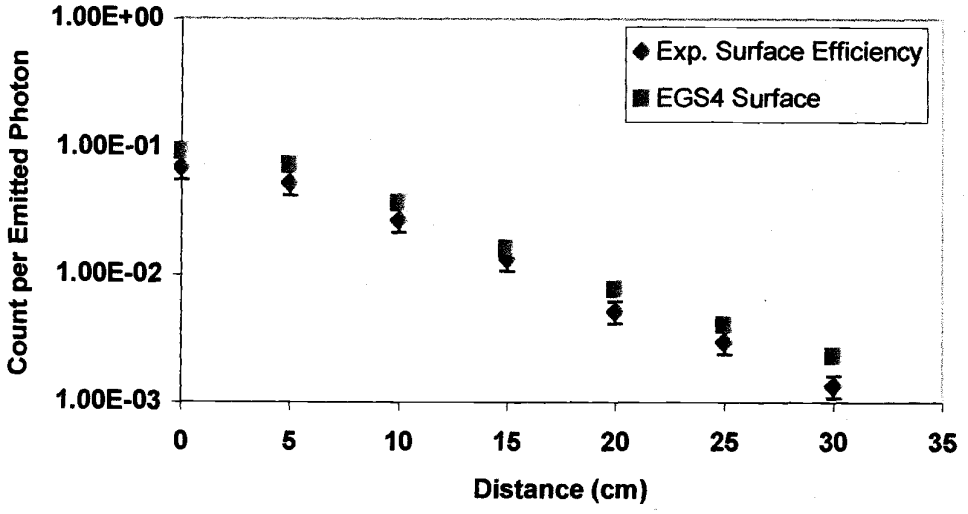

Figure 1.5: FIDLER experimental and theoretical detection efficiencies for a 60 keV photon surface source as a function of distance. The theoretical and experimental results match well with one another. Reprinted from Health Physics, 109, Marianno, C., "Signal Processing and its Effect on Scanning Efficiencies for a Field Instrument for Detecting Low-Energy Radiation", 78-83, 2015, with permission from Wolter Kluwer Health, Inc.

The experimental results are lower than the model results for moving detectors due to signal processing but show the same general trend, Fig. 1.6. Error bars for the model results are inside the markers. The decrease is not linear but starts out sharply and then tapers off to a flat level. This relationship was not quantified.

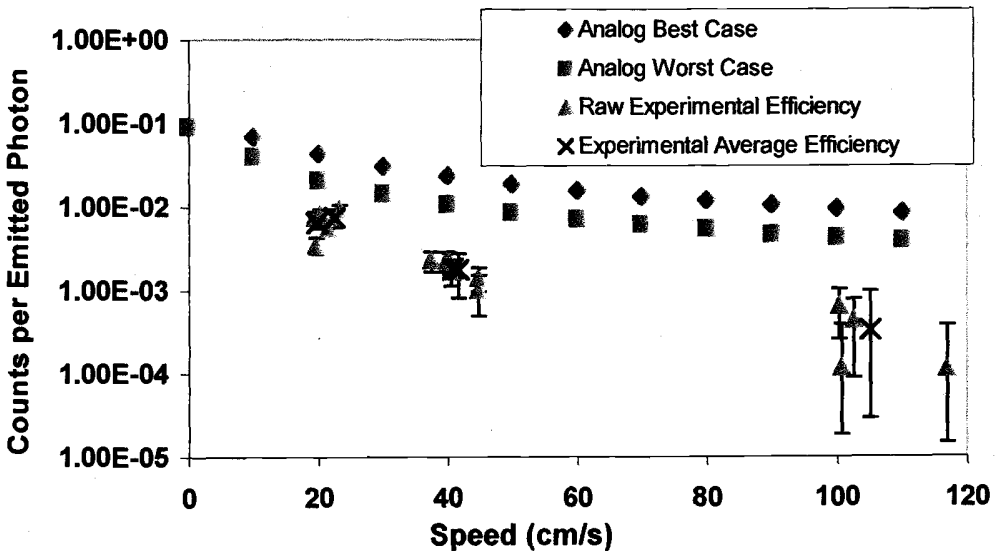

Figure 1.6: FIDLER scanning efficiency for 60 keV photon surface source as a function of speed. As speed increases the scanning efficiency of the FIDLER decreases. Theoretical results, which base their efficiency on analog methods, are higher than experimental efficiencies resulting from signal processed data. Reprinted from Health Physics, 109, Marianno, C., "Signal Processing and its Effect on Scanning Efficiencies for a Field Instrument for Detecting Low-Energy Radiation", 78-83, 2015, with permission from Wolter Kluwer Health, Inc.

1.3 Define Terms

1.3.1 MDA

The desired quantity MDA, or that amount of activity of a particular radioactive substance which can be detected above background, can be calculated by a simple conversion, Eq. 1.1 (Knoll, 2010).

$$MDA = \frac{L_D}{Y\epsilon T}, \tag{1.1}$$

Here L_D is the detection limit of the environment in which the count occurs, Y is the photon yield of a particular radionuclide, ϵ is the efficiency of the detector, and T, integration time, is

the length of time the detector sums signals to produce a count usually dictated by the survey design. A typical integration time in mobile detection systems is 1 s. For the purposes of this research the radionuclide selected for study was ^{137}Cs with a yield of 0.85 per disintegration and integration times were either set at 1 s or normalized to 1 s. The parameters L_D and ϵ are discussed further below.

1.3.2 Limits of Detection

The MDA of a counting system was quantified by Currie for radio-chemistry (Currie, 1968). Prior to experiments being conducted, the researcher chooses the acceptable level of two types of errors: 1) determining the presence of a signal when there is none, "false positive", α and 2) determining the absence of a signal when a source is present, "false negative", β. These values do not have to be the same, however a typical value for both is 5%.

Using these values a critical level, L_C, and determination level, L_D, can be calculated, Eq. 1.2. Here σ_0 and σ_D are the standard deviations assuming radiation is and is not present, respectively. L_C is the critical level, defined as that number of counts above which a source is present. L_D is the detection limit, defined as that number of counts above which the detector will reliably detect a source. A third limit, quantification limit (L_Q), is the limit above which the amount of material present can be quantified. It is not considered in this research and thus is not discussed here. The limits and their relation to α and β are shown in Fig. 1.7.

$$\begin{aligned} L_C &= k_\alpha * \sigma_0 \\ L_D &= L_C + k_\beta * \sigma_D \end{aligned} \tag{1.2}$$

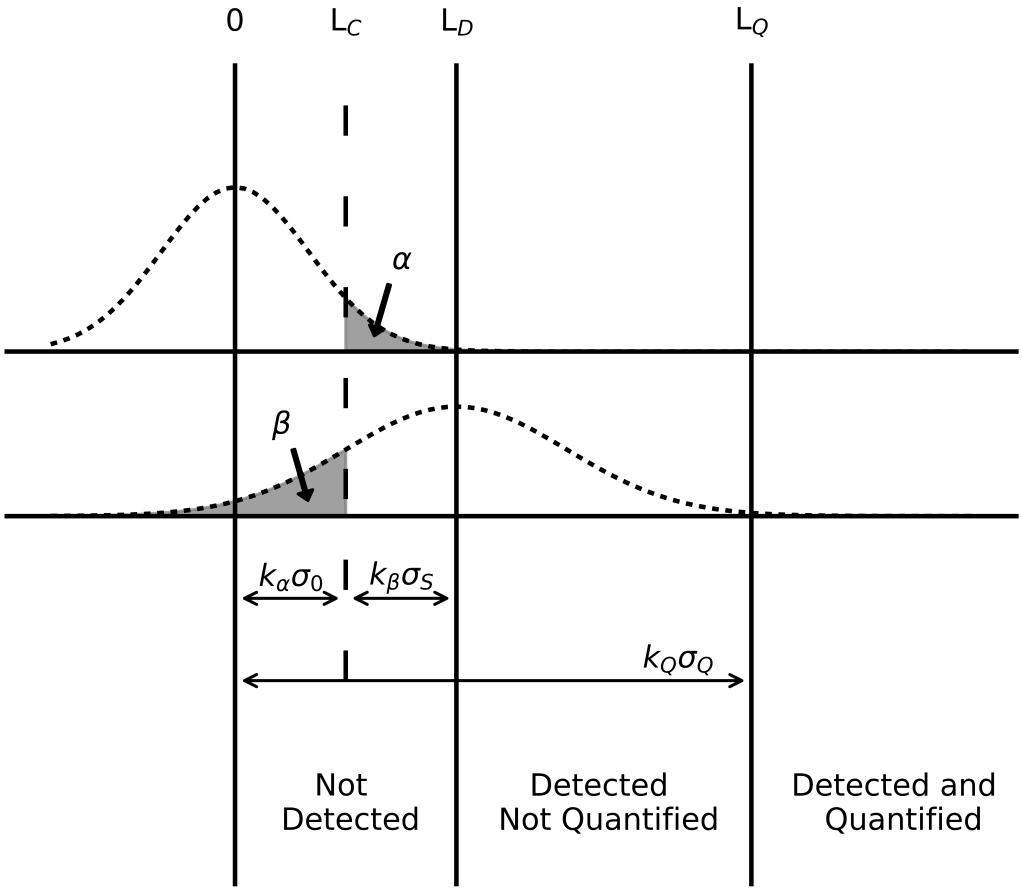

Figure 1.7: Scheme to explain the various measurement limits. Reprinted from Analytical Chemistry, 40(3), "Limits for Qualitative Detection and Quantitative Determination", 586-593, 1968, with permission from the American Chemical Society.

When k values corresponding to 5% errors are used and the source present is considered to be nearly equal to background the detection level becomes $L_D = 4.65\sigma_B + 2.71$ which is known as the "Currie Equation". The concept is applied to gross counts but can be extended to energy bins if a multichannel analyzer is used to gather count data. This is particularly useful when attempting to measure the presence of suspected radionuclides. However, in most cases the reason for analysis is not to determine the amount of radiation but to identify the amount

of the radionuclide that is producing the radiation. The Currie Equation was the basis for all detection limits used in this research.

1.3.3 Efficiency (Total, Geometric, Intrinsic)

Total detector efficiency is the ratio of photon interactions in a detector to photons emitted by a source, Eq. 1.3. It is made up of two components, intrinsic efficiency and geometric efficiency. Intrinsic efficiency is the ratio of photons interacting in the detector to photons striking the detector, ϵ_{I}. Geometric efficiency, ϵ_{G}, is the ratio of photons striking the detector to photon emitted by a source. The fraction of photons striking a detector can be calculated from the solid angle, Ω, which is a function of source/detector configuration, Fig. 1.8.

$$\epsilon_T = \epsilon_G * \epsilon_I = \frac{\text{photon strikes}}{\text{photons emitted}} * \frac{\text{photon interactions}}{\text{photon strikes}} \tag{1.3}$$

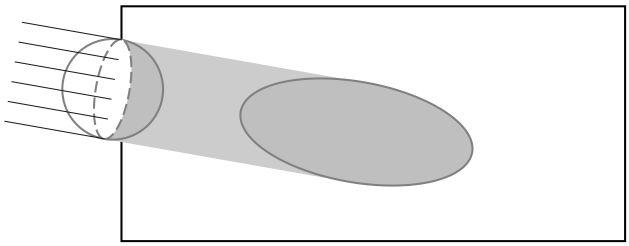

Figure 1.8: Schematic showing what solid angle represents.

Solid angle is the angle an object subtends from an observer at the center of an imaginary sphere containing both the observer and the object. The solid angle depends on the shape of the object and the distance between the observer and object. As the object moves past the observer its solid angle will first increase to a maximum and then decrease, Fig. 1.9. In this research the source is the observer and the detector is the object.

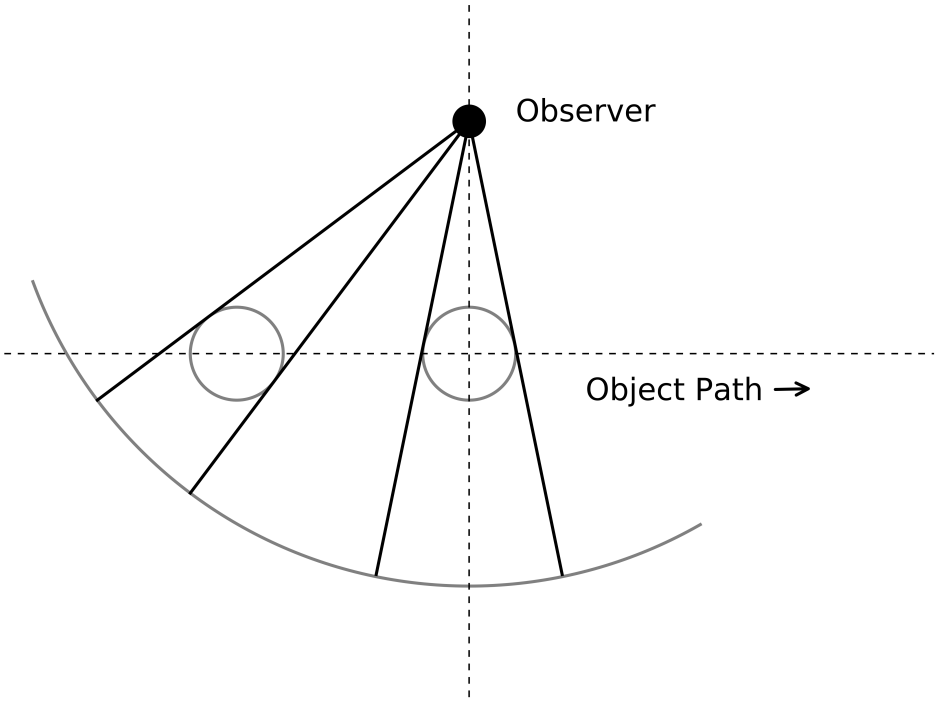

Figure 1.9: Schematic showing the different solid angles an object presents as it moves past an observer.

1.4 Research Objective

This research determined how the speed of a detector relative to a source affects detection efficiency. This work included modeling various source/detector arrangements, laboratory tests with well constrained experimental parameters, and testing against field data to account for real world confounders. This research sought to create a tool for surveyors to 1) validate already designed survey plans, 2) produce a method for determining either ideal detector speed based on required precision, as in the case of meeting regulatory requirements, or 3) produce a method of calculating the MDA based on detector speed as constrained by operational requirements such as those found in the case of mobile detectors for security sweeps.

This research was organized as below. The robot experiments were done in a laboratory so that confounders such as variable background or nuisance sources could be minimized and that detection scheme parameters such as detector speed and orientation could be tightly controlled. The vehicle experiments were done in a field to bridge controlled experiments with real world environments. A conclusion ties the research together and outlines ways in which this work can be used.

1. Simulate the detection system and develop a model that describes the relationship
    1.1. Establish a link between a detector's solid angle and its efficiency
    1.2. Establish a link between a detector's efficiency and its speed
    1.3. Identify a model that explained the relationship between efficiency and speed
2. Verify under controlled laboratory conditions that the relationship holds for the modeled detection system
3. Test this relationship against data collected in real world surveys
4. Identify constraints on the relationship

2. MODELING MINIMUM DETECTABLE ACTIVITY AS A FUNCTION OF DETECTOR SPEED

2.1 Introduction

Previous research has shown that a detector's efficiency varies with increasing speed, (Marianno et al., 2000; Marianno, 2015). Although noted in research, and even discussed in the Multi-Agency Radiation Survey and Site Investigation Manual (MARSSIM), this effect has never been quantified, (U.S. NRC, 2000). Understanding this effect on radiation detectors will improve environmental surveys (Whicker, Cartier, Cain, Milmine, & Griffin, 2008; Abelquist & Brown, 1999; Altshuler & Pasternack, 1963). It can also be used in security applications to help determine whether detection systems are appropriate for the operational constraints to which they are held, (Pöllänen et al., 2009; Lepel, Geelhood, Hensley, & Quam, 1998; Runkle, Mercier, Anderson, & Carlson, 2005; De Geer, 2004; Ayaz-Maierhafer & DeVol, 2007). Knowing how speed effects detector efficiency could even be used in medical physics to improve count times thereby reducing stress on patients and allowing for increased throughput of radiological clinics, (Kramer, Burns, & Guerriere, 2002; Warner & Oliver, 1966).

This research modeled a simple right circular cylinder detector to derive a relationship between the detector's speed and its efficiency. The right circular cylinder was chosen as it is the shape of the standard sodium iodide (NaI) detector used to compare the performance of all other scintillator detectors.

One method of assessing a detector's performance is to calculate its reportable minimum detectable activity (MDA), Eq. 2.1. MDA is that amount of activity required to be detected above background. The components of Eq. 2.1 are yield Y, integration time T, limit of detection L_D, and efficiency ϵ. Emission yield converts the activity of the source present to the number of emitted particles/photons. Integration time is the amount of time that the detector is recording

a signal to produce a count. Detection limit is a function of the background field in which the count is made.

$$MDA = \frac{L_D}{Y\epsilon T}, \tag{2.1}$$

A detector's total efficiency is dependent on its intrinsic efficiency (detector properties) and its geometric efficiency (solid angle), Eq. 2.2. The detector properties do not change under typical survey conditions. The aim of this research was to derive a relationship showing how a detector's speed impacts its geometric efficiency. The number of photons striking a detector, ϵ_{G}, can be calculated from the solid angle, Ω, which is a function of source/detector geometry, Fig. 2.1. Understanding this relationship, allows survey plans to be better optimized based on regulatory, operational, and/or economic requirements.

$$\epsilon_T = \epsilon_G * \epsilon_I = \frac{\text{photons striking}}{\text{photons emitted}} * \frac{\text{photons interacting}}{\text{photons striking}} \tag{2.2}$$

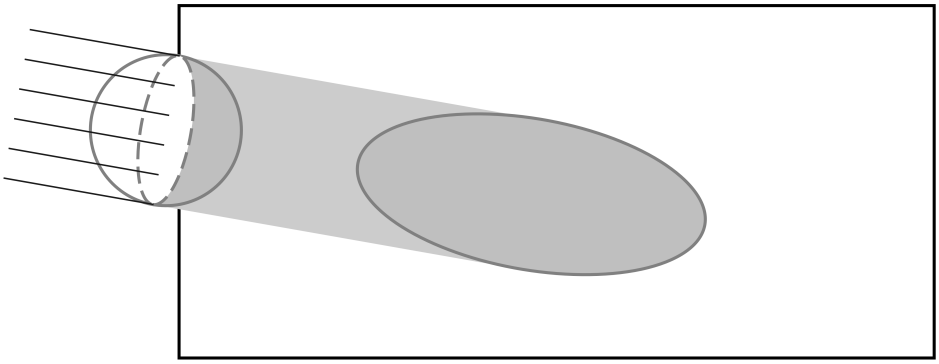

Figure 2.1: Schematic showing what solid angle represents.

Solid angle is the angle an object subtends from an observer at the center of an imaginary sphere containing both the observer and the object, Fig. 2.2. The solid angle depends on the shape of the object and the distance between the observer and object. In this research the source is the observer and the detector is the object. A detector system records a signal over a set period of time (integration time) and reports the summed value (count). The detector's total efficiency is calculated as this count divided by the total emission during the integration time.

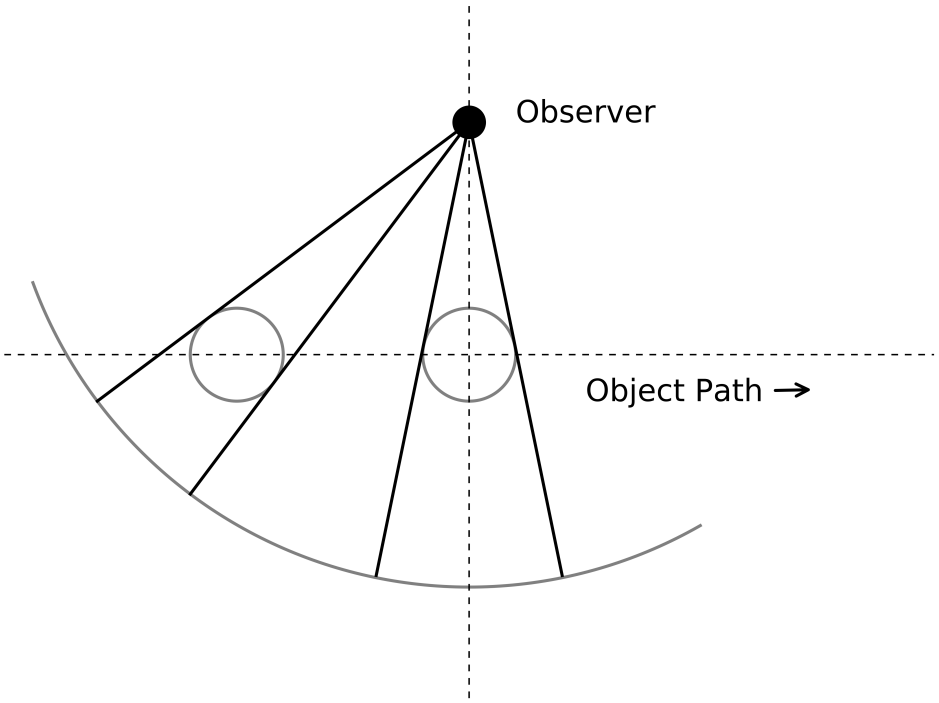

Figure 2.2: Schematic showing the different solid angles an object presents as it moves past an observer.

Masket (1956) derived equations to calculate the solid angle at various positions around a right circular cylinder, Eq. 2.3. Masket chose a right circular cylinder because it is the shape of the industry standard scintillation detector. Masket divided the space around the detector into three regions where Eq. 2.3 is applied in different combinations, Fig. **??**. For example, if the source is located in region I, Ω_1(r,h) would be calculated by referring to Eq. 2.3a. Masket constructed his equations in units of detector radius so that they could be applied to different cylinder sizes, the only modification being that source height and offset need to be accounted for

using the normalized unit. In Eq. 2.3, ρ is the source distance away from the cylinder axis, z is the source height above the reference plane defined as the top of the cylinder, S_1 and S_2 are rays from the source to the farthest and closest point on the detector, respectively, and ϕ is the angle swept across the detector face.

$$\Omega_1(\rho, z) = 2\pi - 2z \int_0^{\pi} \frac{d\phi}{\sqrt{z^2 + S_1^2}} \tag{2.3a}$$

$$\Omega_2(\rho, z) = 2z \int_0^{\arcsin(1/\rho)} [(z^2 + S_2^2)^{\frac{-1}{2}} - (z^2 + S_1^2)^{\frac{-1}{2}}]\, d\phi \tag{2.3b}$$

$$\Omega_3(\rho, z) = 2z \int_0^{\arcsin(1/\rho)} (z^2 + S_2^2)^{\frac{-1}{2}}\, d\phi \tag{2.3c}$$

$$S_1, S_2 = \rho \cos\phi \pm \sqrt{1 - \rho^2 \sin^2\phi} \tag{2.3d}$$

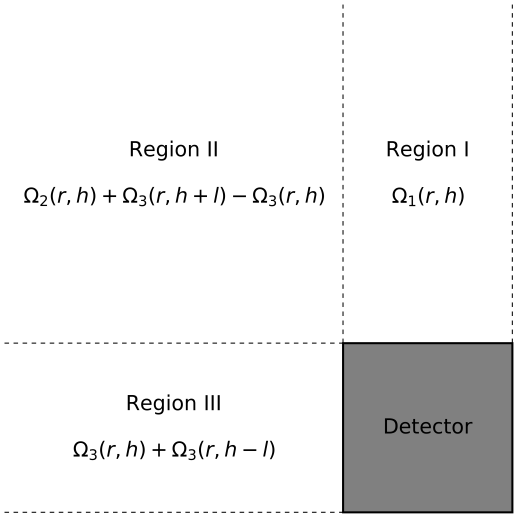

Figure 2.3: Schematic showing the different solid angles an object presents as it moves past an observer.

2.2 Methods and Materials

This research bridged the gap between Masket's solid angle equations for stationary sources and the proposed effect of detector speed on efficiency. This research consisted of Python calculations and MCNP simulations. Masket's solid angle equations were coded using Python 3.6.1, (Rossum, 2017). Detector efficiency was simulated using MCNP6.1, (Goorley et al., 2012). For this research all values were reported to six decimal places in keeping with Masket's precision.

Twenty point source locations around the detector were chosen for evaluation. Five of the points were example locations from Masket's original report used to illustrate his process. Five of the points were arrayed vertically between 1-5 detector radii away from the top face. These were chosen to depict the change in solid angle in region I as a function of distance from the reference plane. Five of the points were arrayed horizontally between 1-5 detector radii away from the middle of the side face. These were chosen to depict the change in solid angle in region

III as a function of distance from the detector side. Five of the points were arrayed horizontally between 1-5 detector radii offset from the detector corner. These were chosen because to depict the change in solid angle in region II as a function of distance from the top and side of the detector. The points in region II also depict a similar solid angle profile as that modeled for the line sources. The ρ and z values for the point sources modeled are listed in Table A.2 and shown in Fig. 2.4. All twenty point source locations are found directly in Masket's table of results and were chosen to verify the accuracy of the Python script.

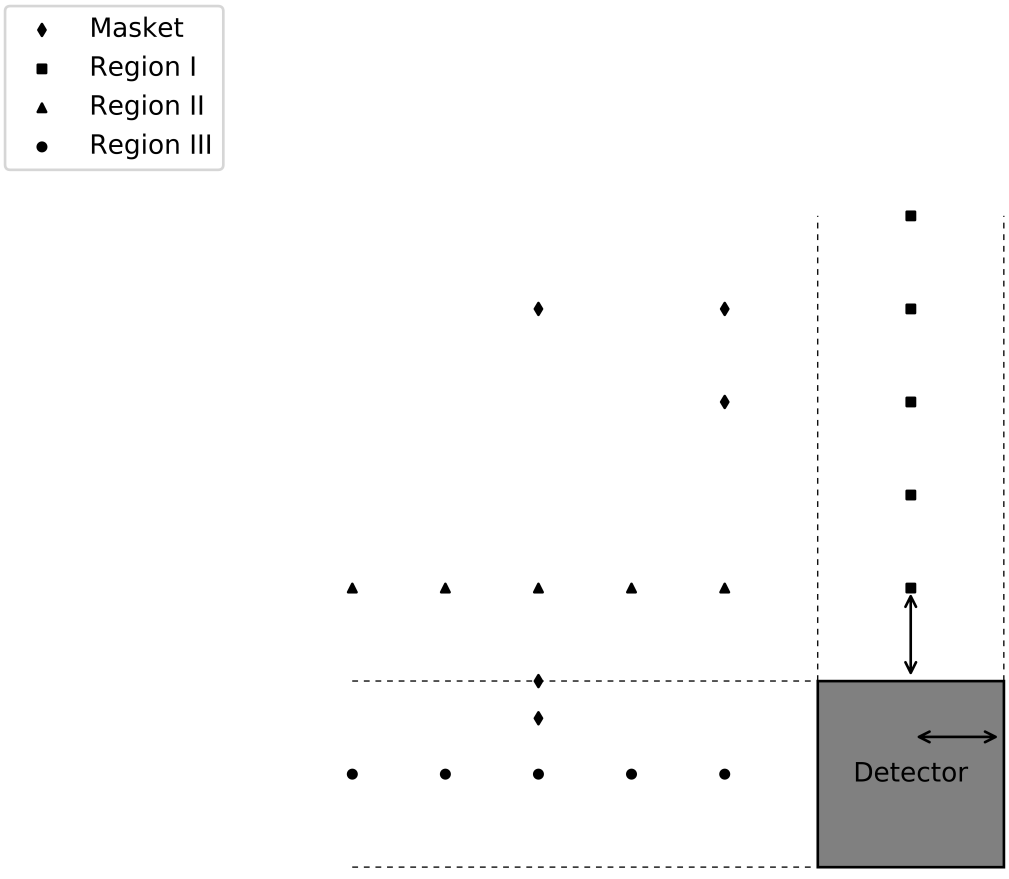

Figure 2.4: Schematic showing the different solid angles an object presents as it moves past an observer.

Line source configurations were modeled at 10 cm centered above the top face of the detector, Fig. 2.5. Line sources were used to approximate a moving detector over a stationary source because the MCNP version used does not model dynamic configurations. A line source emits photons with equal probability along the entire length of the source. In this way the tally response approximates the detector moving past the stationary source. The length of the line source is equal to the distance the detector would have traveled during the integrated period of interest. For these simulations an integration time of one second was used. Velocities simulated were between 10-100 cm s^{-1} in increments of 10 cm s^{-1}. These represent the best case scenarios for count configurations where the integration time occurs such that the detector is centered over the source.

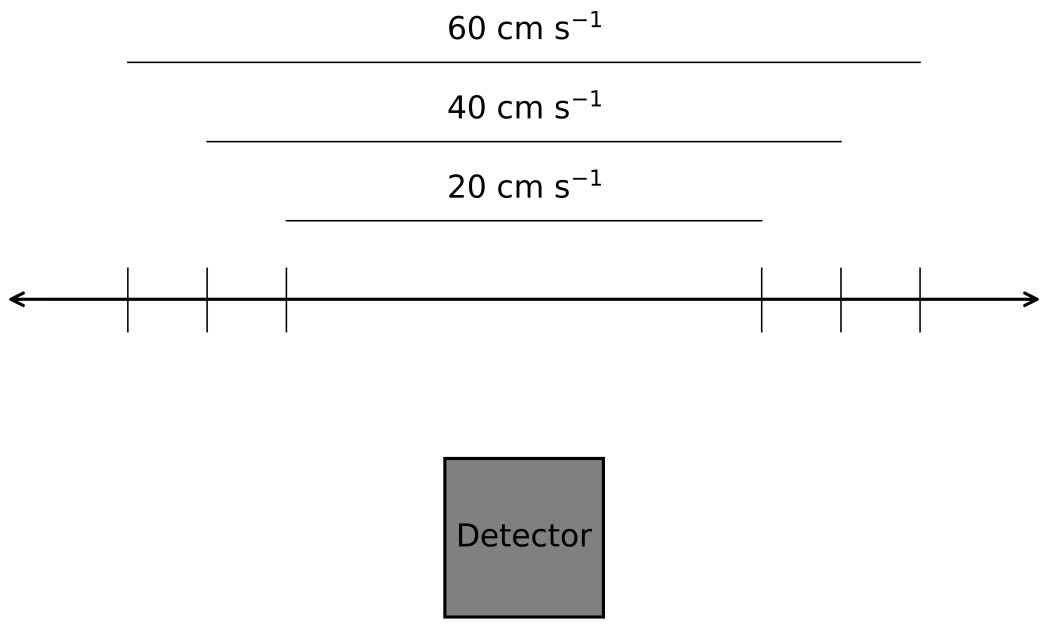

Figure 2.5: Schematic showing the different solid angles an object presents as it moves past an observer.

Masket's values were originally calculated using the ORACLE programming language. This research was conducted using the Python programming language because it could produce acceptable results in a reasonable computational time and because the results could be analyzed in the same language. The Python script used to calculate the solid angle based on Masket's formulas was divided into three parts: 1) a sorter function which determined which region to use in calculating the solid angle, 2) the calculation portion which applied the selected Masket formula to each case, and 3) a function to calculate the integrals in Masket's formulas. The solid

angles for the individual point sources were calculated individually. The line sources were each divided into ten equally spaced sections and the solid angle calculated at each division point. The integral of the ten solid angles was then calculated, normalized to one integration time interval (1 s). This became the composite solid angle for that line source.

The sorter function works to determine which region around the detector the source is located. If z is above the reference plane and ρ is less than or equal to the detector radius the source is in region I. If z is above the reference plane and ρ is greater than the detector radius the source is in region II. If z is between the reference plane and the length of the detector and ρ is greater than the detector radius the source is in region III. The regions around the detector are shown in Fig. 2.3.

In region I, only the top of the cylinder contributes to the solid angle because the source is directly above the detector. Therefore, only Ω_{I} is calculated in Eq. 2.3. In region II, both the top and side of the detector contributes to the solid angle. Here, Ω_{II} is calculated to account for the top of the detector. To account for the side contribution, the Ω_{III} for the imaginary cylinder from the top of the detector to the height of the source is subtracted from the Ω_{III} for the imaginary cylinder and the detector combined, Fig. 2.6. In region III, only the side of the detector contributes to the solid angle because the source is located between the top and bottom planes of the detector. Ω_{III} is calculated twice and summed, Fig. 2.7. The first calculation is the Ω_{III} for the cylinder between the top of the detector and the plane of the observer point. The second calculation is the Ω_{III} for the cylinder between the plane of the observer point and the bottom of the detector.

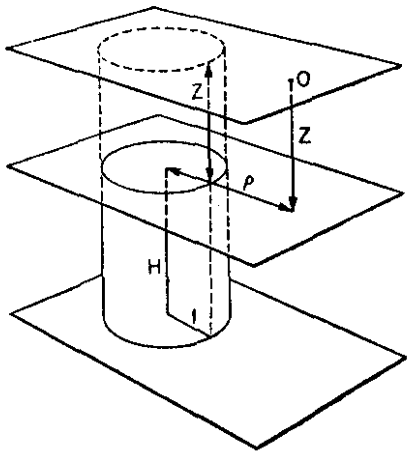

Figure 2.6: Figure showing the imaginary cylinder and solid cylinder used to calculate the side solid angle in region II. Reprinted from Masket et al., 1956.

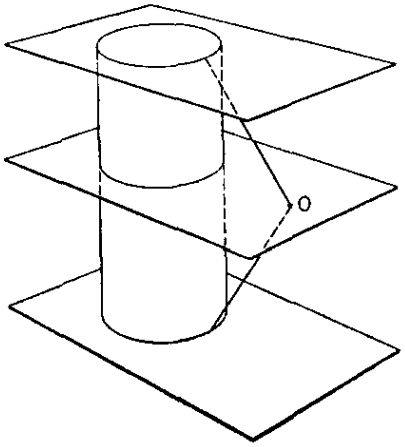

Figure 2.7: Figure showing both portions of the solid cylinder used to calculate the side solid angle in region III. Reprinted from Masket et al., 1956.

The integrals in Masket's formulas for Ω_{II} and Ω_{III} are discontinuous over the ϕ domain. This is because the $S_{1,2}$ rays incorporate the square root of a term that can become negative if

ρ is large enough and are thus impossible for Python to calculate. To accommodate this in the Python script, a 16th order Taylor series approximation of the rays was used to estimate the integrand value at each ϕ. The Riemann Sum integration method was used to further simplify the calculation. The number of intervals in the Riemann Sum was chosen to give the most precise estimate within the computing power available. The integrand was evaluated at each of ten million points between the ϕ limits of integration and summed. This result was then fed back to the Masket formula to calculate the solid angle at that specific source location.

The solid angles for the point source configurations were calculated individually. Moving sources were modeled using line sources. To calculate the solid angle for the line source a solid angle profile was first calculated. This profile is the solid angle at discrete locations in the x-direction of travel at a constant z height above the detector. This profile was then sampled in the interval of each line and normalized to one integration time unit, Fig. 2.5.

The Masket table values and Python results for the point sources were compared to establish the Python calculations are accurate. The Masket values were plotted along the x-axis and the Python results along the y-axis. A linear regression was then fit to this plot. A slope of 1 for this regression fit represents perfect agreement between the Masket table values and the Python script.

The MCNP simulation modeled the source configurations as described above. The modeled cylinder was 2 in x 2 in (5.08 cm x 5.08 cm), made out of sodium iodide (NaI), wrapped in aluminum and aluminum oxide, and oriented vertically with the top face located at the x=0 plane. The wrapping was to approximate a real world detector, simulating the attenuation of low energy photons through a detector's casing. The entire arrangement was placed in a vacuum universe 10 cm above a brick floor. The mean free path of photons in air at the energy modeled is orders of magnitude larger than the modeled distances between source and detector.

The photon energy for all MCNP simulations was 662 keV, the energy of ^{137}Cs which is a standard radionuclide used for detector calibration. An F8 tally over the cylinder was used

to approximate detector efficiency. The energy range of the F8 tally was 0-2 MeV to simulate a multichannel scalar signal. The F8 tally measures the energy deposited in the the detector volume and reports the value as efficiency. Each simulation modeled $1x10^7$ particles. A direction bias was applied to the source definition card. The number of particles modeled and the direction biasing was necessary to produce results with relative errors less than 10%.

The Python results and MCNP results for the point sources and line sources were then compared to establish that solid angle does explain the change in efficiency. The Python results were plotted along the x-axis and the MCNP results along the y-axis. A linear regression was then fit to this plot. The slope of this fit represents the intrinsic efficiency of the modeled detector. This is because the Python results are the geometric efficiencies and the MCNP results are the total efficiencies for each trial.

The MCNP efficiencies were then plotted as a function of the speed simulated. A fit of this plot was made to establish the relationship between efficiency and speed. The desired shape of this curve is the previously observed efficiency phenomenon. The fit of this plot will then explain how efficiency is dependent on speed and is the tool that can be used by the surveyor to tailor their survey plan.

Finally, a generic MDA for the modeled system was then calculated by inserting the efficiencies calculated above into Eq. 2.1. The other variables are normalized so that the effect of efficiency on MDA can be extracted and highlighted. Because the other variables are assumed to be static during counts the shape of the MDA curve will remain the same and only the values will shift based on count setup.

2.3 Results and Discussion

If the integration time is kept constant and detector speed is changed, the amount of the solid angle profile that is swept over during a count is different. When normalized for integration time the composite solid angle of the count decreases as speed increases. This is what causes the

change in efficiency of a detector relative to detector speed.

A plot of Masket table values versus Python results is shown in Fig. 2.8. They were fit to a linear regression where a slope of 1 represents perfect equivalence between the two datasets. The slope of Fig. 2.8 is 1.000422 $\pm$ 0.000222 with an r-squared value of 0.999999 meaning that the Python script calculated the same values in Masket's table. These results affirm that Masket's equations were properly coded in Python and can be relied upon to give accurate results for source locations not listed in Masket's table.

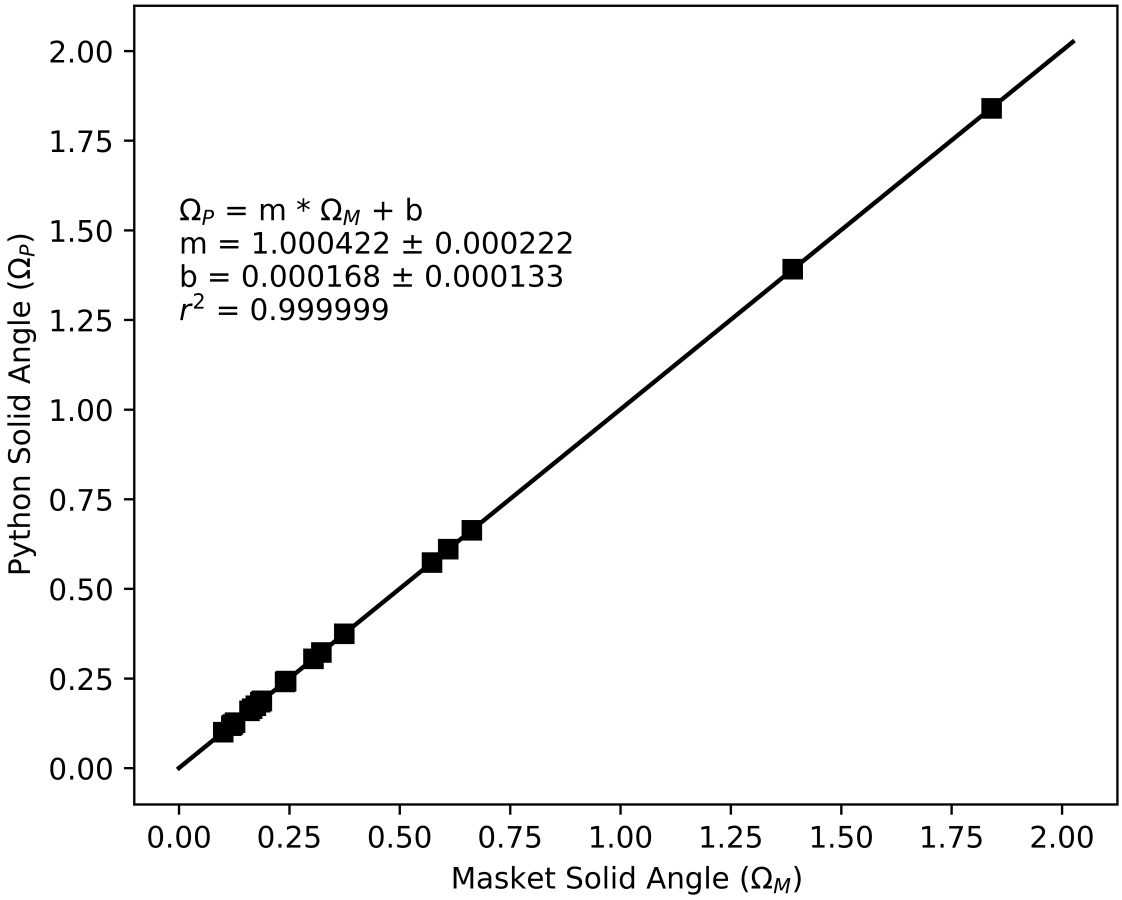

Figure 2.8: Plot and fit of Masket solid angle values versus Python solid angle results for the point source locations.

A plot of Python, Ω, results versus MCNP, ϵ, results for the modeled point sources is shown in Fig. 2.9. The MCNP tally was used as a proxy for the total efficiency while the Python solid angle calculation was used as a proxy for geometric efficiency. Therefore, the ratio of MCNP values to Python values is a proxy for the intrinsic efficiency of the material. The plot is linear with a slope of 0.079491 ± 0.000041 and an r-squared of 0.999995. Analysis of these modeling results suggests that the 2x2 NaI has an intrinsic efficiency of approximately eight percent, which compares favorably to experimentally determined values of actual detectors, (Sakai, 1987; Holl, Lorenz, & Mageras, 1988). This result validates that these simplified MCNP simulations were an accurate representation of the more complex scenario in the real-world. Additionally, it strengthens the argument that a change in solid angle is the driving force behind a change in detector efficiency. If the ratio between Python and MCNP values was not linear then it would mean that the intrinsic efficiency was not constant and that some other physical process was taking place.

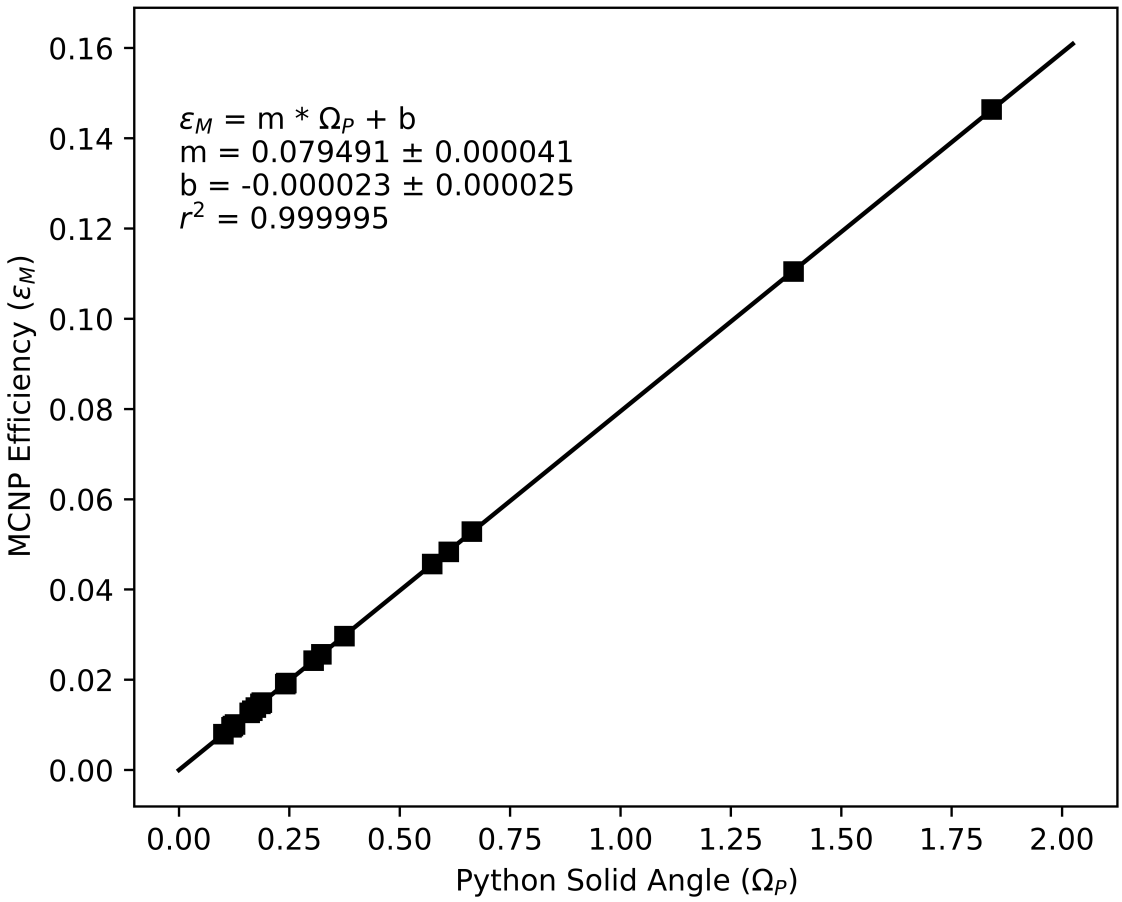

Figure 2.9: Plot and fit of Python solid angle results versus MCNP efficiency results for the point source locations and line source trials.

The above plot shows that the total efficiency of a detector is dependent on its solid angle to a source, not only for static point sources but also line sources approximating a moving detector. Therefore, the MCNP efficiencies can be plotted as a function of speed, Fig. 2.10. The shape of the plot is the characteristic decrease exhibited in previous research, (Marianno et al., 2000). This plot was fit with a modified four parameter logistic function (M4PL), Eq. 3.1, (Sittampalam et al., 2004). The maximum efficiency of the curve, A, is 0.018961 $\pm$ 0.000058. The minimum efficiency of the curve, D, is 0.000936 $\pm$ 0.000492. The slope of the curve,

B, is 1.468228 $\pm$ 0.038920. The speed which results in 50% of the maximum efficiency, C, is 60.487853 $\pm$ 2.344416 cm s^{-1}. This speed is similar to the MARSSIM target scan rate of 50 cm s^{-1} indicating that this simplified detector system would be a good candidate for performing surveys according to that standard, (U.S. NRC, 2000). This fit of efficiency data has never been identified before.

$$\epsilon = D + \frac{A - D}{1 + \left(\frac{x}{C}\right)^B} \tag{2.4}$$

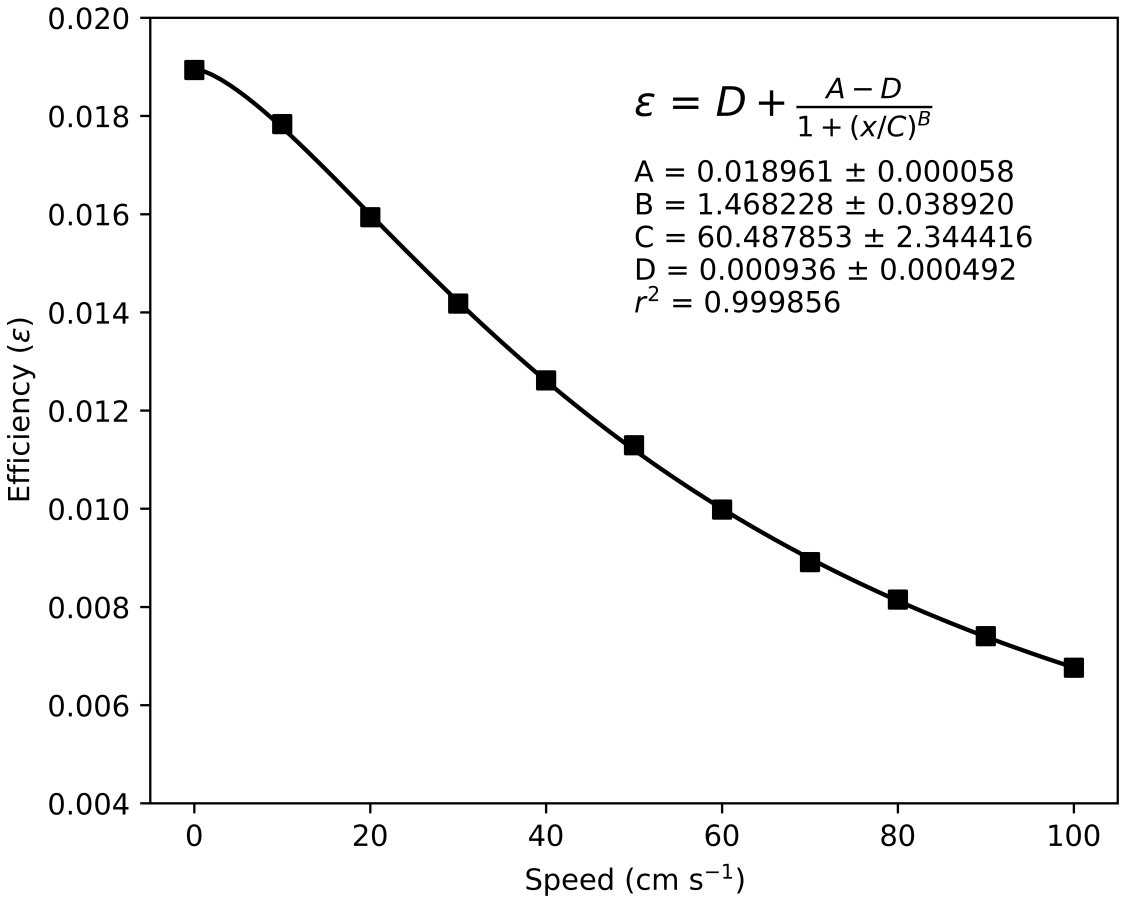

Figure 2.10: Plot and fit of MCNP efficiency versus speed.

The MDA can now be assessed by inserting Eq. 2.4 into Eq. 2.1 to yield Eq. 2.5. The detection limit and yield were normalized to 1 to show the full effect of efficiency on the MDA as a function of detector speed, Fig. 2.11. The composite MDA model starts at 0 cm s^{-1} with a minimum MDA of 52.77 normalized units. It slowly rises until approximately 40 cm s^{-1} with an MDA of 79.33 general units. From there it appears to rise with a linear slope until the end of the plot at 100 cm s^{-1} with an MDA of 147.77 general units. This figure can be referenced when seeking to find the maximum speed possible while remaining below a required MDA. Conversely, the lowest MDA achievable can be determined if speed is the dependent variable. For example, if regulations require that the MDA be 105 in normalized units the fastest speed the detector would move is approximately 64 cm s^{-1}. If the operational constraints require the speed to be 75 cm s^{-1} then the MDA would be 117.16 in normalized units.

$$MDA = \frac{L_D}{Y\left(D + \frac{A-D}{1+\left(\frac{x}{C}\right)^B}\right)T} \tag{2.5}$$

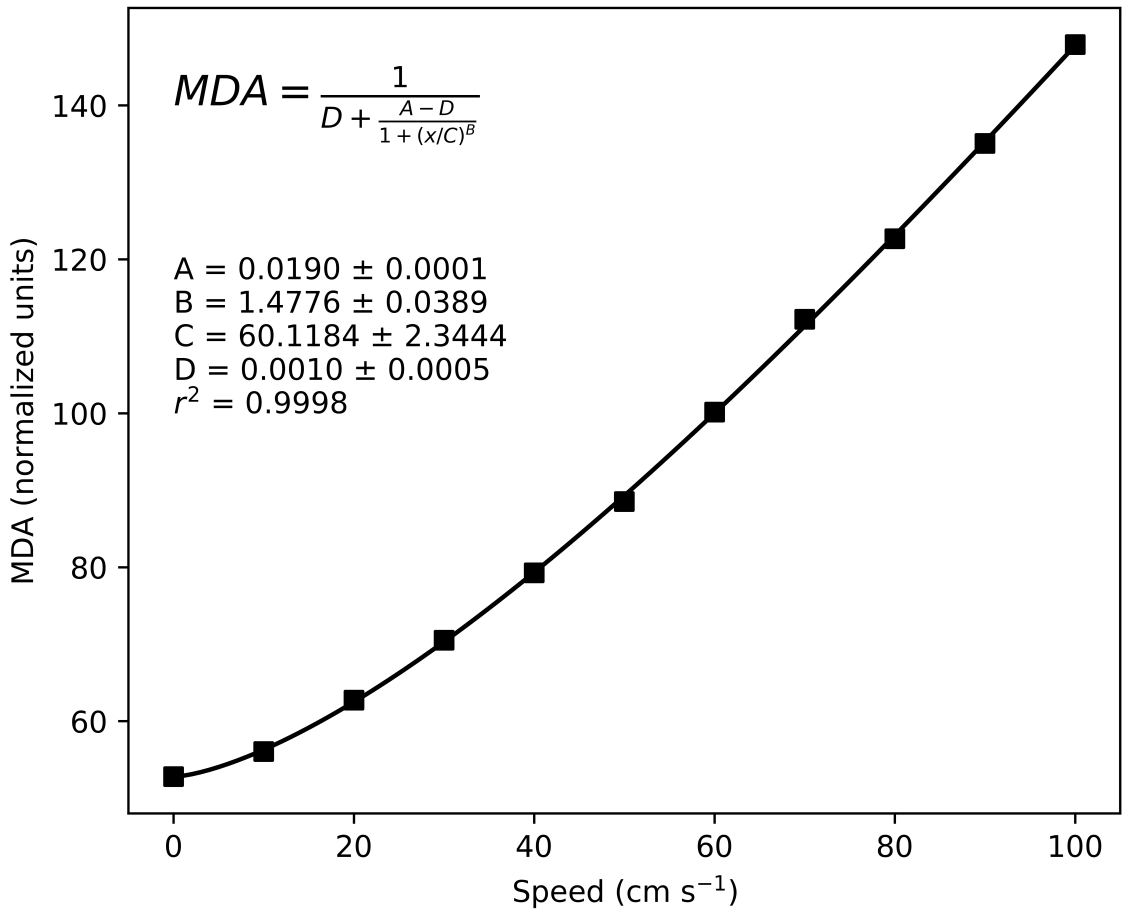

Figure 2.11: Plot of MDA model using a generic detection limit and yield.

2.4 Summary

MDA is a function of background, yield, efficiency, and time of count. Efficiency is the quantity the surveyor has most control over. Efficiency is the combination of how many photons impact the detector (geometric efficiency) and how many of these photons interact and produce a signal inside the detector (intrinsic efficiency). Under typical survey conditions intrinsic efficiency is unchanging. This research showed how geometric efficiency quantifies MDA as a function of speed. Geometric efficiency can be calculated by considering the solid angle of the detector. Solid angle is the angle subtended by an object from a point. In this research the source

is the point and the detector is the object. MCNP results were correlated to solid angle calculations using point and line sources. The solid angle results were then fit with the M4PL model to calculate efficiencies.

The M4PL model was used to develop a relationship between speed and MDA. This relationship is a first of its kind. There are three uses of this relationship 1) verify the accuracy of your current survey plans, 2) optimize survey plans for speed and accuracy, 3) identify limits of detection accuracy based on operational speed. It will be useful in allowing surveyors to design site surveys to be conducted as quickly and cost effectively as possible while still meeting regulatory requirements. This relationship is also invertible which will allow surveyors to derive MDAs their detection systems can achieve given operational constraints.

This is the desired relationship between speed and efficiency which can now be used to tailor survey plans to fit operational, logistical, regulatory and fiscal needs. This foundational relationship has the potential for many large and small applications in both the academic and operational fields. It can be used to improve survey accuracy when used in a way to identify a single source with an unknown location. Slower speeds within a given survey field will produce a more accurate pinpoint of source location at lower activities. The speed which results in 50% of the maximum efficiency, 60.12 ± 2.34 cm s^{-1} is similar to the MARSSIM target scan rate of 50 cm s^{-1}. This means that variations in speed will have immediate effects on detector efficiency. Depending on the size of the survey field, robotic systems or other means of transporting the detector that can travel at consistent speeds might be necessary to achieve desired results.

3. EXPERIMENTALLY VERIFYING MINIMUM DETECTABLE ACTIVITY TO DETECTOR VELOCITY RELATIONSHIP

3.1 Introduction

In the last few decades mobile detection systems have expanded in prevalence in the field of radiation detection. This change in paradigm has brought new challenges to the survey world. Determining appropriate survey patterns, variable background fields, operational constraints, and accounting for any impact speed may have upon detector performance form the bulk of these challenges, (U.S. NRC, 2000).

This last challenge, the effect of speed on detector performance, was noted in the 1997 Multi-Agency Radiation Survey and Site Investigation (MARSSIM) manual, (U.S. NRC, 2000). Marianno identified the phenomenon in his data when evaluating the performance of a Field Instrument for the Detection of Low-Energy Radiation, (Marianno et al., 2000; Marianno, 2015). Schroettner, et. al., sought to address this problem through varying the integration speed, (Schroettner et al., 2009). However, the relationship between speed and efficiency has not been quantified until recently, (Falkner & Marianno, in prep 2018a). The relationship was identified by fitting MCNP results to a modified four parameter logistic (M4PL) equation, (Sittampalam et al., 2004). The original logistic function starts at a minimum and rises to a maximum. The rise is gradual at first, quickly steepens to a maximum slope, and then tapers off. The modifications made to the logistic function were to mirror the shape but start at a maximum and progress to a minimum. In this equation the speed of the detector is x, the maximum efficiency is A, the minimum efficiency is D, the slope of the equation is B, and the speed at which the efficiency is half that of the maximum is C.

$$\epsilon = D + \frac{A - D}{1 + \left(\frac{x}{C}\right)^B} \tag{3.1}$$

This current research sought to reproduce in a laboratory setting the modeled relationship with as few outside confounders as possible. A robotic system was used to carry a detection system at various speeds. This allowed for reproducing consistent trial conditions for the duration of this study. The parameters held constant from trial to trial included track length, radionuclide, source location, background, detector height, and integration time. The parameters that varied from trial to trial included speed and source strength.

One method of assessing a detector's performance is to calculate its reportable minimum detectable activity (MDA), Eq. 3.2. MDA is the lowest level of activity present which can be detected with statistical confidence. The components of Eq. 3.2 are yield (Y), integration time (T), limit of detection (L_D), and efficiency (ϵ). Solving Eq. 3.2 for efficiency while fixing the limit of detection, integration time, and yield enabled the derivation of a relationship that can be used by field surveyors to quickly tailor their survey plans to be as accurate as needed while remaining cost effective.

$$MDA = \frac{L_D}{Y\epsilon T}, \tag{3.2}$$

3.2 Methods and Materials

The robot used in this experiment was an LT2 Tracked ATR Robot Platform purchased from SuperDroidRobots (Super Droid Robots, 2017). It consisted of an aluminum body frame, two motors, a battery to power each motor, a wireless receiver to connect the robot to the remote control, and a controller module that received input from the handler, Fig. 3.1. The robot measured 67.31 cm long by 17.78 cm tall by 41.91 cm wide and with a shipping weight of 19.1 kg. The remote control used for this experiment was a Spektrum Dx6E hobby airplane remote control that had already been programmed and paired with the robot by SuperDroidRobots prior to delivery. The remote control was programmed to set the robot throttle at a preset fraction of maximum motor power for the duration of each trial.

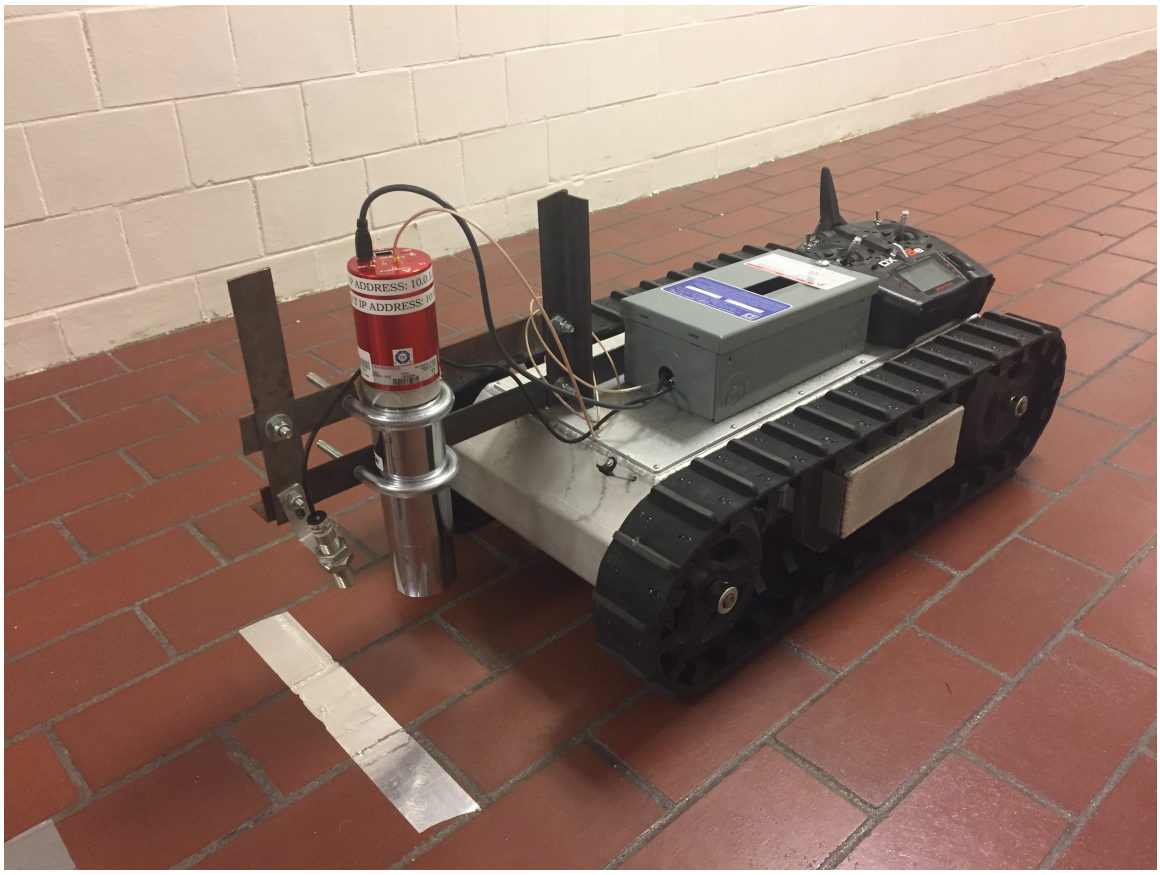

Figure 3.1: Photo of robot used during experiment. Shown are the detector, mca, optical sensor, and remote control.

The detection system consisted of a 2 in x 2 in (5.08 cm X 5.08 cm) sodium iodide detector, model 802 from Canberra, connected to a Canberra Osprey. The unit was U-bolted in a downward orientation to a steel frame extending from the robot with the face of the detector 10 cm from the floor. There was noticeable vibration in the detector/MCA assembly at the higher trial speeds. The amplitude of the vibration was significantly less than the diameter of the detector and thus did not have an effect on the experimental result. The vibration did cause the MCA to work itself loose from the detector. The MCA was taped to the detector to prevent it from disconnecting during trials.

The detector was operated through scripts written in Python 2.7, (Rossum, 2015) using the Canberra Software Development Kit, (Canberra Industries Inc., 2011). The Python script controlled when the count started, how the count was conducted, when the count ended, and how the resulting data was collected and stored. The multichannel scaler (MCS) function on the MCA was used to gather count information for the entire energy range of the detector. The MCS function is the "acquisition of time-correlated data in an MCA. Each channel is defined as a time window; all pulses are stored in one channel, then stepped sequentially to the next", (Gilmore, 2011). This means the count information is binned by time in the available channels instead of by energy as in a typical count spectrum. The integration time used was 0.02 s. This resulted in collecting enough data points per trial to sufficiently capture the source peak. The timing resolution of the Python script was determined to be $4.1026\text{x}10^{-7}$ seconds. Timing resolution impacts the precision of any timestamps used in calculations. This value is several orders of magnitude below the integration time and thus has no impact on the timing used.

Prior to conducting trials the detector was calibrated and settings input. Energy calibration was conducted using ^{241}Am, ^{137}Cs, and ^{60}Co on a 2 MeV scale because they represent the low, middle, and high end of the energy spectrum of interest in this research. The course gain and fine gain were set to 2 and 3.38, respectively, in the Python script. The operating voltage for the photomultiplier tube (PMT) was set to 750 V as suggested in the Python script example for an MCS count provided in the SDK. However, the Canberra manual for the detector sets the operating voltage to 800-1100 V. The operating voltage determines the potential difference across the dynodes in the PMT which determines the final size of the PMT output pulse. Increasing voltage across the detector will increase the count recorded by the MCA. Although the SDK recommended value of 750 V was used in the trials, the higher voltage recommended would have been more appropriate to use. The integration time was set to 0.02 s in the Python script using the SDK. The full energy range was counted to simplify analysis and to mimic less sophisticated detectors to broaden the applicability of this research.

An ROS-P remote optical sensor coupled with a SPSR-IM interface module, both from Monarch Instruments, was used to trigger the detector to start and stop counting during each trial. The optical sensor would trigger when it crossed a strip of reflective tape at the start of the track and again at the end of the track. After each trigger the interface module would send a 5 V time-to-live pulse via a BNC connection to a General Purpose Input/Output (GPIO) connection on the MCA. The MCA then used the GPIO signal to start and stop the count acquisition. Due to limitations in signal transmission between the various components, there would be a minimal delay on the order of 0.5 s between crossing the tape and the count beginning.

The optical sensor was mounted on the steel frame preceding the detector and angled backwards to approximately 15 degrees, as specified in the unit's manual, (Monarch Instruments, 1995). The angle served to trigger the detector as accurately as possibly as it crossed the reflective tape. The laser was aimed such that it impacted the ground directly underneath the leading edge of the detector. The angle also minimized scattering of the optical signal while the robot was traveling down the track.

The track was re-purposed from a previous experiment with already established distance markings. The track measured approximately 600 cm in length. It was situated in a basement hallway approximately 180 cm wide. The floor of the track was brick and the walls of the hallway were concrete. Reflective tape was placed at the start and end of the track. The time of each trial and the length of the track was then used to calculate the average speed the robot traveled in each trial. The robot was started a short distance before the beginning of the track so as to gain its target trial speed and to settle out any vibration in the detection system due to the sudden acceleration of the robot. This length needed to be extended further as the target trial speed increased but never exceeded 0.5 m. No counts were recorded during this pre-track length and this distance was not included in the speed calculation. All distance measurements were made from the leading edge of the reflective tape strips.

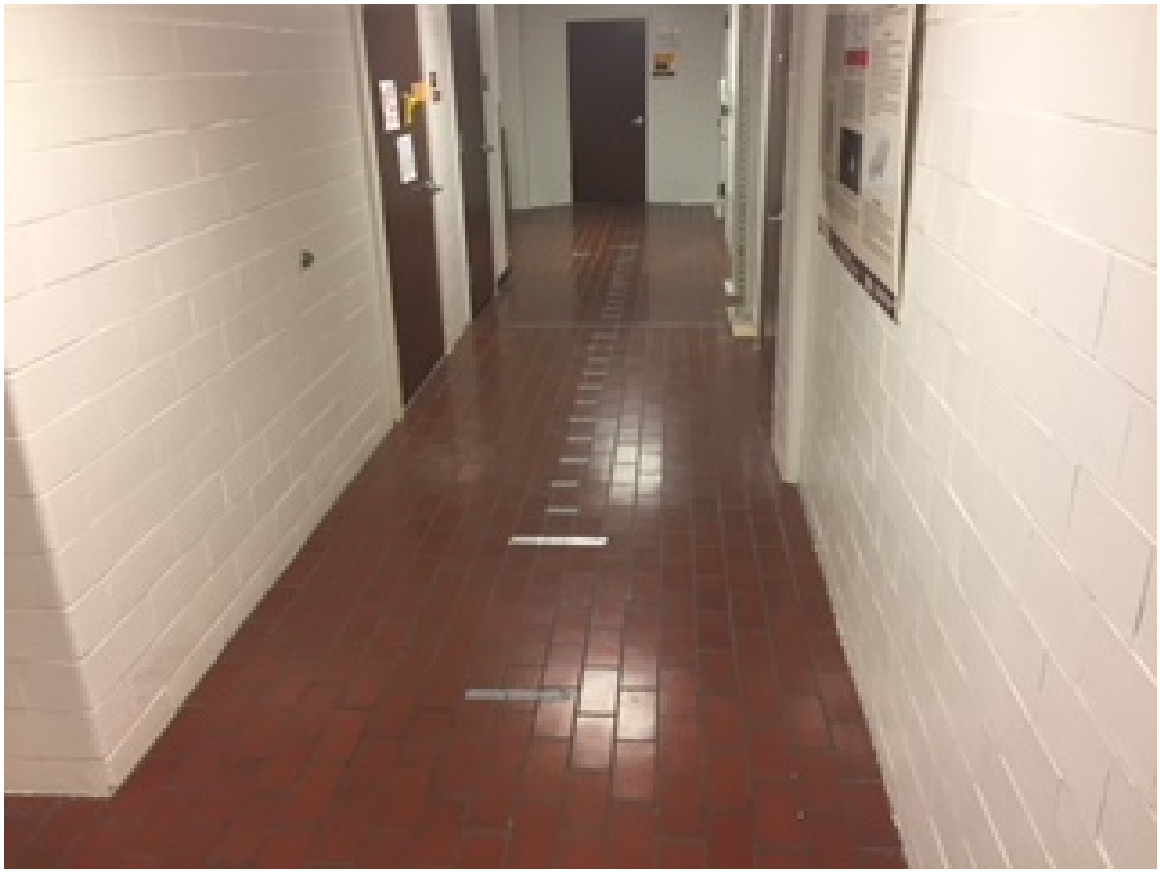

Figure 3.2: The hallway were the robot experiments were conducted. Visible are the starting position and distance markings.

The sources used for this experiment were ^{137}Cs buttons. In total, five button sources were used in increments of one. The activity of each button source was 1 ± 0.1 μCi. The sources were all assayed in Jan 2013 and decay corrected to the dates of the experiment. The sources were placed at approximately 250 cm from the start of the track. This source location was used to ensure that the entire radiation field was captured; it was feared that the radiation field after the source would be cut off if placed too close to the end. The first two sources were placed next to each other perpendicular to the track and then subsequent sources were stacked on this pair so as to minimize the height above the track the sources ended up being.

The velocity of the robot was an important parameter of this research. Throttle settings used in the experiment were 50%, 75%, 100%, 125%, and 150% of a preset power level determined by SuperDroidRobots. The maximum throttle setting was a limitation imposed by the remote control. The minimum throttle setting was the lowest setting that still produced smooth and consistent forward motion. Below this throttle setting, at around 40%, the robot would jerk forward slowly. The rest of the throttle settings were chosen to produce trial results in distinct clusters of speeds since the actual speeds achieved in the trials depended on battery level. A total of ten trials were conduced at each throttle setting. The average speed of the robot for all trials at each throttle level is shown in Table 3.1. The relationship between throttle and speed is linear between settings 50 to 150. The intercept of this relationship is at a throttle setting of 34%, consistent with the observed behavior in the lab. The throttle setting with the highest variation, as indicated by the standard deviation in Table 3.1 is 100%. This is likely because trials were conducted in increasing or decreasing throttle cohorts each day. The battery was charged during changes between cohorts and the trials immediately after would have more power than the trials prior to the break. This break sometimes occurred before the 100% trials and sometimes after the 100% trials leading to a larger variance in power levels.

Table 3.1: Throttle settings and the corresponding average robot speeds.

Throttle Setting	Robot Speed (cm s^{-1})
50	19.08 ± 0.68
75	39.90 ± 1.04
100	63.58 ± 3.50
125	86.28 ± 0.08
150	120.67 ± 0.14

To produce robust statistics, ten trials were conducted at each throttle setting for each source strength. In each trial the robot always traveled in the same direction. Throttle setting would progress from low to high or vice versa and then the number of sources was increased from 0 to 5 incrementally by 1. In addition to trials being conducted at various throttle settings, data was collected for a static detector directly over the source location for approximately 30 seconds per count for all source strengths. Static counts had to be triggered manually by passing a strip of reflective tape under the optical sensor to start and stop each count. The 0 source strength trials were conducted to test whether or not background is affected by speed. This is important because if it is, there are two terms dependent on speed in Eq. 3.2, the L_D and the ϵ.

A typical background count is shown in Fig. 3.3. The portion of the count in the gray box was used to calculate the average background count per integration time. The first and last ten counts were disregarded to further ensure only data gathered at desired settings was used. This average count per integration time was used to calculate a background count rate in units of count per second (cps). This was done for all trials, static and dynamic, with zero sources present. The average and standard deviation for the remaining data was calculated. These values were for 0.02 s integration periods and needed to be multiplied by 50 to calculate an average 1 s background count rate for each trial. The average background count rate and standard deviation was then calculated for each throttle setting. For the rest of the experiment, the background count rate for the static trial was used when calculating net values because it was viewed as equivalent to current standard practice when conducting radiation surveys. The detection limit, L_D, for each throttle cohort was calculated using Currie's Equation, Eq. 3.3. The σ_B is the standard deviation of the background.

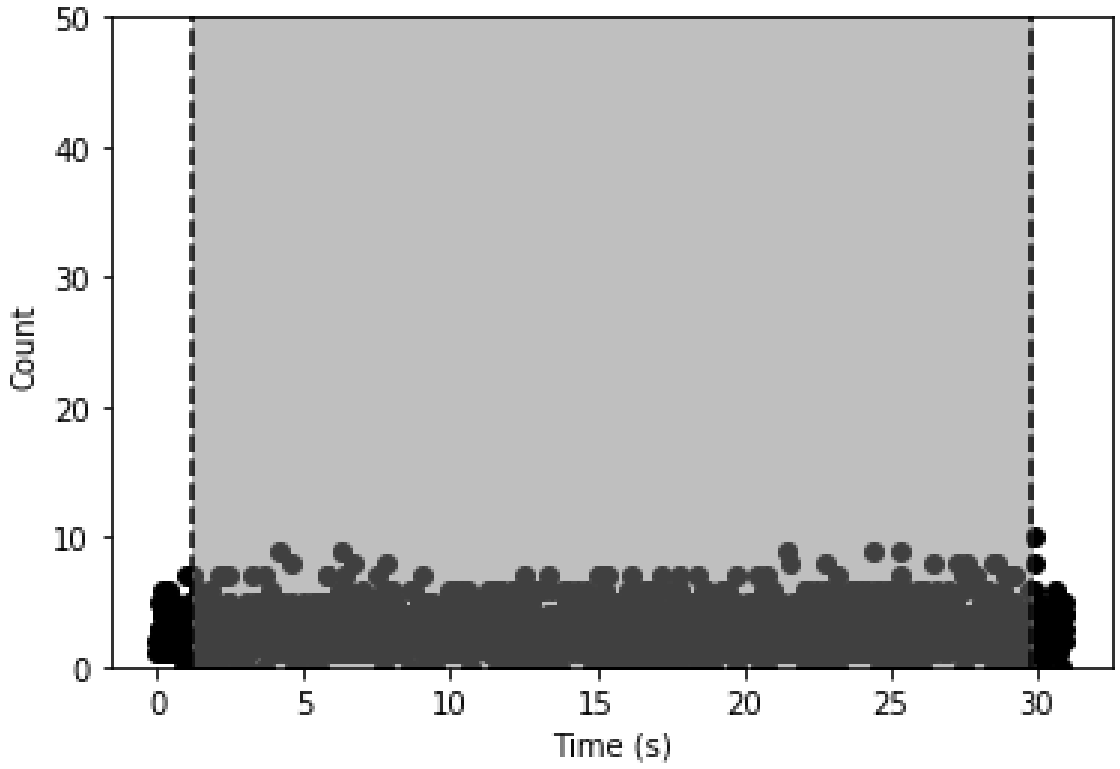

Figure 3.3: Plot of typical static background count profile shown for illustration purposes. Counts in gray region were used to calculate the background count rate.

$$L_D = 4.65 * \sigma_B + 2.71 \tag{3.3}$$

For trials where sources were present, the maximum count recorded was assumed to be the peak signal indicating the location of the source. A typical source count is shown in Fig. 3.4. The portion of the count in the gray box illustrates what was used to calculate the peak count per integration time. Each count in the experimental trial was conducted over 0.02 seconds and consisted of a total count at all energies. Therefore, in order to compare the experimental results to modeling results, all peaks were normalized to one second by summing fifty counts centered on the maximum. A net peak count was then calculated by subtracting the background

count value. The peak counts were then averaged within each throttle setting and source strength cohort. The efficiencies for each throttle and source strength cohort were calculated using the decay corrected activity of the sources used and then plotted against the model fit from previous work, (Falkner & Marianno, in prep 2018a). The static trials for each of the source strengths directly over the source were gathered to show the static detector's efficiency as a baseline for a comparison to the speed trials. Errors were propagated throughout the calculations.

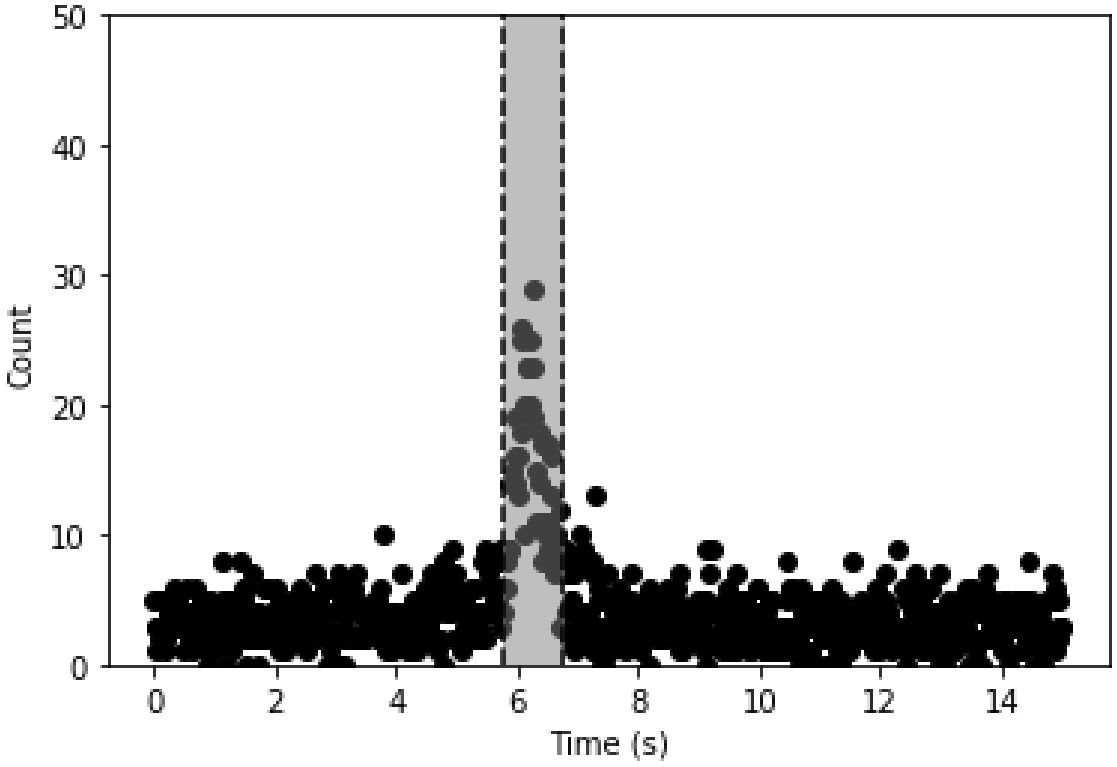

Figure 3.4: Plot of typical source count profile shown for illustration purposes. Counts in gray region were used to calculate the peak count.

The experimental data were compared to Eq. 3.1 using parameters derived in previous research, (Falkner & Marianno, in prep 2018a). The parameters of the M4PL used are listed in

Table 3.2. The model was plotted and the experimental data superimposed to show how well the two data sets compare. The model and experimental data were then input into Eq. 3.2, with an integration time of 1 s, a yield of 0.85, and the limit of detection determined above, and the MDAs plotted.

To validate whether the model applies to this experimental setup, the MDA for each throttle cohort was independently calculated. First the count totals for each speed cohort were plotted as a function of source strength. Each speed cohort was then fit to a linear regression of counts as a function of source strength. The linear regression was rearranged to be source strength as a function of counts. The regression parameters and the detection limit determined above were then used to calculate the MDA for each speed cohort. These calculated MDAs were then plotted as a function of speed along with the model MDAs.

Table 3.2: Parameters of the M4PL model used to compare simulation and experimental results, (Falkner & Marianno, in prep 2018a).

Parameter	Value
A	0.0149 ± 0.0000
B	1.5475 ± 0.0257
C	52.2784 ± 0.8991
D	0.0014 ± 0.0002

3.3 Results and Discussion

Representative samples of trials at different speeds and different source strengths are shown in Fig. 3.5. Since all data points were taken in 0.02 s intervals and the track distance is the same length for all trials, the number of data points collected decreased as robot speed increased. The increased data density on the left is due to slower robot speed acquiring more counts over the

course of the track. The difference in peak count is due to different source strengths being used for each trial. The count times were converted to track distance to compare different throttle cohorts. The peak of each trial is at approximately at 250 cm, as expected. The max count value of each peak increases with source strength but is constant with throttle setting, Table 3.3.

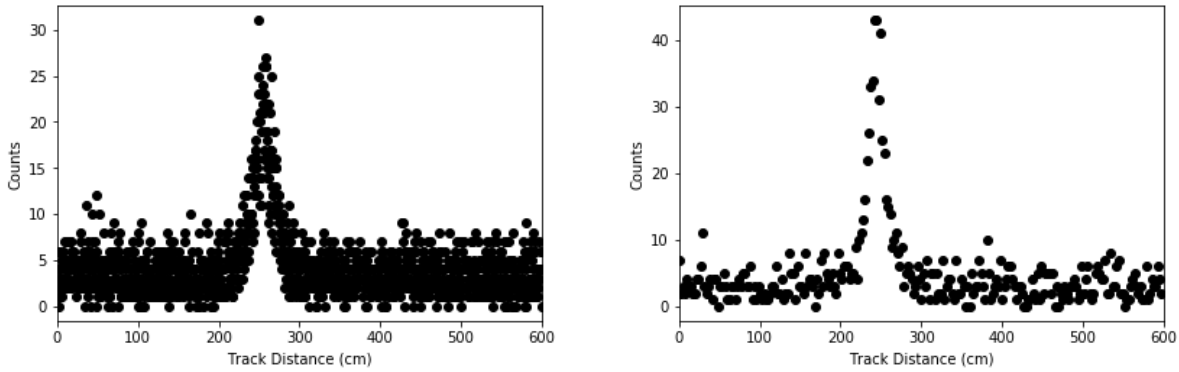

Figure 3.5: Results for two example trials are shown for illustration purposes.

Table 3.3: Average peak integration count for each throttle/source cohort are shown.

Throttle \ Sources	1	2	3	4	5
0	28 $\pm$ 5.3	38 $\pm$ 6.2	52 $\pm$ 7.2	63 $\pm$ 7.9	75 $\pm$ 8.7
50	18.4 $\pm$ 1.7	30.3 $\pm$ 3.1	41.2 $\pm$ 3.3	48.9 $\pm$ 2.9	59.9 $\pm$ 4.5
75	16.9 $\pm$ 1.7	27.7 $\pm$ 2.4	38.3 $\pm$ 3.9	49.5 $\pm$ 3.9	59.1 $\pm$ 5.0
100	16.6 $\pm$ 1.8	27.6 $\pm$ 1.8	36.2 $\pm$ 2.9	46.6 $\pm$ 3.1	57.9 $\pm$ 6.5
125	15.0 $\pm$ 1.5	26.1 $\pm$ 3.6	34.9 $\pm$ 4.9	46.4 $\pm$ 3.9	55.6 $\pm$ 4.4
150	14.0 $\pm$ 1.8	23.2 $\pm$ 2.3	32.6 $\pm$ 4.1	43.0 $\pm$ 5.5	52.8 $\pm$ 4.2

Characterizing the background environment is important because it defines what the limit of detection is for your count. The average backgrounds and standard deviations for each throttle setting are listed in Table 3.4. The backgrounds are all within two standard deviations of each other. This shows that the velocity of the detector does not have an affect on background count rate.

This is important because it means that the detection limit in the MDA calculation is a function of the environment, and thus static, rather than a function of the detector. This can be seen in Eq. 3.2. Here the limit of detection (effect of background) and the efficiency of the detector (effect of speed) are two separate components. Using Eq. 3.3 and the static background count rate standard deviation the detection limit for the laboratory environment can be calculated as 59.44 cps.

Table 3.4: Throttle settings and the corresponding average background count rate.

Throttle Setting	Background Count Rate (cps)
0	148.0 ± 12.2
50	153.0 ± 12.3
75	164.7 ± 12.8
100	155.2 ± 12.4
125	161.1 ± 12.7
150	155.9 ± 12.4

The source trial efficiencies are shown in Fig. 3.6. The experimental data demonstrate a general decreasing trend as speed increases similar to the modified 4-parameter logistic function relationship (M4PL) derived in (Falkner & Marianno, in prep 2018a). There appears to be two

trend lines in the experimental data. The data begins at 0 cm s^{-1} with calculated efficiencies of approximately 0.016 and decrease sharply until approximately 60 cm s^{-1} with efficiencies of approximately 0.007. From there the trend trend line continues to decrease with a shallower slope until 120 cm s $^{-1}$ with efficiencies of approximately 0.004. Plotted with the experimental data is the model derived by Falkner et al. Error bars on the experimental data extend two standard deviations. Thus there is significant agreement between the shape of the M4PL and the experimental data. However, the experimental values are greater than two standard deviations below the M4PL owing to the lower high voltage used during the trials. This confirms that the M4PL relationship is an accurate model for the influence of speed upon efficiency.

Features in the M4PL, such as the increasing slope change at approximately 15 cm s^{-1} and the decreasing slope change at approximately 70 cm s^{-1}, are not captured in the experimental data because the robot used for this experiment could not differentiate speeds any finer. Even so, the relationship between detector speed and detector efficiency is validated.

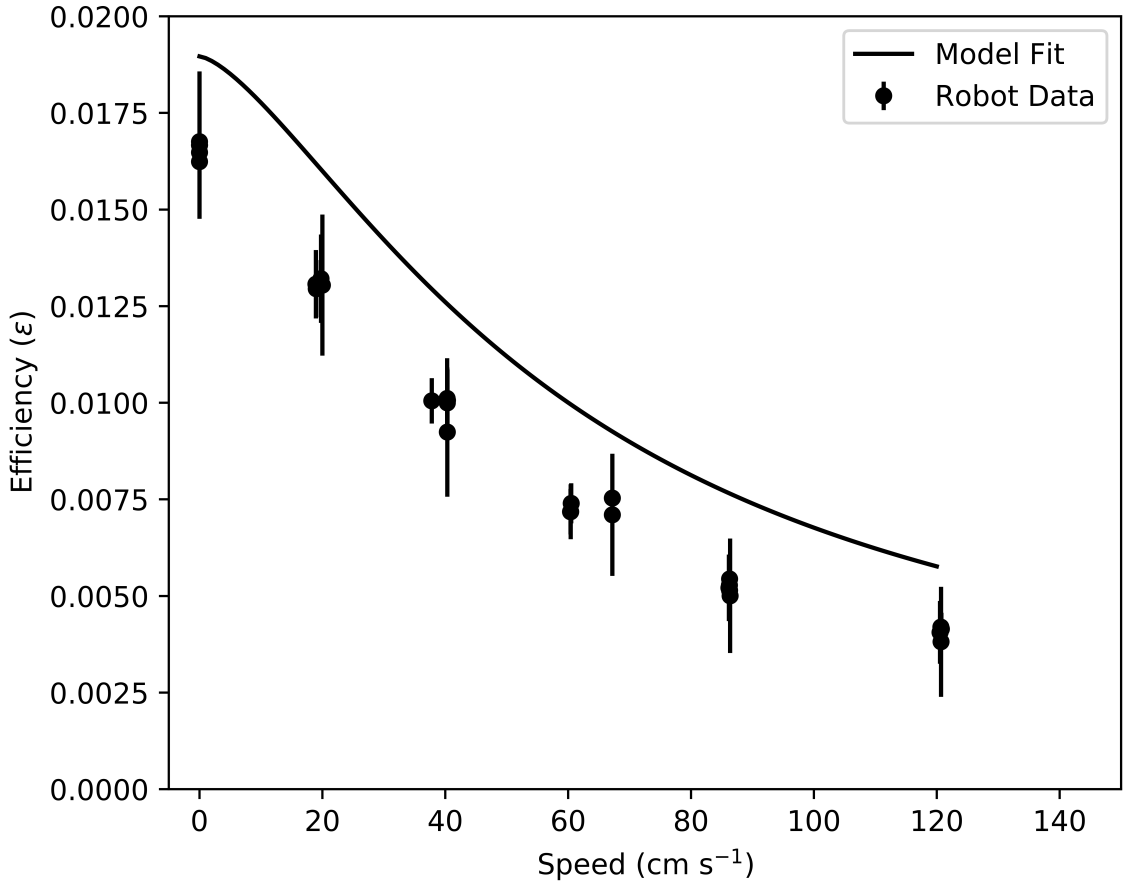

Figure 3.6: Plot of robot data and M4PL fit as a function of speed. The fit and data show the characteristic shape of efficiency starting at a relative high, ending at a relative low, and exhibiting a transition region of rapid change in between.

A plot of the MDA as a function of speed for this experimental setup demonstrates that as speed increases, MDA also increases, Fig. 3.7. As in Fig. 3.6, there appears to be two trend-lines in the experimental data. The data begin at 0 cm s^{-1} with calculated MDAs of approximately 0.114 and increase slowly until approximately 20 cm s^{-1} with MDAs of approximately 0.144. From there the trend line continues to increase with a sharper slope until 120 cm s^{-1} with MDAs of approximately 0.465. Plotted with the experimental data is the efficiency model derived by Falkner et al. input into the MDA equation. Error bars on the experimental data extend two

standard deviations. For example, if regulations require that the MDA be 0.2 μCi of ^{137}Cs the fastest speed the detector would move is approximately 65 cm s^{-1}. If the operational constraints require the speed to be 100 cm s^{-1} then the MDA would be 0.28 μCi of ^{137}Cs.

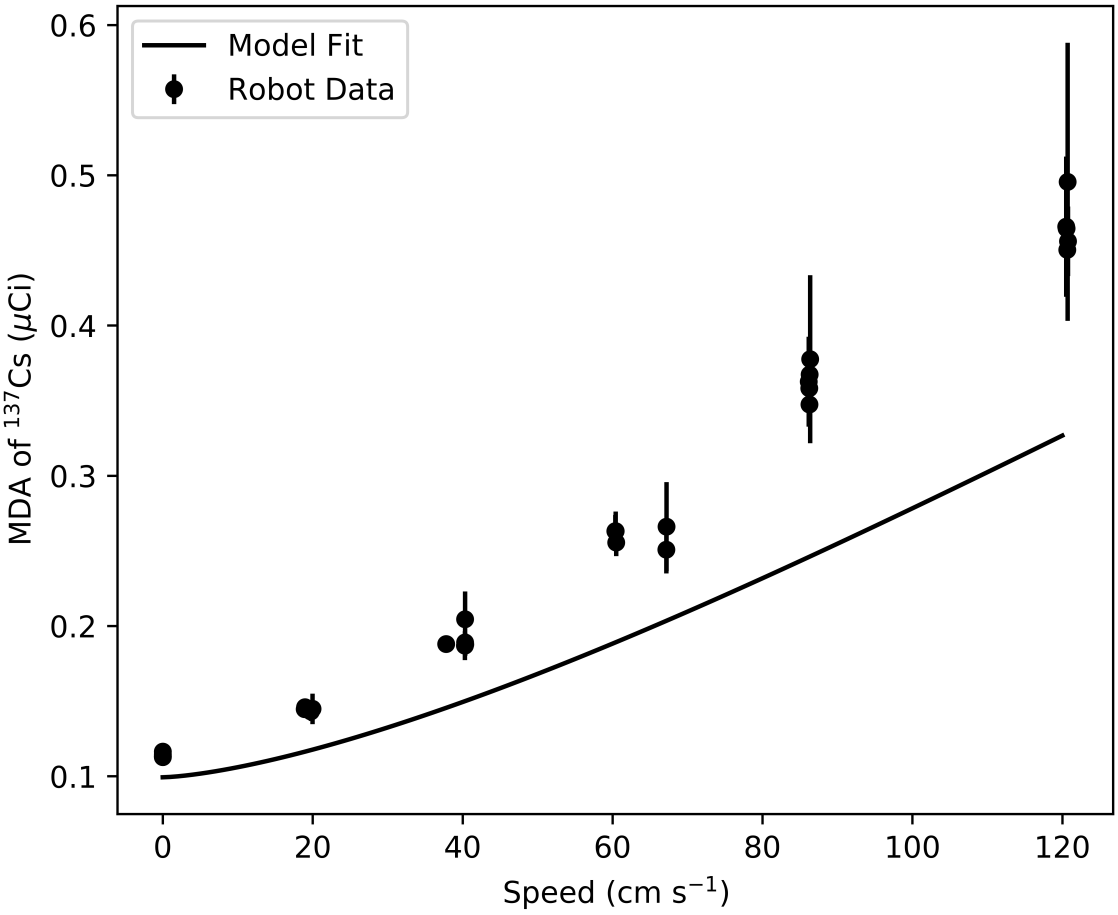

Figure 3.7: Plot of robot data and MDA fit.

Another way of estimating MDA as a function of speed is to plot the count totals for each source and speed cohort and then fit a linear regression to each data set. The result of this analysis is shown in Fig. 3.8. The minimum number of sources that this experiment's detector could see at a particular speed (MDA) is where each line crosses the limit of detection determined above.

The MDA is directly calculated using this method as opposed to being derived by theoretical calculations as in the previous method. This independently verified that the MDA calculated from the efficiency model fit the experimental data and lends credence to the results discussed above.

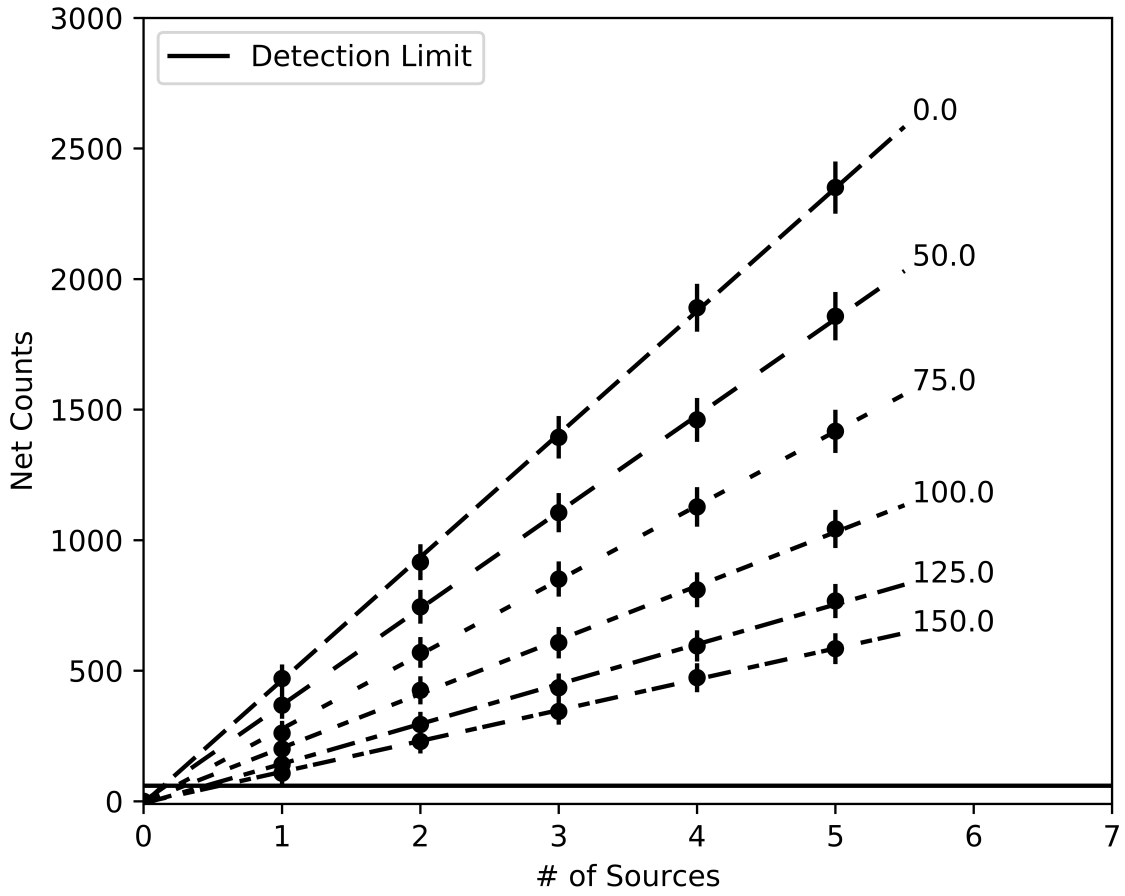

Figure 3.8: Plot of robot data and linear fits. Each dashed line represents a different speed, listed to the right. The plots are the average trial at each source strength at each speed. The solid line is the calculated detection limit based on the background.

The experimentally derived MDAs along with the M4PL model calculated MDAs are plotted in Fig. 3.9. Similar to Fig. 3.7 there appears to be two positive phases with differing slopes. The

first trend starts at 0 cm s^{-1} and ends at approximately 20 cm s^{-1} and is the shallower of the two. The second trend-line starts at 20 cm s^{-1} and extends to the end of the plot at 120 cm s^{-1} and is steeper than the first. The model MDAs are within two standard deviations of the experimental data and again confirms that the model is applicable to this laboratory setting.

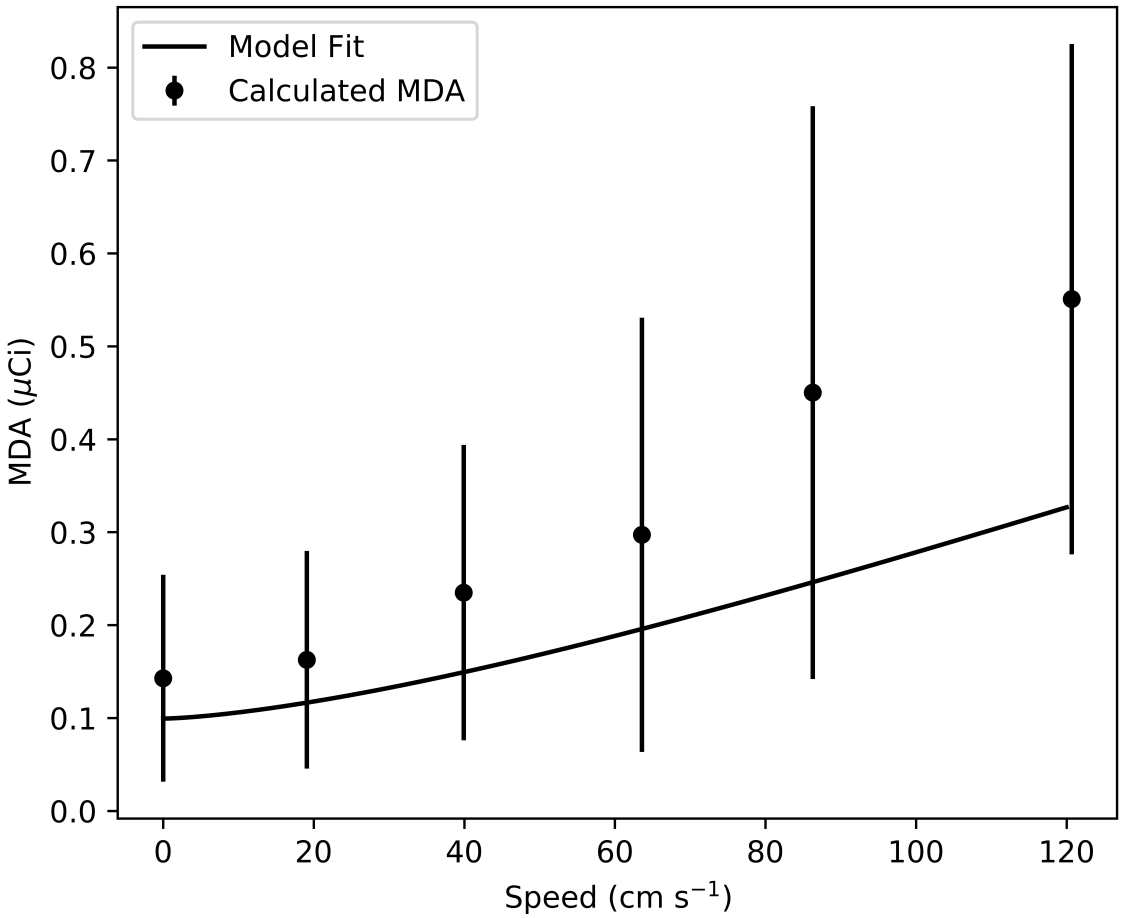

Figure 3.9: Plot of robot data and model fit.

3.4 Summary

It has been known for some time that the efficiency of a moving detector can be improved by slowing the speed of travel. The effect of speed on detector efficiency was mentioned in the MARSSIM manual for conducting environmental site surveys for the decommissioning of facilities. Marianno identified the phenomenon in his data when evaluating the performance of a Field Instrument for the Detection of Low-Energy Radiation. This phenomenon also has real world ramifications for conducting security sweeps using mobile detection systems. There are three main reasons for addressing this issue. First, a surveyor may want to validate the detection system for surveys he performs. The detector uses either an efficiency defined by the manufacturer or more likely an efficiency needs to be calculated. Either way it is most likely an efficiency calculated in a static configuration. However, when using the detector in a mobile configuration the efficiency degradation due to speed may invalidate the results. Second, a surveyor can use this relationship to improve his survey plan. A surveyor has a detector and needs to survey a site as part of a job. It is known how efficient the detector is when static but how fast the detector can move and still meet the designed survey parameters is not known. Finally, a surveyor can use this relationship to identify the limits of the detection system being used due to constraints outside the control of the surveyor. The surveyor has the same detector as the first two cases with a known efficiency, however it is on a flying drone that has a minimum cruising speed it must maintain. The surveyor is interested in knowing what the lowest amount of radiation is that can be seen with this detector on the drone.

This current research sought to reproduce in a laboratory setting the modeled relationship with as few outside confounders as possible. Confounders here includes variable backgrounds, presence of multiple sources, and presence of excess attenuators (tall grass, shrubs, trees, walls, buildings, etc.) or terrain (broken soil, undulating hills, culverts, etc.) that would inhibit an isotropic source. The robotic system allowed for reproducing consistent trial conditions for

the duration of the study. Most critically this included operating at a consistent desired speed for each trial but it also allowed for detector to be held in the same place relative to the robot for every trial. This allowed the trial results to be as consistent to the modeling as possible. The parameters held constant from trial to trial included track length, radionuclide selected as a source, source location, background, detector height, and integration time. Track length was critical because it was used, along with precise timing of each trial, as the means of determining trial speed. The source location and detector height were defined by the modeled parameters. The source used, background, and integration time used were analogs for parameters in Eq. 3.2. The parameters that varied from trial to trial included speed and source strength. Source strength was varied to provide an alternate means of verifying model results. The speed varied because it was the parameter of interest in this research.

The experimental data demonstrate a general decreasing trend as speed increases similar to the modified 4-parameter logistic function relationship (M4PL) derived in (Falkner & Marianno, in prep 2018a). Two portions in the episodic data align well with the general shape of the curve in the model. Additionally, the model falls within two standard deviations of all data points. Thus there is significant agreement between the M4PL and the experimental data. This confirms that the M4PL relationship holds true under experimental conditions and is an accurate model for the influence of speed upon efficiency. The M4PL can then be inverted and placed in Eq. 3.2 to generate an MDA curve. It is this curve that a surveyor would be most interested in. In general the MDA curve starts low and as speed increases rises. The slope of the MDA curve starts shallowly at first but very quickly becomes quite sharp. The data points from this research match the modeled fit very well. This is the first time this relationship has been experimentally confirmed. The Marianno data has the shape of this relationship but that work did not identify the model needed to reproduce it. Utilizing this fundamental relationship allows surveyors to validate current survey plans, design more efficient surveys, or understand survey limitations based upon operational constraints.

4. VALIDATING MINIMUM DETECTABLE ACTIVITY TO DETECTOR SPEED RELATIONSHIP

4.1 Introduction

Radiological surveying occurs in a wide variety of situations with multiple applications. Example surveys include laboratory assessments of reference sources, decommissioning surveys performed to meet regulatory requirements, and identifying source locations and concentrations via vehicle or aircraft mounted systems. It has been observed that detector efficiency is negatively impacted by increasing detector speed, (Marianno et al., 2000; Marianno, 2015). Previous research fit a modified four parameter logistic (M4PL) function to modeling and laboratory results of a 2 x 2 in (5.08 x 5.08 cm) right circular cylinder NaI detector to explain this effect, (Falkner & Marianno, in prep 2018a, in prep 2018b). While standards for performing surveys have been developed, (U.S. NRC, 2000), the varying demands of these applications require a variety of detector types besides right circular cylinder detectors to best achieve the necessary results.

The modified function, Eq. 4.1, is a form of the four parameter logistic function (M4PL) commonly found in biochemistry, (Sittampalam et al., 2004). The original function starts at a minimum value and curves to a maximum value. The M4PL modifies this so that the shape of the curve is mirrored and begins with a region of relatively high efficiency and ends with a region of relatively low efficiency. In between is a transition region of decreasing efficiency. This decrease is gradual at first, quickly steepens, and then shallows out. In this function the speed of the detector is x, the maximum efficiency is A, the minimum efficiency is D, the slope of the equation is B, and the speed at which the efficiency is half that of the maximum is C.

$$\epsilon = D + \frac{A - D}{1 + \left(\frac{x}{C}\right)^B} \tag{4.1}$$

Previous experiments to verify the M4PL were conducted in an indoor laboratory environment on a small scale in terms of detector size, vehicle speed, and distance from the source, (Falkner & Marianno, in prep 2018b). This current research was conducted on a larger scale using a slab detector mounted to a truck. The truck traveled at higher speeds on an outdoor track that was longer and located farther from the source. This was done to extend results to a more realistic scenario while maintaining control over vehicle speed and allowing for multiple trials at each speed/source cohort for reproducibility.

In addition to large scale vehicle trials conducted by the researcher, aerial data was provided by two government partner groups. Air surveys are regularly being conducted as a part of various government agency programs. For example, the Aerial Measuring System (AMS) is operated by the Department of Energy (DOE) to provide radiological support services for the purposes of national security and radiological response, (AMS, 2018). They operate a multi-slab detector system mounted on a rotary-wing aircraft designed to respond to radiological emergencies. Additionally, the Environmental Protection Agency (EPA) operates the Airborne Spectral Photometric Environmental Collection Technology (ASPECT) to provide emergency response capabilities of a radiological nature, (EPA, 2018). The EPA system employs a similar multi-slab detector system mounted on a fixed-wing aircraft. This research evaluated survey data from each of these agencies and compared this real-world data to the M4PL.

This current research extended the M4PL to larger, more complex systems and environments to validate its use in real world survey plans. To do this final results were converted to minimum detectable activities (MDA) to assess performance of the different detection systems, Eq. 3.2. MDA is the lowest level of activity present which can be detected with statistical confidence. The components of Eq. 3.2 are yield Y, integration time T, limit of detection L_D, and efficiency ϵ. Evaluating Eq. 3.2 for efficiency while fixing the limit of detection, integration time, and yield enabled the derivation of a relationship that can be used by field surveyors to quickly tailor their survey plans to be as accurate as needed while remaining cost effective.

$$MDA = \frac{N_D}{Y\epsilon T}, \tag{4.2}$$

4.2 Methods and Materials

4.2.1 Field Trials

4.2.1.1 Vehicle Trial

This current research looked at vehicle data collected at a normal driving speed and at greater distances from sources than previous work, (Falkner & Marianno, in prep 2018b). Due to the larger scale an optical sensor to trigger the start and end of each trial was impractical. To counter this challenge, manual initiation and termination of the count was necessary. This resulted in variable count times within a range of target speeds. The count information was gathered in a similar process to previous research, (Falkner & Marianno, in prep 2018b).

To imitate a vehicle mounted monitoring system similar to the ones used by homeland security or a police force, a simple detector setup was mounted on a pickup truck with no special modifications. The detection system was a 2 x 4 x 16 in (5.08 x 10.16 x 40.64 cm) sodium iodide (NaI) slab detector mounted in a polyvinyl chloride (PVC) holder filled with polystyrene foam. The detector was strapped to the passenger side roof rack with the long axis of the detector parallel to the direction of travel and approximately 2 m above the ground. It was connected to a Canberra Osprey Multichannel Analyzer (MCA) in MCS mode with an integration time of 0.02 seconds and operated using the Canberra Software Development Kit via Python script. The equipment used in this experiment are list in Table 4.1 and shown in Fig. 4.1.

Table 4.1: Equipment used in the vehicle portion of experiment.

Equipment	Description
Vehicle	Truck with roof rack
Detector	2x4x16 NaI slab detector
MCA	Canberra Osprey
Software	Python w/ SDK
Sources	0.4 mCi 137Cs sealed sources (x5)

Figure 4.1: Vehicle with detections system mounted on roof rack.

The vehicle field trials were conducted at Fan Field located near the Bush School at Texas A&M University, College Station, TX, Fig. 4.2. Fan Field is a gravel overflow parking lot only used during football games and other high attendance events. The track consisted of two lanes approximately 5 m wide each and extended approximately 300 m. A 60 m section in the middle of the of the 300 m length was marked out using orange cones. As the truck passed the cones the timer would be manually started and stopped. Due to the inexactness of speed control and the short distances available, the speeds varied for each pass. The truck was driven at target speeds of 10, 20, 30, and 40 mph. The truck drove up one lane and down the other in such a manner that the detector was always on the side towards the source location.

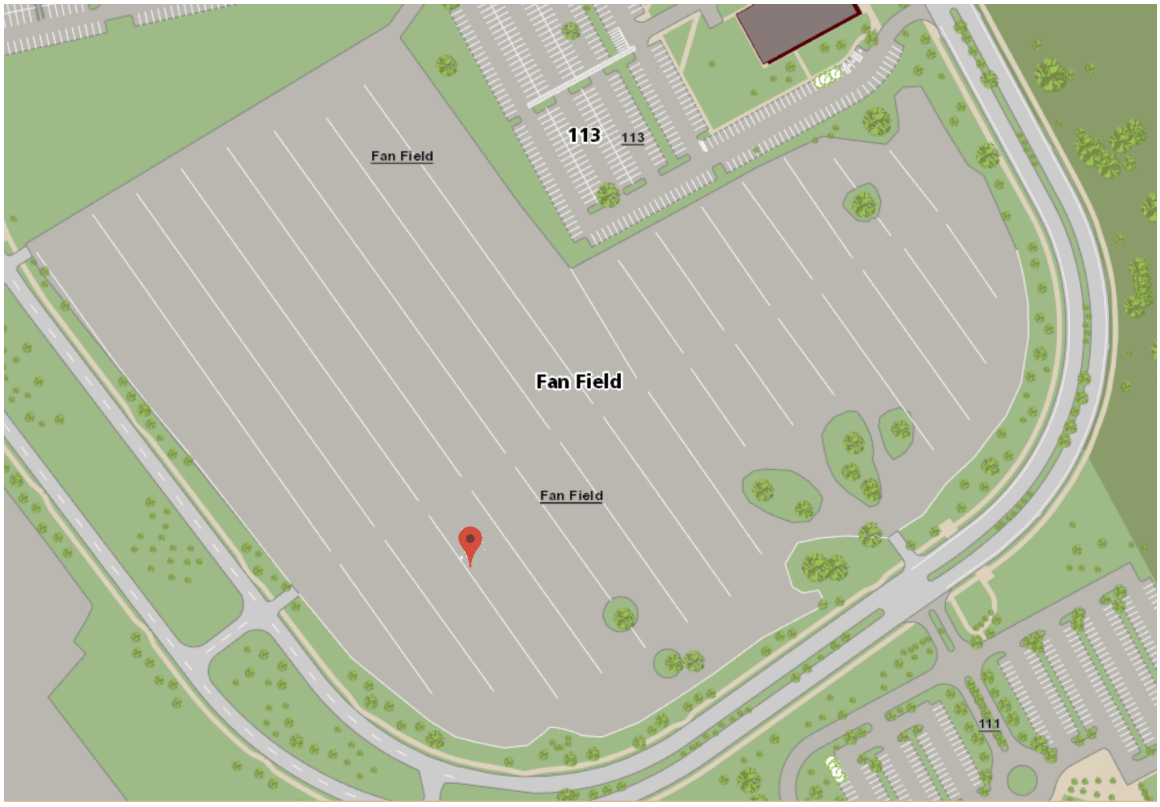

Figure 4.2: Diagram of field where truck trials were conducted. Red arrow is general location of where sources were placed. White lines indicate lanes on either side of sources that truck was driven.

The 0.4 mCi ^{137}C sources used in this experiment were placed in the middle of the 60 m timing section of the track. Four trials were conducted at each target speed for each source strength. Dynamic trials started with background counts and the number of sources increased by one to a maximum of five sources.

A typical background total count is shown in Fig. 4.3. The portion of the count in the gray box is what was used to calculate the average background count per integration time. The first and last fifty counts were disregarded to further ensure only data gathered at desired speeds was used. These values were for 0.02 s integration periods and needed to be multiplied by 50 to calculate an average 1 s background count rate for each trial. The average background count rate and standard deviation was then calculated for all target speeds. This average background count rate was used when calculating net values for the rest of this experiment.

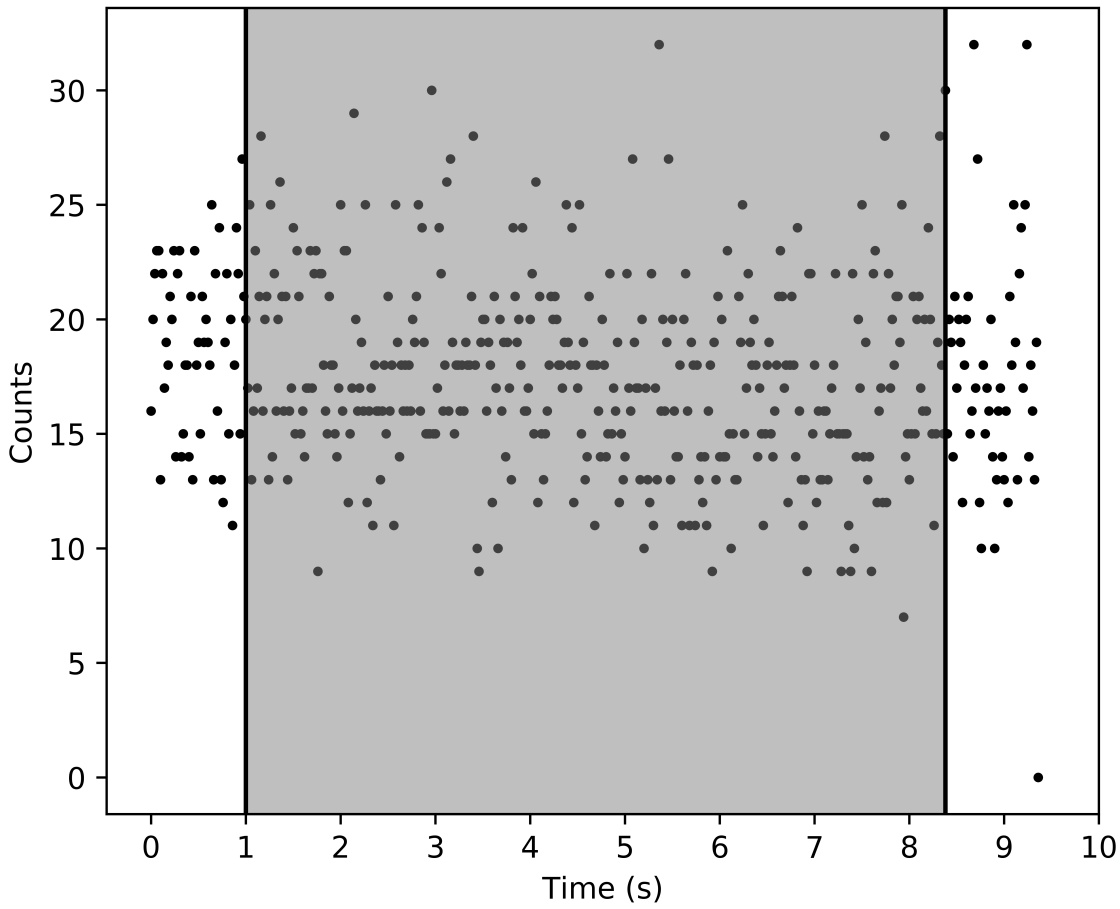

Figure 4.3: Plot of typical MCS background count profile is shown for illustration purposes. The target speed of this trial was 30 mph but the profile is indicative of all background trials, regardless of target speed. Counts in gray region were used to calculate the background count rate.

For trials where sources were present, the maximum count recorded was assumed to be the peak signal indicating the location of the source. A typical source count is shown in Fig. 4.4. The portion of the count in the gray box illustrates what was used to calculate the peak count per integration time. In order to compare the experimental results to modeling results, all peaks were normalized to one second by summing fifty 0.02 s counts centered on the maximum. Each count was the total photons recorded during the integration time. A net peak count was then calculated

by subtracting the background count value. The peak counts were averaged within each throttle setting and source strength cohort. The efficiencies for each throttle and source strength cohort were calculated using the decay corrected activity of the sources used and then plotted against the M4PL model.

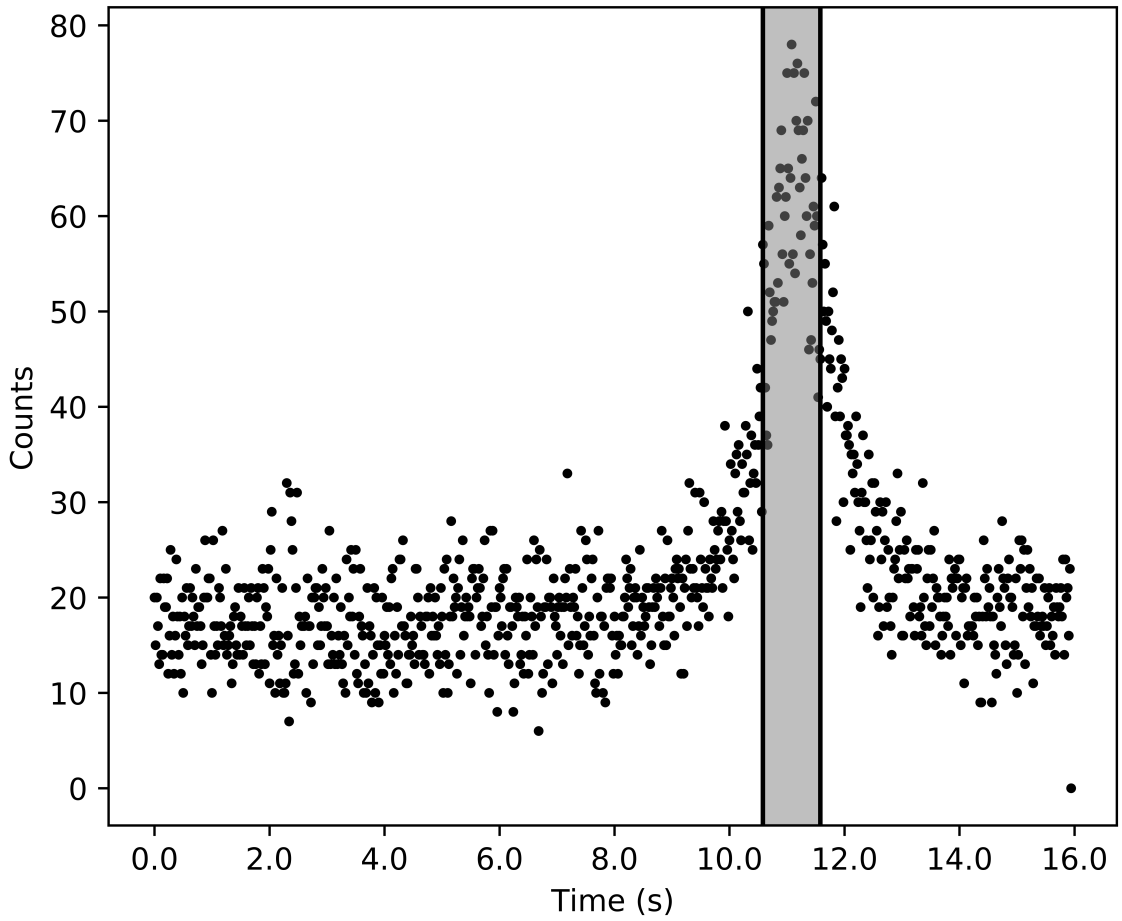

Figure 4.4: Plot of typical MCS source count profile shown for illustration purposes. This trial used two 0.4 mCi sources and a target speed of 20 mph but the shape of the profile is indicative of all source trials. Counts in gray region were used to calculate the peak count rate.

4.2.1.2 Flight Data

The DOE provided rotary wing aircraft flight survey data consisting of date, time stamp, latitude, longitude, altitude, and count rate in counts per second (cps). The data provided was collected in 2009 at an undisclosed testing facility and was collected using a total of twelve NaI slab detectors in four RSX-3 systems mounted on a Bell-412 helicopter, (RSI, 2018; AMS, 2018). The detection system was turned on at the beginning of the flight, operated continuously for the duration of the flight, and turned off prior to landing. Trials consisted of flying over a line of point sources at a target speed of 70 knots and a target height of 100 ft. Sources used were 5.8 mCi ^{60}Co, 27 mCi ^{137}Cs, 8.2 mCi ^{133}Ba, 19.1 mCi ^{241}Am at approximately 500, 1000, 1500, and 2000 m along the track, respectively. Only the ^{137}Cs source was considered for this research. The equipment used by these groups are list in Table 4.2 and shown in Figs. 4.5,4.6.

The EPA provided flight data for a fixed wing aircraft detection system consisting date, time stamp, latitude, longitude, altitude, and count rate in counts per second (cps). The particular data provided was collected in 2010 at an undisclosed testing facility and was collected using a total of eight slab detectors in two RSX-4 detectors and mounted in a AeroCommander-680FL fixed-wing aircraft, (RSI, 2018; EPA, 2018). As with the DOE flight, the detection system was turned on at the beginning of the flight and operated continuously until the end of the survey period. Sources used by the EPA were 5.0 mCi of ^{60}Co and 26.2 mCi of ^{137}Cs located at approximately 500 m and 2000 m along the track, respectively. Only the ^{137}Cs source was considered for this research.

Table 4.2: Equipment used by AMS and ASPECT to gather data.

DOE	
Equipment	Description
Aircraft	Bell-412
Detector	RSX-3 (x4)
MCA	ADS
Software	RadAssist
Sources	5.8 mCi ^{60}Co, 27 mCi ^{137}Cs,
Target Height	20 m
Target Speed	70 kt

EPA	
Equipment	Description
Aircraft	AeroCommander-680FL
Detector	RSX-4 (x2)
MCA	ADS
Software	RadAssist
Sources	5.0 mCi ^{60}Co, 26.2 mCi ^{137}Cs,
Target Heights	30 m and 45 m
Target Speed	110 kt

Figure 4.5: Aircraft used to gather the data provided. The left aircraft was used by the DOE and the right aircraft was used by the EPA. Reprinted from AMS, 2018 and EPA, 2018.

Figure 4.6: Detectors used to gather the data used in this research. The left detector is an RSX-3 used by the DOE and the right detector is an RSX-4 used by the EPA. Reprinted from RSI, 2018.

Individual passes in both aerial data sets along the test track were identified by selecting data points within a rectangle drawn using open-source QGIS and exported for further evaluation, (Team, 2017). Each individual pass was identified in the exported data by locating time stamp deviations greater than 5 seconds, Fig. 4.7. Each group of data between these deviations was considered one pass and was evaluated for pass speed.

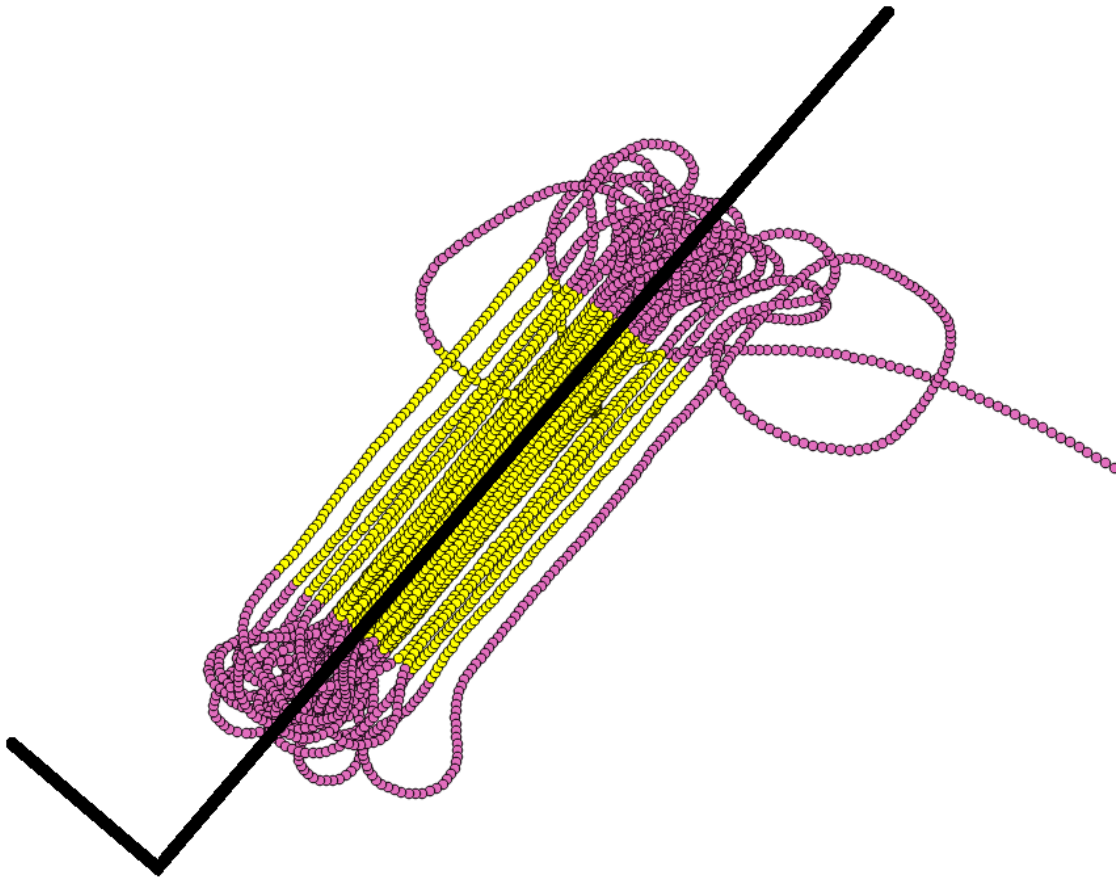

Figure 4.7: Representation of flight data. Purple dots represent all data provided. Yellow dots represent data selected in this research to construct individual passes. Axes are superimposed for reference. The long axis represents distance along track. The short axis represents offset from the track.

The lateral track offsets from the ^{137}Cs source and height above ground of each data point in the trials were calculated, Fig. 4.8. The maximum count rate from each trial that was within approximately 60 m of the source was chosen for analysis. The offset of 60 m was chosen to account for counts not taken directly over the source location and any error in GPS positions. Some trials in both the DOE and EPA datasets did not have counts that were taken within 50 m of the source location and were thus discarded. The height varied by about 100 m during each

trial. The changing height profile is important because in a 1 s count the height would change approximately 1.4 m and 2.3 m at speeds of 70 kt and 110 kt, respectively. This is not enough to invalidate the experimental data but will contribute to any variation. In total, four trials were identified from the DOE dataset and eight trials were identified from the EPA dataset.

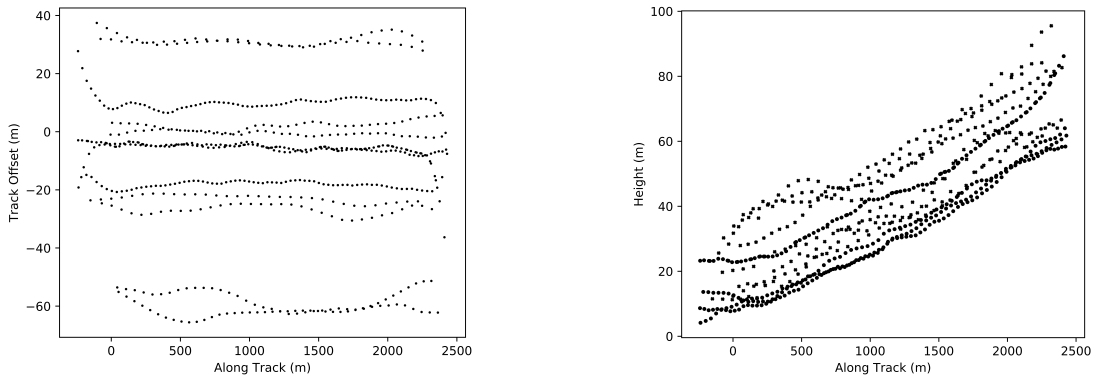

Figure 4.8: Identified tracks from both datasets provided. The left plot is the lateral offset of each trial. The right plot is the height profile for each trial.

4.2.2 Modeling

Similar to previous research a simplified mock up of each detection system was modeled in MCNP, (Falkner & Marianno, in prep 2018a; Goorley et al., 2012). Detection/source schemes modeled are shown in Table 4.3. The schemes chosen were as close to experimental arrangements as possible. Due to inconsistencies inherent to field studies, the aerial tracks varied in survey altitude enough to necessitate the modeling of both a high and low scheme to better simulate survey parameters.

Table 4.3: Various detector/source configurations that were modeled.

Setup	Description
Truck	Height (cm): 200
	Speeds (mph): 0, 10, 15, 20, 25, 30, 35, 40, 45, 50
DOE Low	Height (cm): 2000
	Speeds (kt): 0, 25, 50, 100, 125, 150
DOE High	Height (cm): 4000
	Speeds (kt): 0, 25, 50, 100, 125, 150
EPA Low	Height (cm): 3048
	Speeds (kt): 0, 25, 50, 100, 125, 150
EPA High	Height (cm): 4572
	Speeds (kt): 0, 25, 50, 100, 125, 150

In the case of the vehicle mounted system, a single 2 x 4 x 16 in (5.08 x 10.16 x 40.64 cm) detector was modeled. The detector was wrapped in 0.64 cm of aluminum, approximately 7.62 cm of polystyrene foam, and then wrapped in 0.64 cm PVC. The entire system was placed in a dry air atmosphere. The detector was arranged so that the long axis was oriented in the x-axis and the short axis was oriented in the z-axis. The top plane of the detector was located in the z=0 plane. The source was located 500 cm in the z-axis and 200 cm in the y-axis. This was to mimic the truck experimental design where the source was on the ground 500 cm away from the truck and the detector was on the roof-rack 200 cm above the ground.

In the case of both aircraft, a single detector was modeled to represent the multi-detector systems. The DOE crystal measured 2 x 24 x 32 in (5.08 x 60.96 x 81.28 cm). The EPA crystal measured 2 x 16 x 32 in (5.05 x 40.64 x 81.28 cm). Both aerial systems were wrapped with 1.27 cm of aluminum, 7.62 cm of polystyrene, and 0.64 cm of steel to mimic the detector housing and aircraft frame. Both systems were placed in a dry air atmosphere. Similar to the

truck simulation, the detectors were arranged so that the long axis was oriented in the x-axis and the short axis was oriented in the z-axis. The top plane of each detector was located in the z=0 plane.

Line sources were used to approximate a moving detector over a stationary source because the MCNP version used does not model dynamic configurations. A line source emits photons with equal probability along the entire length of the source. In this way the tally response approximates the detector moving past the stationary source. The length of the line source is equal to the distance the detector would have traveled during the integrated period of interest. For these simulations an integration time of one second was used. Velocities simulated were between 0-50 mph in increments of 10 mph for the truck simulation and 0-150 kt in increments of 25 kt for the aerial simulations.

The photon energy for all MCNP simulations was 662 keV, the energy of ^{137}Cs which is a standard radionuclide used for detector calibration. An F8 tally over the cylinder was used to approximate detector efficiency. The F8 tally measures the energy deposited in the the detector volume and reports the value as efficiency. Each simulation modeled $1x10^9$ particles. A direction bias was applied to the source definition card. The number of particles modeled and the direction biasing was necessary to produce results with relative errors less than 10%.

The MCNP results for each system were fit with the M4PL model. The experimental data was superimposed and comparisons made as to how well the data fit the model. The efficiency results were then converted to MDAs using the detection limits from above, a yield of 0.85 for ^{137}Cs, and an integration time of 1 s.

4.3 Results and Discussion

4.3.1 Vehicle Results

Representative data for vehicle trials at different speeds and source strengths are shown in Fig. 4.9. The broad peak on the left indicates the detector spent more time close to the source

as a result of slower speed. Conversely, the sharper peak on the right is a result of the vehicle passing more quickly and thus receiving fewer photons. Since all data points were taken in 0.02 s intervals, peak width is a reflection of speed. Higher speeds resulted in a sharper peak while lower speeds resulted in a broader peak. Normalized counts of 1 s incorporated 25 counts on either side of the highest value to create a 1-s count. The broader peak of the slower speeds resulted in a wider spread of higher counts and thus produced a more efficient reading. The sharper peak of the faster speeds incorporated a wider range of count values in the normalized 1 s count and so resulted in a lower total count value and reduced efficiency.

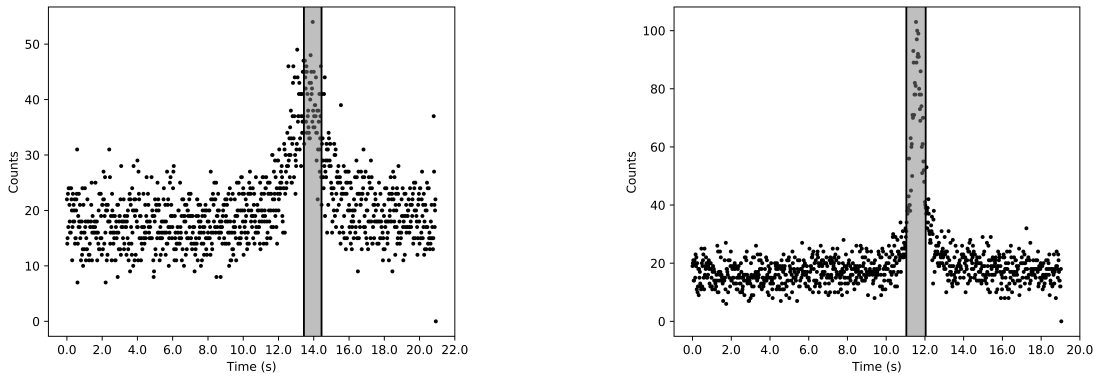

Figure 4.9: Two example truck profiles are shown for illustration purposes. The left profile used one 0.4 mCi source and a target speed of 10 mph. The right profile used three 0.4 mCi sources and a target speed of 30 mph.

Average background counts recorded for each target speed are shown in Table 4.4. The highest value was 878.63 $\pm$ 18.15 cps for the 10 mph cohort. The lowest value was 858.31 $\pm$ 14.99 cps for the 20 mph cohort. Backgrounds for all speed cohorts were within two standard deviations of one another. Thus, as demonstrated in previous research, speed has no effect on background readings even at higher speeds, (Falkner & Marianno, in prep 2018b). As a result, the limit of detection is not affected by speed, and therefore any impact on count totals that speed

may have is only expressed in the efficiency component of Eq. 4.2.

Table 4.4: Background counts for the truck trials.

Speed (mph)	Gross Peak (cps)
10	878.63 ± 18.15
20	858.31 ± 14.99
30	861.02 ± 11.00
40	866.52 ± 23.19

The final experimental average background value was determined to be 866.84 ± 16.72 cps and was most likely influenced by the gravel in the parking lot. This value is low for the Texas A&M campus based upon previous unpublished surveys for laboratory classes. Buildings on the campus typically are constructed with concrete which contributes to high background count rate. Fan Field is located in an area with very few buildings nearby and so has a low background reading. The limit of detection for this experiment was 80.46 counts.

4.3.2 Aerial Results

Examples of the aerial data profiles that were used in this research are shown in Fig. 4.10. The DOE profile shows the source peaks closer to one another. The EPA profile shows the source peaks at opposite ends of the track from each other. Variations in the profiles amongst each system are due primarily to the x-, y-, and z-axis offsets in detection location relative each source. In other words, the precise location of the detector when each count was made was not consistent between profiles. Backgrounds for both the DOE and EPA datasets were calculated by averaging the track counts farthest from the source location. This was because they were most representative of the survey environment while remaining independent of any source influence.

The DOE background was 2129.09 $\pm$ 346.03 cps resulting in a limit of detection of 1611.75 cps. The EPA background was 4790.53 $\pm$ 321.16 cps with a limit of detection of 1496.10 cps.

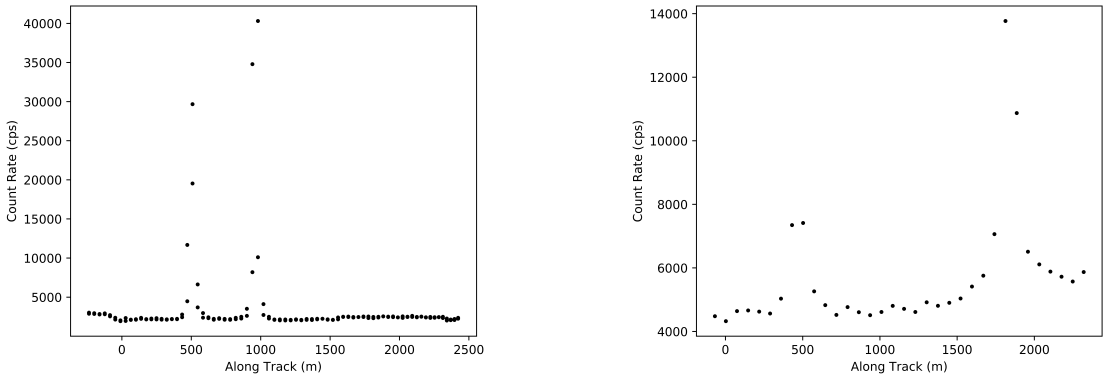

Figure 4.10: Two example aerial profiles are shown for illustration purposes. The left profile is for DOE data. The right profile is for EPA data.

The experiment and simulation results for the truck data are shown in Fig 4.11. The shape of the simulation results can be very accurately modeled with the M4PL. The plot of the simulation results starts with a maximum efficiency of 1.0×10^{-4}. It decreases slowly until approximately 15 mph with an efficiency of 8.6×10^{-5}. The slope then steepens until approximately 50 mph with an efficiency of 4.5×10^{-5} before shallowly decreasing to a minimum efficiency of 3.6×10^{-5}. The experimental data is within two standard deviations of the model results for all speed cohorts. This implies that the model is a good approximation for the truck detector system.

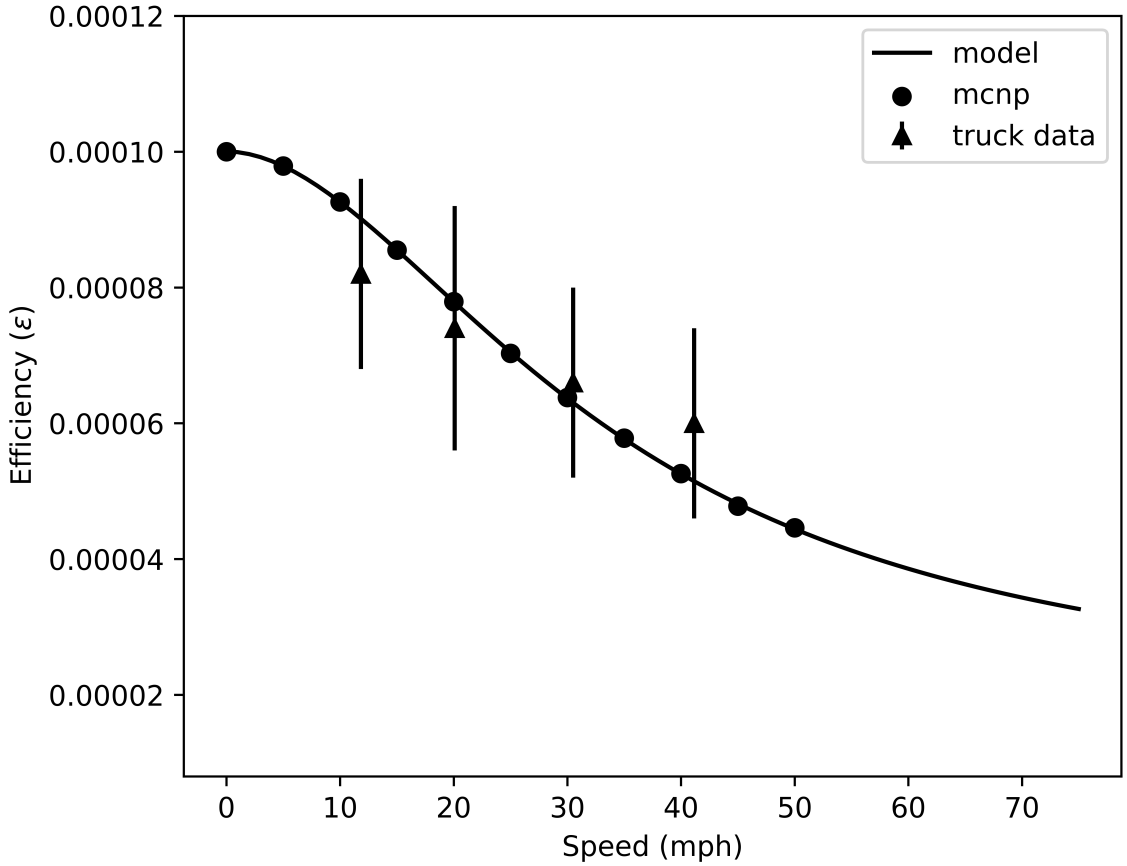

Figure 4.11: Model fit and experimental results for truck trials.

The experiment and simulation results for the DOE and EPA data are shown in Fig 4.13 and Fig. 4.12, respectively. As expected, the efficiencies of the lower altitude models are larger than the efficiencies of the higher altitude models for both the DOE and EPA configurations. In general, the efficiencies of the DOE models are higher than the efficiencies of the EPA models. This is primarily because the heights of the DOE models were lower than the heights of the EPA models indicating that height plays a major role in detector performance. Another possible reason is that the DOE detection system used 4 more slab detectors than did the EPA detection system.

The plot of the 20 m altitude DOE data starts at 0 kt with a maximum efficiency of 5.8×10^{-5}. It

begins sloping downward gently until approximately 25 kt where the slope of the curve steepens until approximately 120 kt with an efficiency of 3.2×10^{-5} before flattening out for the rest of the plot. The plot of the 40 m altitude EPA data begins at 0 kt with a maximum efficiency of approximately 1.4×10^{-5} to a minimum efficiency of 1.0×10^{-5}. There is very little change in change in efficiency and almost no curvature in the 40 m altitude plot. A total of four data points collected for the DOE system are plotted with error bars of two standard deviations. All four data points are clustered around 70 kt. All of the data points have efficiencies within the bounds of the two curves or are within two standard deviations of a curve. The variation in the data points is likely due to the lateral offset from the source and differences from the modeled altitudes.

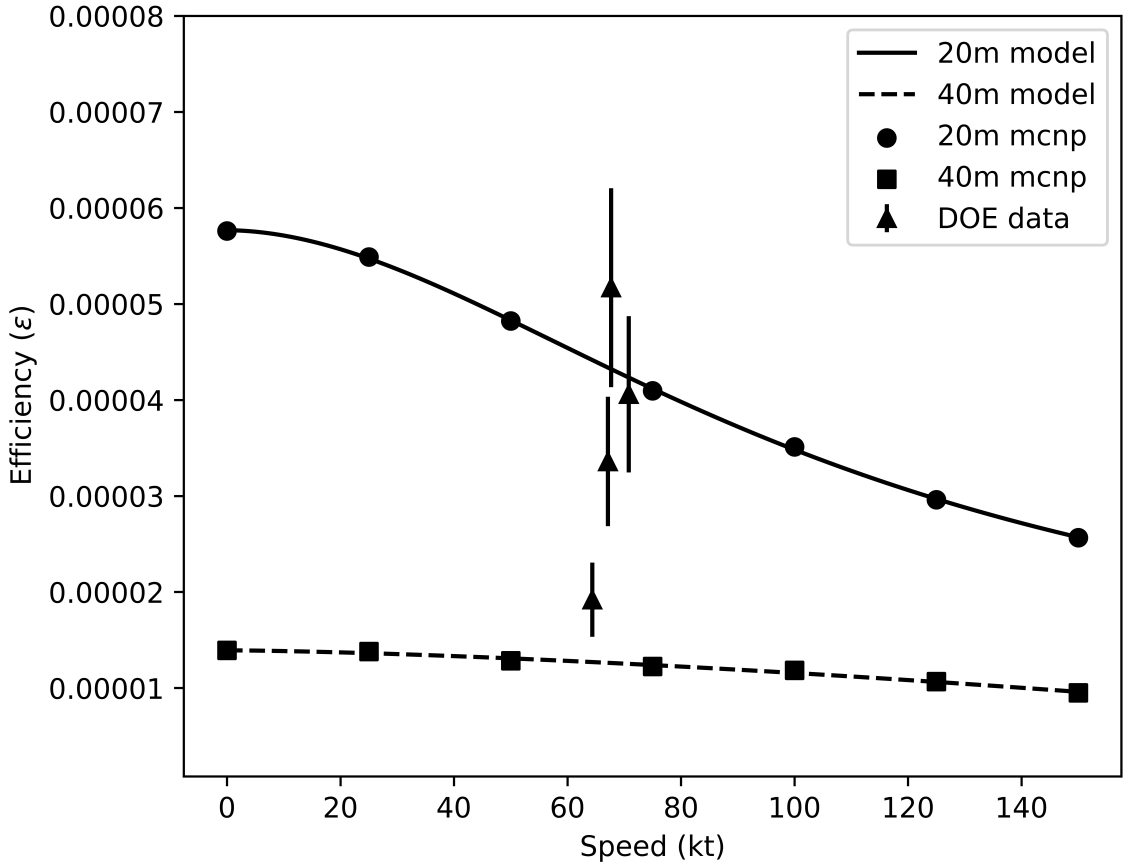

Figure 4.12: Model fit and experimental results for the DOE aerial trials. The lines represent the simulated results and the data points with error bars are the experimental values. All experimental values are within two standard deviations of a model or are between two models accounting for lateral and height offsets.

The plot of the 30 m altitude EPA data starts at 0 kt with a maximum efficiency of 1.6×10^{-5}. It begins sloping downward gently until approximately 40 kt where the slope of the curve steepens until approximately 120 kt with an efficiency of 1.3×10^{-5} before flattening out for the rest of the plot. The plot of the 45 m altitude EPA data begins at 0 kt with a maximum efficiency of approximately 7.5×10^{-6} to a minimum efficiency of 5.0×10^{-6}. There is very little change in change in efficiency and almost no curvature in the 45 m altitude plot. Eight data points collected for the EPA system are plotted with error bars of two standard deviations. The data points are

clustered at approximately 115 kt and 140 kt. Five of the eight data points have efficiencies within the bounds of the two simulation curves. The other three data points have efficiencies that are larger than the 30 m altitude curve. As with the DOE data the variation is likely due to the lateral offset and height difference.

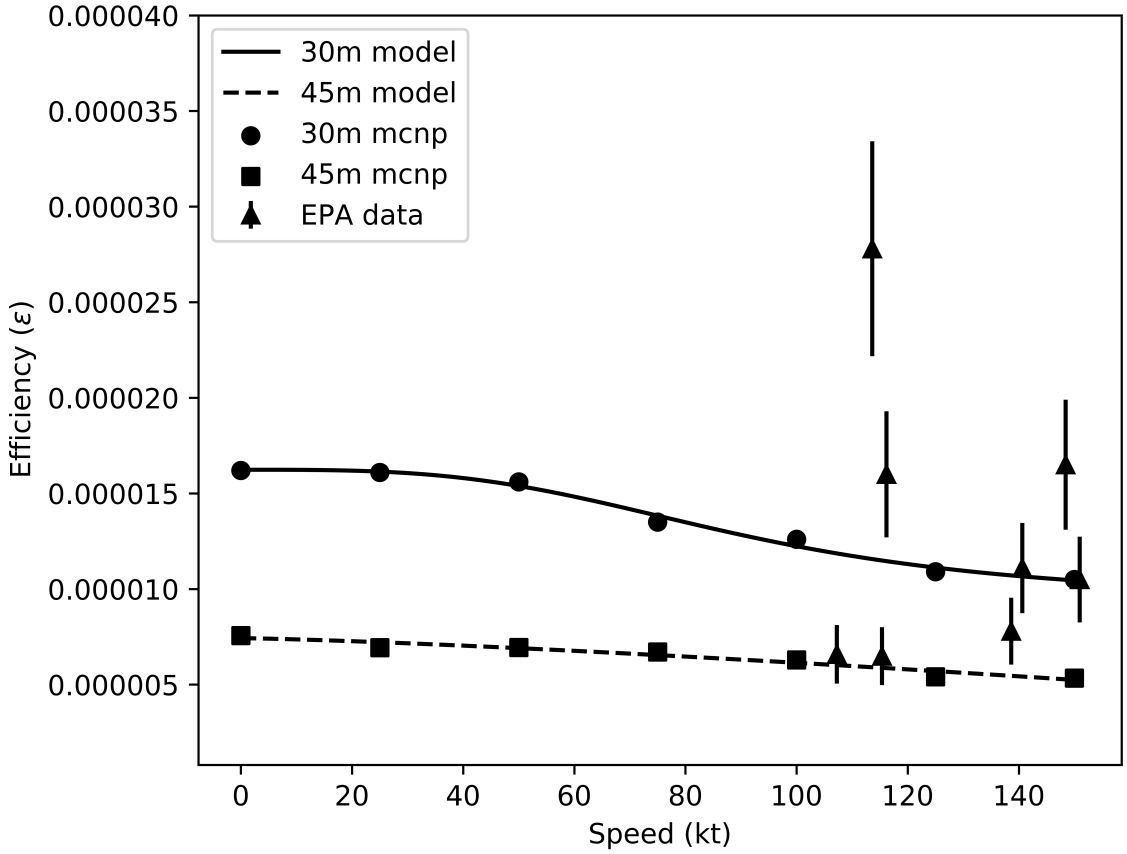

Figure 4.13: Model fit and experimental results for EPA trials. The lines represent the simulated results and the data points with error bars are the experimental values. The experimental values are generally within two standard deviations of a model or are between two models. The data points outside the model fits can be accounted for by lateral and height offsets.

The reason for the difference in efficiency profiles for the two altitudes is because the increased distance has an inverse squared effect on solid angle. The size of the detector as seen

from the source is dramatically reduced at the higher altitude as compared to the lower altitude. This results in fewer photons being captured. Another effect seen is that the points in the curves where the slope steepens and then bottoms out appear to get closer to each other as altitude increases. This is important if the speed of the vehicle can not be consistently maintained at a set speed. The area between these points is the portion of the plot with the highest rate of change in efficiency with speed and thus shrinking this region results in less volatility, however this stability comes at a cost of reduced overall efficiencies for the entire plot. The surveyor must balance their operational parameters against desired precision in results.

Parameters for the M4PL models used to fit the truck, DOE, and EPA systems are listed in Table A.5. As expected the truck system has the largest maximum efficiency, an A of $8.38 \times 10^{-5} \pm 0.01 \times 10^{-5}$, since it is both closest to its source and traveling at the slowest speed. This trend continues with the aerial systems where both low altitude parameters are larger than their respective high altitude parameters. This implies that smaller detectors will suffice when slower speeds are desired or the detector will be operated close to the survey field.

Similarly as expected, the speed at 50% of maximum efficiency, C, increases as size of the detector increases. The smallest detector is the truck system and has a C value of 34.35 $\pm$ 0.70 mph. This is approximately one third that of the aerial systems. The low altitude C values for the aerial systems are approximately equal, but the DOE system is slightly larger at 107.46 $\pm$ 6.44 kt versus the EPA system at 90.58 $\pm$ 12.17 kt. This is reasonable as the DOE system employed twelve slab detectors and the EPA system employed eight. This implies that a larger detector system is required if higher speeds are desired. The conversion from mph to kt is 1 mph is equal to 0.868976 kt.

Table 4.5: Parameters of the 4-Parameter Logistic Function used to fit the various model results.

Setup	A	B	C	D	r^2
Truck	$8.38\text{x}10^{-5} \pm 0.01\text{x}10^{-5}$	1.90 ± 0.03	34.35 ± 0.70	$1.58\text{x}10^{-5} \pm 0.13\text{x}10^{-5}$	0.9999
DOE 20 m	$5.77\text{x}10^{-5} \pm 0.02\text{x}10^{-5}$	1.88 ± 0.09	107.46 ± 6.44	$0.87\text{x}10^{-5} \pm 0.03\text{x}10^{-5}$	0.9998
DOE 40 m	$1.39\text{x}10^{-5} \pm 0.03\text{x}10^{-5}$	1.49 ± 0.67	$2.51\text{x}10^{4} \pm 2.37\text{x}10^{7}$	$-911.26\text{x}10^{-5} \pm 1.28\text{x}10^{1}$	0.9867
EPA 30 m	$1.62\text{x}10^{-5} \pm 0.74\text{x}10^{-5}$	3.30 ± 1.30	90.58 ± 12.17	$0.94\text{x}10^{-5} \pm 0.12\text{x}10^{-5}$	0.9902
EPA 45 m	$0.74\text{x}10^{-5} \pm 0.03\text{x}10^{-5}$	1.30 ± 1.30	$4.98\text{x}10^{4} \pm 9.91\text{x}10^{7}$	$-422.73\text{x}10^{-5} \pm 1.09\text{x}10^{1}$	0.9397

Although the r^2 values are high for all systems, indicating that the M4PL fits the experimental data, the C and D parameters for both high altitude systems are unrealistic. The speeds at 50% of maximum efficiency are approximately 2500 kt for the DOE system and 5000 kt for the EPA system. It is unreasonable to expect radiation surveys to be performed at speeds of thousands of knots. Similarly, the minimum efficiencies for the DOE and EPA systems are approximately -900 and -400, respectively. Negative efficiencies are physically impossible. These unrealistic parameters are due to the height of the systems being far enough above the source that the inverse square of distance dominates any effect of speed. This explains the flat declines in the high altitude efficiency plots. Rather than use these parameters to modify survey plans they should be used as qualitative indicators for when the model breaks down and other factors of the survey plan dominate.

The MDA curve for the truck system was calculated using Eq. 4.2 and the efficiencies above, Fig. 4.14. The yield, integration time, and detection limit were as detailed above. The curve exhibits the shape of the MDA curve from previous research, (Falkner & Marianno, in prep 2018b). The truck curve starts at 0 mph with an MDA of 26 μCi of ^{137}Cs and begins to rise. The slope of the rise is shallow until approximately 20 mph with an MDA of 34 μCi of ^{137}Cs. The MDA then rises steeply until 70 mph where the plot ends with an MDA of 76 μCi of ^{137}Cs. The

MDAs for the experimental truck data is within two standard deviations of the simulated curve with the exception of the last data point for the 40 mph cohort. For example, if regulations require that the MDA be 40 μCi of ^{137}Cs the fastest speed the detector would move is approximately 30 mph. If the operational constraints require the speed to be 50 mph then the MDA would be 58 μCi of ^{137}Cs.

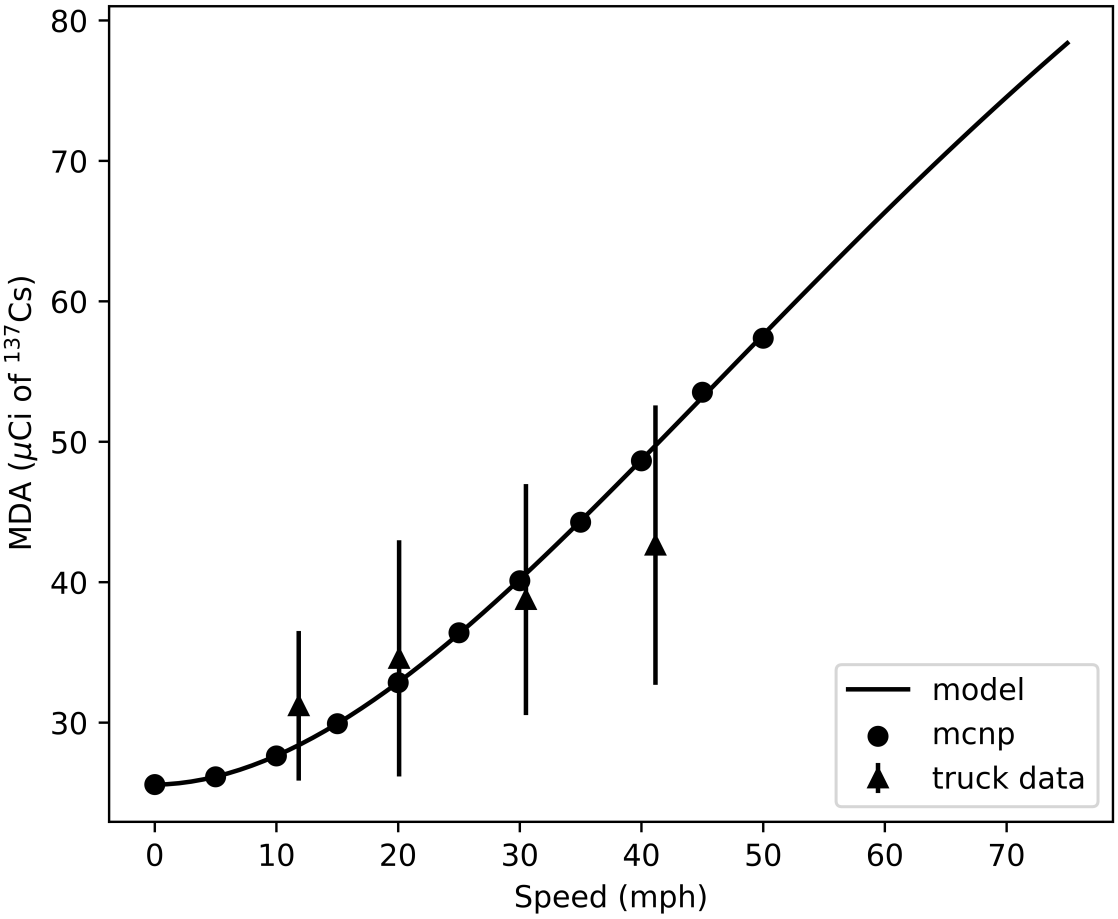

Figure 4.14: MDA for ^{137}Cs based on experimental parameters from truck data.

The DOE 20 m altitude curve starts at 0 kt with an MDA of approximately 0.9 mCi of ^{137}Cs. The curve starts rising imperceptibly until approximately 40 kt and an MDA of 1.1 mCi of ^{137}Cs.

From there the slope of the curve increases until the maximum MDA of 1.9 mCi of ^{137}Cs. The DOE 40 m altitude curve starts at 0 kt with an MDA of 3.8 mCi of ^{137}Cs. The curve starts rising until 80 kt and an MDA of 4.0 mCi of ^{137}Cs. There the slope of the curve increases until the maximum MDA of 5.4 mCi of ^{137}Cs. Unlike the efficiency curves, the 40 m altitude curve is a mirror image of the 20 m altitude curve. Similar to the efficiency plot, the experimental data are clustered near the 20 m curve with a single data point in the middle between the two curves. All data points are either within the two curves or is within two standard deviations of the 20 m curve, implying the M4PL can explain the experimental data, accounting for lateral and height offsets of the data from the modeled parameters. For example, if regulations require that the MDA be 1 mCi of ^{137}Cs the fastest speed the detector would move at 20 m altitude is approximately 45 kt. If the operational constraints require the speed to be 140 kt at 20 m altitude then the MDA would be 2 mCi of ^{137}Cs.

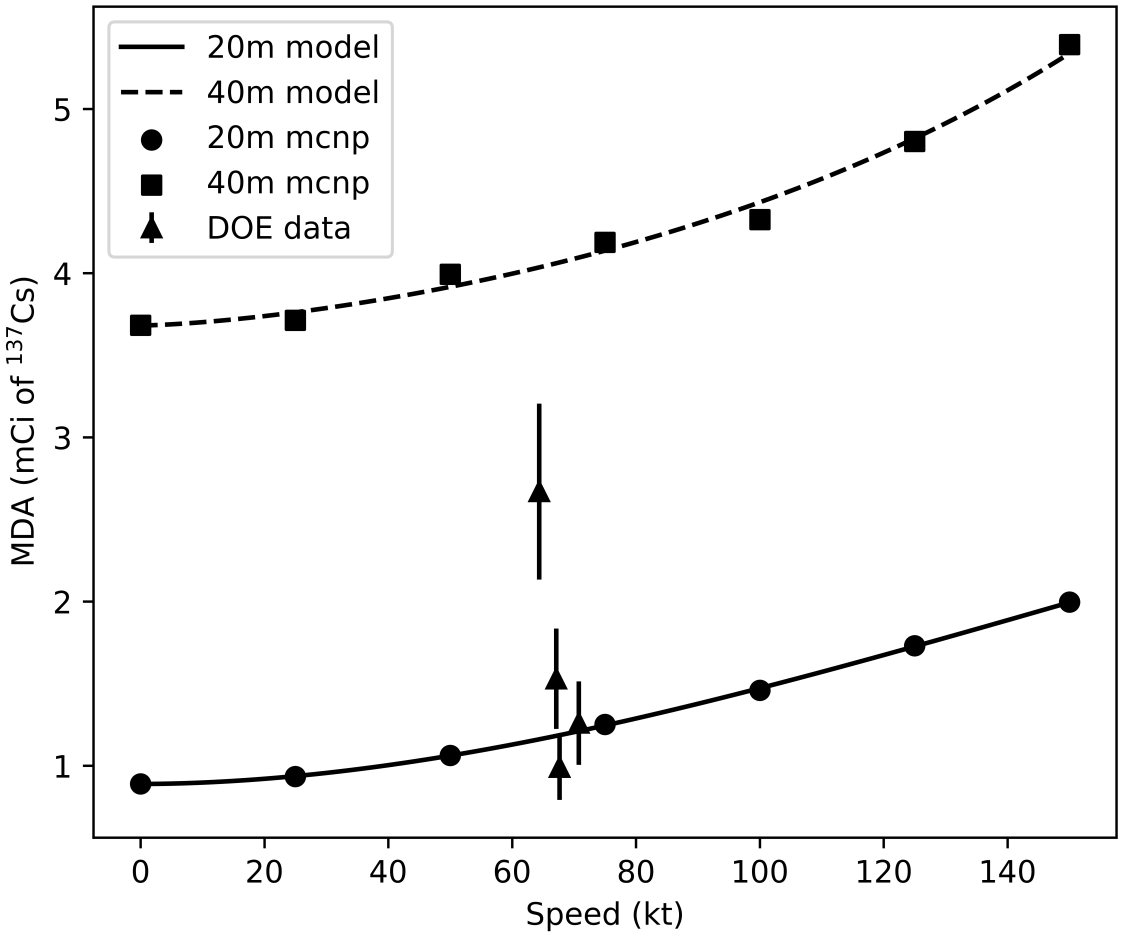

Figure 4.15: MDA for ^{137}Cs based on experimental parameters from AMS data.

The EPA 30 m altitude curve starts at 0 kt with an MDA of approximately 3.0 mCi of ^{137}Cs. The curve starts rising imperceptibly until approximately 40 kt and an MDA of 3.5 mCi of ^{137}Cs. From there the slope of the curve increases until the maximum MDA of 1.9 mCi of ^{137}Cs. The EPA 45 m altitude curve starts at 0 kt with an MDA of 6.5 mCi of ^{137}Cs. The curve rises continuously until the maximum MDA of 8.5 mCi of ^{137}Cs. Unlike the efficiency curves, the 45 m altitude curve is a mirror image of the 20 m altitude curve. Five of the eight data points are bounded between the two curves or within two standard deviations of the 30 m curve,

implying the M4PL is a good fit for the experimental data. The three points that are outside of two standard deviations of the 30 m curve are below the curve due to variations in height and lateral offset from the source. For example, if regulations require that the MDA be 3 mCi of ^{137}Cs the fastest speed the detector would move at 30 m altitude is approximately 40 kt. If the operational constraints require the speed to be 140 kt at 30 m altitude then the MDA would be 4 mCi of ^{137}Cs.

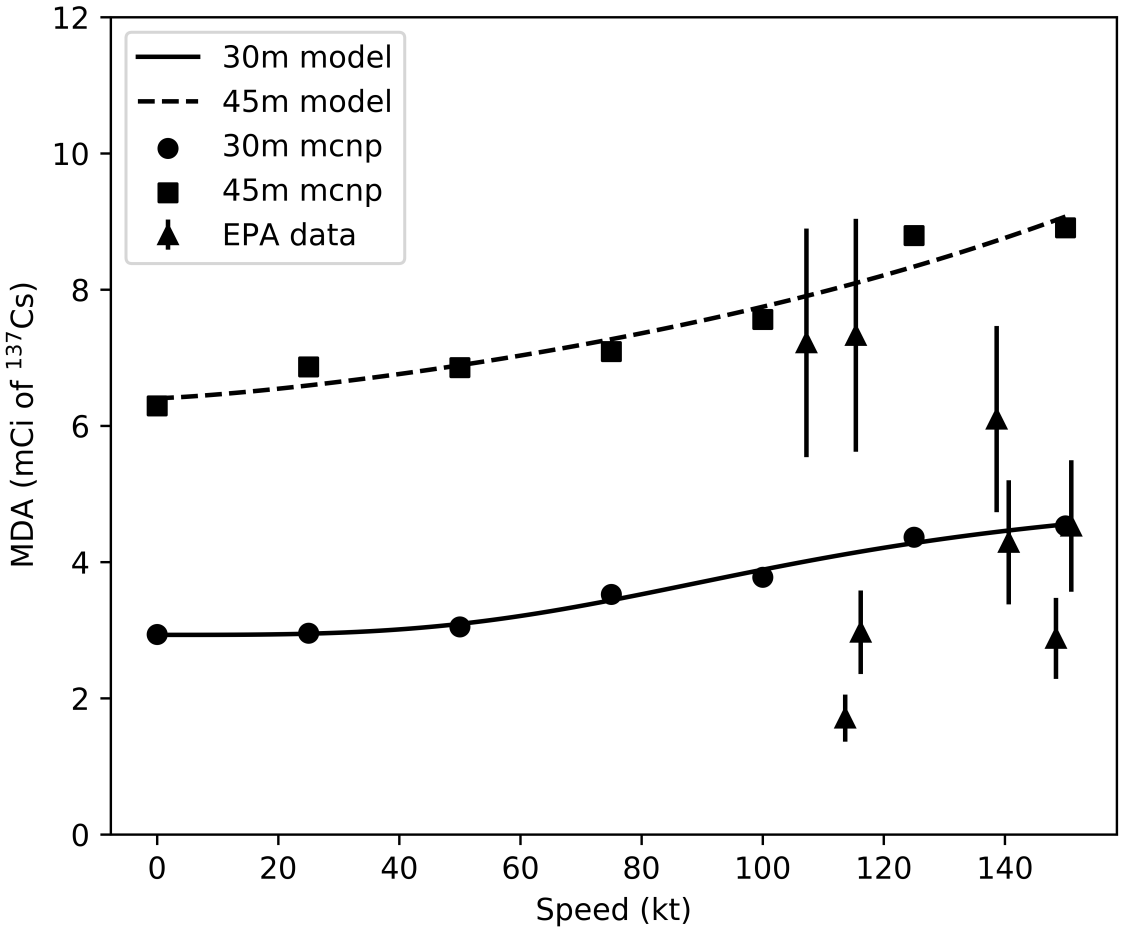

Figure 4.16: MDA for ^{137}Cs based on experimental parameters from EPA data.

All plots exhibit the inverse relationship between efficiency and MDA, as seen in Eq. 4.2. This relationship is the reason for the linear slope to the high speed portion of the MDA curves. Because efficiency is in the denominator of Eq. 4.2, as it gets smaller any relative changes in efficiency are dwarfed by the magnitude of the efficiency in general. A similar reasoning explains why the error bars in the efficiency plots change relative size to each other in the MDA plots. When errors are propagated the efficiency is squared in the denominator of the MDA error. This causes the relatively high efficiencies at slower speeds to result in small errors in MDA and the exact opposite at faster speeds.

4.4 Summary

Previous efforts in modeling and laboratory-scale trials show that detector performance is tightly coupled to detector speed, (Falkner & Marianno, in prep 2018a, in prep 2018b). As detector speed increases, the performance, as measured by efficiency, drops as represented in the M4PL curve. While this M4PL relationship held true both in a modeling and laboratory setting, the question remained of how applicable or valid it is to 'real-world' environments.

Field-survey plans are subject to regulatory requirements, time constraints and cost considerations, both in terms of detector investment and worker-time. Being able to better design a survey by considering how speed might affect those considerations would allow surveyors to verify their chosen detector works for their surveying needs, improves survey plans to better achieve the results they are seeking, or determine the best performance given the constraints within which they must operate.

Therefore, to seek to address whether the M4PL is scalable to the real-world environment, data was gathered from three systems: a truck system, a rotary-wing system, and a fixed-wing system. These experimental setups were then modeled via MCNP as was done in prior research, (Falkner & Marianno, in prep 2018a). Data from both the field-trials and simulations were compared and evaluated against the M4PL relationship as well as its associated minimum detectable

activity (MDA) curve, (Falkner & Marianno, in prep 2018a).

The M4PL fits both the experimental and simulated results, although the simulated results exhibited a higher degree of fit to the M4PL and its associated MDA plot than did the experimental results. One explanation for this is the lateral offset of the count location relative to the source. Another explanation is the height difference between count location and the simulated height of the detector. As these two values deviate from the modeled parameters the divergence between results will increase.

Ultimately, the MDA curve, as calculated using the validated M4PL curve, will be what is most relevant to those designing and conducting field-surveys. For a very short window the change in MDA for surveys will not impact the survey results significantly. If an operator is concerned with meeting regulatory requirements for MDA and they plan to operate at speeds beyond this threshold, they would be well-advised to consider their operational speed when designing their survey plan. Conversely, if survey speed is dictated by operational constraints, surveyors can utilize this MDA model to determine whether their detection system is a proper fit for the survey parameters.

5. CONCLUSION

Radiological surveying occurs in a wide variety of situations with multiple applications. These include laboratory assessments of reference sources, decommissioning surveys performed to meet regulatory requirements, and identifying source locations and concentrations in the field via vehicle or aircraft mounted systems. While standards for performing these surveys have been generally outlined a relationship coupling detector performance to its speed has not been identified, (U.S. NRC, 2000). One measure of a detector's performance is the minimum detectable activity (MDA) that it can achieve. MDA is the amount of activity above which a detector can observe with statistical confidence, Eq. 5.1. L_D is the limit of a detection, the number of counts above which a source is determined to have been detected. Y is the yield of the radionuclide in question. T is the integration time of the count performed. ϵ is the detector's efficiency. It is the dependence of efficiency, and ultimately MDA, on speed that was the focus of this research.

$$MDA = \frac{L_D}{Y \epsilon T} \tag{5.1}$$

It has been known for some time that the efficiency of a moving detector can be improved by slowing the speed of travel. The effect of speed on detector efficiency was mentioned in the Multi-Agency Radiation Survey and Site Investigation Manual (MARSSIM) for conducting environmental site surveys for the decommissioning of facilities, (U.S. NRC, 2000). Marianno identified the phenomenon in his data when evaluating the performance of a Field Instrument for the Detection of Low-Energy Radiation, (Marianno et al., 2000; Marianno, 2015). Schroettner, et. al., sought to address a similar problem through varying the integration speed, (Schroettner et al., 2009). Their approach was for a source traveling through a stationary portal monitor but is analogous to a moving detector past a stationary source due to reciprocity. However, the relationship itself between speed and efficiency has not been quantified until recently, (Falkner

& Marianno, in prep 2018a).

Efficiency is the combination of how many photons impact the detector (geometric efficiency) and how many of the photons that impact the detector interact and produce a signal inside the detector (intrinsic efficiency). Under typical survey conditions intrinsic efficiency is unchanging. This research showed how geometric efficiency affects MDA as a function of speed. Geometric efficiency can be calculated by solid angle of the detector. Solid angle is the angle subtended by an object from a point. In this research the source is the point and the detector is the object. MCNP results were correlated to solid angle calculations using point and line sources. The solid angle results were then fitted with a model to calculate values for any speed.

The first part of this research derived the relationship between detector efficiency and its speed. First a link between a detector's solid angle and its efficiency was established. This was accomplished by calculating the solid angle for various locations around a right circular cylinder and comparing to similarly modeled efficiencies. The purpose of this step was to confirm that solid angle is the driving factor in detector efficiency and that the detector properties are not influenced by source location. A link between a detector's efficiency and its speed was then established. This was accomplished by modeling detector efficiency at various speeds as it passed a source location. The purpose of this step was to reproduce the previously observed phenomenon. The model explaining the relationship between efficiency and speed was then defined, Eq. 5.2. This relationship is a modified four parameter logistic function (M4PL). In this function the speed of the detector is x, the maximum efficiency is A, the minimum efficiency is D, the slope of the equation is B, and the speed at which the efficiency is half that of the maximum is C.

$$y = D + \frac{A - D}{1 + \left(\frac{x}{C}\right)^B} \tag{5.2}$$

The second part of this research verified under laboratory conditions that the M4PL holds

for the detection system modeled. This was done in a laboratory first so that confounders such as variable background or nuisance sources could be minimized and that detection scheme parameters such as detector speed and orientation could be tightly controlled. Confounders here includes variable backgrounds, presence of multiple sources, and presence of excess attenuators (tall grass, shrubs, trees, walls, buildings, etc.) or terrain (broken soil, undulating hills, culverts, etc.) that would inhibit an isotropic source. A robotic system was used to perform all laboratory trials. This allowed for reproducing consistent trial conditions for the duration of the study. Most critically this included operating at a consistent desired speed for each trial but it also allowed for detector to be held in the same place relative to the robot for every trial. This allowed the trial results to be as consistent to the modeling as possible. The parameters held constant from trial to trial included track length, radionuclide selected as a source, source location, background, detector height, and integration time. Track length was critical because it was used, along with precise timing of each trial, as the means of determining trial speed. The source location and detector height were defined by the previously modeled parameters. The parameters that varied from trial to trial included speed and source strength. Source strength was varied to provide an alternate means of verifying model results. The speed was obviously varied because it was the parameter of interest in this research.

To validate the M4PL model under real world conditions data was gathered from three systems, a truck system, a rotary-wing system, and a fixed-wing system. The truck system was a single slab 2x4x16 detector oriented with the flat paddle face of the detector towards the source. The rotary-wing system was 12 of the same type of detectors mounted in 4 pods around the exterior of the aircraft. The fixed-wing system was 8 of the same type of detectors mounted in 2 cases in the interior of the aircraft. Both the rotary-wing and fixed-wing detectors were oriented so that the flat faces were aimed towards the ground. Data from the three systems were gathered on different dates. Each vehicle was operated in an oval track manner around their respective stationary point sources. Gross peak, net peak, and total efficiency were calculated for each

trial. The efficiencies of these systems was modeled and simulation results were compared to experimental data. As expected the efficiency of the detector is highly correlated to its solid angle. Additionally, the previously observed phenomenon of decreasing efficiency with increasing speed was reproduced in the simulation results. This indicates that detector properties do not vary over the conditions of interest. Thus solid angle explains the effect of speed on efficiency.

The M4PL model begins with a region of relatively high efficiency and ends with a region of relatively low efficiency. In between is a transition region of decreasing efficiency. This decrease is gradual at first, quickly steepens, and then shallows out. This general shape was observed for all modeled systems. Experimental data for all systems agreed with their respective model results. The degree of agreement was highest for the laboratory data and lowest for the aerial data owing to the size of the detector, distance from the source, and complexity of the overall survey environment.

The M4PL was used to develop a relationship between speed and MDA. In general the MDA curve starts low and as speed increases rises. The slope of the MDA curve starts shallowly at first but very quickly becomes quite sharp. The data points from this research match the modeled fit very well. Roughly speaking, the change in MDA for surveys conducted at the lower speeds will not impact the survey results significantly. If an operator is concerned with meeting regulatory requirements for MDA and they plan to operate at at higher speeds, they would be well-advised to consider this plot when designing their survey plan. Conversely, if survey speed is dictated by operational constraints, surveyors can consult this MDA model to determine whether their detection system is a proper fit for the survey parameters.

There are three uses of the M4PL model. The first is to verify the accuracy of current survey plans. The second is to optimize survey plans for speed and accuracy. The third is to identify limits of detection accuracy based on operational speed. This foundational relationship has the potential to improve detector performance in many large and small applications for both the academic and operational fields.

REFERENCES

Abelquist, E. W., & Brown, W. S. (1999). Estimating minimum detectable concentrations achievable while scanning building surfaces and land areas. *Health physics*, *76*(1).

Alecksen, T., & Whicker, R. (2016). Scan MDCs for GPS-Based Gamma Radiation Systems. *Health Physics*, *111*(2), S123-S132.

Altshuler, B., & Pasternack, B. (1963). Statistical measures of the lower limit of detection of a radioactivity counter. *Health Physics*, *9*(3), 293–298.

AMS. (2018). Aerial Measuring System. Retrieved 17-Jan-2018, from `https://nnsa.energy.gov/aboutus/ourprograms/emergencyoperationscounterterrorism/respondingtoemergencies-0-0`

Ayaz-Maierhafer, B., & DeVol, T. A. (2007). Determination of absolute detection efficiencies for detectors of interest in homeland security. *Nuclear Instruments and Methods in Physics Research Section A: Accelerators, Spectrometers, Detectors and Associated Equipment*, *579*(1), 410–413.

Canberra Industries Inc. (2011). *Osprey mcaSDK/Communications* (1.0.1 ed.). Canberra Industries Inc.

Currie, L. (1968). Limits for Qualitative Detection and Quantitative Determination. *Anal. Chem.*, *40*(3), 586-593.

De Geer, L.-E. (2004). Currie detection limits in gamma-ray spectroscopy. *Applied radiation and isotopes*, *61*(2-3), 151–160.

EPA. (2018). Airborne Spectral Photometric Environmental Collection Technology. Retrieved 17-Jan-2018, from `https://www.epa.gov/emergency-response/aspect`

Falkner, J., & Marianno, C. (in prep 2018a). Modeling Minimum Detectable Activity as a

Function of Detector Velocity. *unpublished*.

Falkner, J., & Marianno, C. (in prep 2018b). Experimentally Verifying Minimum Detectable Activity to Detector Velocity Relationship. *unpublished*.

Gilmore, G. (2011). *Practical Gamma-ray Spectrometry* (2^{nd} ed.). John Wiley & Sons, Inc.

Goorley, T., James, M., Booth, T., Brown, F., Bull, J., Cox, L., ... others (2012). Initial MCNP6 Release Overview. *Nuclear Technology*, *180*(3), 298–315.

Holl, I., Lorenz, E., & Mageras, G. (1988). A Measurement Of The Light Yield Of Common Inorganic Scintillators. *IEEE Transactions on Nuclear Science*, *35*(1), 105-109.

Knoll, G. (2010). *Radiation Detection and Measurement* (4^{th} ed.). John Wiley & Sons, Inc.

Kramer, G. H., Burns, L. C., & Guerriere, S. (2002). Monte carlo simulation of a scanning detector whole body counter and the effect of bomab phantom size on the calibration. *Health physics*, *83*(4), 526–533.

Lepel, E., Geelhood, B., Hensley, W., & Quam, W. (1998). A field-deployable, aircraft-mounted sensor for the environmental survey of radionuclides. *Journal of radioanalytical and nuclear chemistry*, *233*(1-2), 211b–215.

Marianno, C. (2015). Signal Processing and its Effect on Scanning Efficiencies for a Field Instrument for Detecting Low-Energy Radiation. *Health Physics*, *109*, 78-83.

Marianno, C., Higley, K., & Palmer, T. (2000). Theoretical Efficiencies for a FIDLER Scanning Hot Particle Contamination. *Radiat Protect Management J Applied Health Phys*, *17*, 31-34.

Masket, A., Macklin, R., & Schmitt, H. (1956). *Tables of Solid Angles and Activations* (ORNL-2170 ed.). Technical Information Service Extension, Oak Ridge, TN.

Monarch Instruments. (1995). *Remote Optical Sensor* (1071-4854-118R ed.). Monarch Instruments.

Pöllänen, R., Toivonen, H., Peräjärvi, K., Karhunen, T., Ilander, T., Lehtinen, J., ... Juusela, M. (2009). Radiation surveillance using an unmanned aerial vehicle. *Applied radiation and*

isotopes, *67*(2), 340–344.

Rossum, G. (2015). *Python 2.7.10 reference manual* (Tech. Rep.).

Rossum, G. (2017). *Python 3.6.1 reference manual* (Tech. Rep.).

RSI. (2018). Radiation Solutions, Inc. Retrieved 06-Jan-2018, from `http://www.radiationsolutions.ca/airborne/`

Runkle, R. C., Mercier, T. M., Anderson, K. K., & Carlson, D. K. (2005). Point source detection and characterization for vehicle radiation portal monitors. *IEEE transactions on nuclear science*, *52*(6), 3020–3025.

Sakai, E. (1987). Recent Measurements On Scintillator-Photodetector Systems. *IEEE Transactions on Nuclear Science*, *NS-34*(1), 418-422.

Schroettner, T., Kindl, P., & Presle, G. (2009). Enhancing Sensitivity of Portal Monitoring at Varying Transit Speeds. *App. Rad. and Iso.*, *67*, 1878-1886. (with permission from Elsevier)

Sittampalam, G., Coussens, N., Brimacombe, K., et al. (2004). *Assay Guidance Manual [Internet]*. National Center for Advancing Translational Sciences.

Super Droid Robots. (2017). Super Droid Robots. Retrieved 20-Mar-2017, from `http://www.superdroidrobots.com/shop/item.aspx/lt2-tracked-atr-robot-platform/1513/`

Team, Q. D. (2017). *Qgis geographic information system* (Tech. Rep.).

U.S. NRC. (2000). MARSSIM. *NUREG-1575, Rev*, *1*.

Warner, G., & Oliver, R. (1966). A whole-body counter for clinical measurements utilizing theshadow shield'technique. *Physics in Medicine & Biology*, *11*(1), 83.

Whicker, R., Cartier, P., Cain, J., Milmine, K., & Griffin, M. (2008). Radiological site characterizations: gamma surveys, gamma/226ra correlations, and related spatial analysis techniques. *Health physics*, *95*(5), S180–S189.

APPENDIX A

DATA TABLES

A.1 Coordinate locations for point source modeling

Table A.1: Coordinate locations for point sources used in modeling.

Trial	ρ	z
ex0	-2	4
ex1	-2	3
ex2	-5	0
ex3	-5	-0.5
ex4	-5	4
I1	0	1
I2	0	2
I3	0	3
I4	0	4
I5	0	5
II1	-2	1
II2	-3	1
II3	-4	1
II4	-5	1
II5	-6	1
III1	-2	-1
III2	-3	-1
III3	-4	-1
III4	-5	-1
III5	-6	-1

A.2 Masket, Python, and MCNP point source results

Table A.2: Modeling results from Masket table, MCNP simulations, and Python calculations for point sources.

Trial	Masket Results	Python Results	MCNP Results	Python/Masket Ratio	MCNP/Python Ratio
ex0	0.159548 ± 0.000001	0.160016 ± 0.000480	0.012663 ± 0.000035	1.002933 ± 0.003009	0.079133 ± 0.000325
ex1	0.240063 ± 0.000001	0.240738 ± 0.000722	0.019048 ± 0.000044	1.002812 ± 0.003008	0.079125 ± 0.000299
ex2	0.173954 ± 0.000001	0.174061 ± 0.000522	0.013855 ± 0.000037	1.000615 ± 0.003002	0.079599 ± 0.000321
ex3	0.184067 ± 0.000001	0.184189 ± 0.000553	0.014657 ± 0.000038	1.000664 ± 0.003002	0.079577 ± 0.000316
ex4	0.100254 ± 0.000001	0.100462 ± 0.000301	0.007921 ± 0.000028	1.002077 ± 0.003006	0.078848 ± 0.000363
I.1	1.840300 ± 0.000001	1.840302 ± 0.005521	0.146365 ± 0.000117	1.000001 ± 0.003000	0.079533 ± 0.000247
I.2	0.663334 ± 0.000001	0.663334 ± 0.001990	0.052834 ± 0.000069	0.999999 ± 0.003000	0.079650 ± 0.000260
I.3	0.322432 ± 0.000001	0.322432 ± 0.000967	0.025647 ± 0.000049	1.000001 ± 0.003000	0.079542 ± 0.000282
I.4	0.187600 ± 0.000001	0.187600 ± 0.000563	0.014943 ± 0.000039	1.000001 ± 0.003000	0.079652 ± 0.000316
I.5	0.122015 ± 0.000001	0.122015 ± 0.000366	0.009729 ± 0.000031	1.000002 ± 0.003000	0.079732 ± 0.000350
II.1	0.609786 ± 0.000001	0.610908 ± 0.001833	0.048345 ± 0.000068	1.001840 ± 0.003006	0.079136 ± 0.000262
II.2	0.374393 ± 0.000001	0.374930 ± 0.001125	0.029674 ± 0.000053	1.001434 ± 0.003004	0.079146 ± 0.000277
II.3	0.242704 ± 0.000001	0.243000 ± 0.000729	0.019260 ± 0.000044	1.001218 ± 0.003004	0.079258 ± 0.000300
II.4	0.165765 ± 0.000001	0.165942 ± 0.000498	0.013147 ± 0.000035	1.001068 ± 0.003003	0.079227 ± 0.000320
II.5	0.118673 ± 0.000001	0.118784 ± 0.000356	0.009448 ± 0.000030	1.000937 ± 0.003003	0.079537 ± 0.000349
III.1	1.389954 ± 0.000001	1.391837 ± 0.004176	0.110487 ± 0.000099	1.001355 ± 0.003004	0.079382 ± 0.000249
III.2	0.573002 ± 0.000001	0.573602 ± 0.001721	0.045642 ± 0.000064	1.001047 ± 0.003003	0.079570 ± 0.000263
III.3	0.304482 ± 0.000001	0.304736 ± 0.000914	0.024252 ± 0.000049	1.000834 ± 0.003003	0.079584 ± 0.000287
III.4	0.187641 ± 0.000001	0.187770 ± 0.000563	0.014916 ± 0.000039	1.000686 ± 0.003002	0.079439 ± 0.000315
III.5	0.126946 ± 0.000001	0.127020 ± 0.000381	0.010083 ± 0.000031	1.000583 ± 0.003002	0.079384 ± 0.000342
			Average	1.001005 ± 0.003003	0.079403 ± 0.000304

A.3 Python and MCNP line source results

Table A.3: Modeling results from MCNP simulations and Python calculations for line sources.

Speed (cm s^{-1})	Python Results (Ω)	MCNP Results ($\frac{\text{ph counted}}{\text{ph emitted}}$)	MCNP to Python Ratio
0	0.193375 ± 0.000580	0.018380 ± 0.000132	0.079608 ± 0.000311
10	0.179388 ± 0.000538	0.017835 ± 0.000132	0.079715 ± 0.000317
20	0.161888 ± 0.000486	0.015939 ± 0.000126	0.079685 ± 0.000328
30	0.142015 ± 0.000426	0.014181 ± 0.000118	0.080273 ± 0.000335
40	0.123846 ± 0.000372	0.012614 ± 0.000111	0.080745 ± 0.000352
50	0.108638 ± 0.000326	0.011295 ± 0.000106	0.080082 ± 0.000365
60	0.096214 ± 0.000289	0.009983 ± 0.000100	0.080030 ± 0.000376
70	0.086066 ± 0.000258	0.008912 ± 0.000094	0.080171 ± 0.000388
80	0.077720 ± 0.000233	0.008151 ± 0.000090	0.079774 ± 0.000400
90	0.070765 ± 0.000212	0.007404 ± 0.000086	0.080548 ± 0.000413
100	0.064895 ± 0.000195	0.006761 ± 0.000082	0.080129 ± 0.000428
		Average	0.080069 ± 0.000111

A.4 Source Speed Cohort Linear Fit Parameters

Table A.4: Linear fit parameters for various robot speeds as a function of number of sources counted.

Speed (cm^{-1})	Slope	Intercept
0.00 ± 0.00	471.12 ± 3.32	-7.84 ± 10.05
19.08 ± 0.68	369.37 ± 2.53	-0.66 ± 7.67
39.90 ± 1.04	284.74 ± 2.50	-7.47 ± 7.56
63.58 ± 3.50	206.46 ± 3.08	-1.91 ± 9.33
86.28 ± 0.09	152.50 ± 2.63	-9.22 ± 7.95
120.67 ± 0.14	118.12 ± 1.33	-5.62 ± 4.01

Modified 4 Parameter Logistic Function Parameters

Table A.5: Parameters of the 4-Parameter Logistic Function used to fit the various model results.

Setup	A	B	C	D
MCS	1.26E-4 $\pm$ 2.38E-7	1.91E0 $\pm$ 3.71E-2	1.57E3 $\pm$ 3.64E1	2.39E-5 $\pm$ 2.18E-6
EPA Low	2.47E-5 $\pm$ 1.56E-7	1.68E0 $\pm$ 3.68E-1	8.66E2 $\pm$ 3.65E3	-1.12E-4 $\pm$ 8.40E-4
EPA High	1.10E-5 $\pm$ 4.83E-8	3.17E0 $\pm$ 8.04E-1	1.18E2 $\pm$ 2.17E1	8.74E-6 $\pm$ 6.10E-7
AMS Low	2.83E-5 $\pm$ 2.00E-7	2.31E0 $\pm$ 3.53E-1	1.31E2 $\pm$ 2.50E1	1.08E-5 $\pm$ 1.38E-6
AMS High	1.26E-5 $\pm$ 1.35E-7	2.70E0 $\pm$ 1.01E0	1.09E2 $\pm$ 3.23E1	8.85E-6 $\pm$ 1.38E-6

A.5 Robot Source Data

Table A.6: Gross peak counts, net peak counts, and efficiencies for robot source data.

Sources	Throttle	Gross Peak	Net Peak	Efficiency
1	0	6.18E+02 ± 2.40E+01	4.70E+02 ± 2.69E+01	1.67E-02 ± 9.53E-04
1	50	5.16E+02 ± 2.27E+01	3.68E+02 ± 2.58E+01	1.30E-02 ± 9.13E-04
1	75	4.09E+02 ± 2.02E+01	2.61E+02 ± 2.36E+01	9.24E-03 ± 8.36E-04
1	100	3.48E+02 ± 1.87E+01	2.00E+02 ± 2.23E+01	7.10E-03 ± 7.90E-04
1	125	2.89E+02 ± 1.70E+01	1.41E+02 ± 2.09E+01	5.00E-03 ± 7.41E-04
1	150	2.56E+02 ± 1.60E+01	1.08E+02 ± 2.01E+01	3.81E-03 ± 7.12E-04
2	0	1.06E+03 ± 3.22E+01	9.16E+02 ± 3.44E+01	1.62E-02 ± 6.09E-04
2	50	8.93E+02 ± 2.99E+01	7.45E+02 ± 3.23E+01	1.32E-02 ± 5.72E-04
2	75	7.18E+02 ± 2.68E+01	5.70E+02 ± 2.94E+01	1.01E-02 ± 5.22E-04
2	100	5.73E+02 ± 2.39E+01	4.25E+02 ± 2.68E+01	7.53E-03 ± 4.76E-04
2	125	4.42E+02 ± 2.10E+01	2.94E+02 ± 2.43E+01	5.21E-03 ± 4.30E-04
2	150	3.77E+02 ± 1.94E+01	2.29E+02 ± 2.29E+01	4.06E-03 ± 4.06E-04
3	0	1.54E+03 ± 3.88E+01	1.39E+03 ± 4.07E+01	1.65E-02 ± 4.81E-04
3	50	1.25E+03 ± 3.54E+01	1.11E+03 ± 3.74E+01	1.31E-02 ± 4.42E-04
3	75	9.99E+02 ± 3.16E+01	8.51E+02 ± 3.39E+01	1.01E-02 ± 4.00E-04
3	100	7.55E+02 ± 2.75E+01	6.07E+02 ± 3.01E+01	7.18E-03 ± 3.55E-04
3	125	5.83E+02 ± 2.41E+01	4.35E+02 ± 2.70E+01	5.14E-03 ± 3.20E-04
3	150	4.92E+02 ± 2.22E+01	3.44E+02 ± 2.53E+01	4.07E-03 ± 2.99E-04
4	0	2.04E+03 ± 4.42E+01	1.89E+03 ± 4.58E+01	1.68E-02 ± 4.06E-04
4	50	1.61E+03 ± 4.01E+01	1.46E+03 ± 4.19E+01	1.29E-02 ± 3.71E-04
4	75	1.28E+03 ± 3.57E+01	1.13E+03 ± 3.77E+01	9.99E-03 ± 3.34E-04
4	100	9.58E+02 ± 3.09E+01	8.10E+02 ± 3.33E+01	7.18E-03 ± 2.95E-04
4	125	7.43E+02 ± 2.73E+01	5.95E+02 ± 2.98E+01	5.28E-03 ± 2.65E-04
4	150	6.21E+02 ± 2.49E+01	4.73E+02 ± 2.77E+01	4.20E-03 ± 2.46E-04
5	0	2.50E+03 ± 4.84E+01	2.35E+03 ± 4.99E+01	1.67E-02 ± 3.54E-04
5	50	2.01E+03 ± 4.48E+01	1.86E+03 ± 4.64E+01	1.32E-02 ± 3.29E-04
5	75	1.56E+03 ± 3.96E+01	1.42E+03 ± 4.14E+01	1.00E-02 ± 2.93E-04
5	100	1.19E+03 ± 3.45E+01	1.04E+03 ± 3.66E+01	7.40E-03 ± 2.59E-04
5	125	9.15E+02 ± 3.02E+01	7.67E+02 ± 3.26E+01	5.44E-03 ± 2.31E-04
5	150	7.32E+02 ± 2.71E+01	5.84E+02 ± 2.97E+01	4.14E-03 ± 2.10E-04

APPENDIX B

CODES

B.1 Sample MCNP Input Deck for 2x2 Detector

MDA Solid Angle Test 1-1

C

C Surface Cards

1 1 -3.67 -101 IMP:P=1

2 2 -2.70 +101 -102 IMP:P=1

900 0 +102 -999 IMP:P=1

999 0 +999 IMP:P=0

C Cell Cards

101 RCC 0 0 0.16 0 0 5.08 2.54

102 RCC 0 0 0 0 0 5.40 2.85

999 SO 1000

C Physics Cards

MODE P

SDEF POS=0 0 -10 AXS=1 0 0 EXT=D1 ERG=0.662

SI1 -10 10 $Xmin to Xmax for line source

SP1 -21 0 $uniform sampling on line Here x$\hat{0}$

F8:P 1

E8 0 1E-04 0.05 0.10 0.15 0.20 0.25 0.30 0.35 0.40 0.45 &

0.50 0.55 0.60 0.65 0.655 0.656 0.657 0.658 0.659 0.660 &

0.661 0.662 0.663 0.664 0.665 0.670 0.70 0.75 0.80 0.85 &

0.90 0.95 1.0 1.05 1.10 1.15 1.20 1.25 1.30 1.35 1.40 1.45 1.50 1.55

FT8 GEB -0.00789 0.06769 0.21159

M1 11000 0.5 53000 0.5

M2 13000 1.0

NPS 1e7

B.2 Sample MCNP Input Deck for RSL Detector

MDA Solid Angle Test 1-1

C

C Surface Cards

1 1 -3.67 -101 IMP:P=1

2 2 -3.97 +101 -102 IMP:P=1

3 3 -2.70 +102 -103 IMP:P=1

4 4 -1.80 -104 IMP:P=1

900 0 +103 +104 -999 IMP:P=1

999 0 +999 IMP:P=0

C Cell Cards

101 RCC 0 0 0.16 0 0 5.08 2.54

102 RCC 0 0 0.05 0 0 5.30 2.805

103 RCC 0 0 0.00 0 0 5.40 2.855

104 RPP -100 100 -100 100 -15.72 -10.01

999 SO 1000

C Physics Cards

MODE P

SDEF POS=0 0 -10 AXS=1 0 0 EXT=D1 ERG=0.662

SI1 -50 50 $XmintoXmaxforlinesource$

$SP1 - 210$ uniform sampling on line Here x$\hat{0}$

F8:P 1

E8 0 2

M1 11000 0.5 53000 0.5

M2 8000 0.4 13000 0.6

M3 13000 1.0

M4 8000 0.663062 13000 0.003916 14000 0.323140 20000 0.007272 26000 0.002610

NPS 1e6

B.3 Python script used to calculate solid angle of a right circular cylinder

```
import numpy as np
import matplotlib.pyplot as plt

r0 = np.linspace(0.0, 0.9, 10).tolist()
r1 = [0.95]
r2 = np.linspace(1.0, 6.2, 53).tolist()
r3 = np.linspace(6.5, 16, 20).tolist()
r4 = np.linspace(17, 36, 20).tolist()
r5 = np.linspace(40, 160, 24).tolist()
r6 = np.linspace(50, 2000, 40).tolist()
r = r0 + r1 + r2 + r3 + r4 + r5

r2 = r0 + r1 + r2 + r3 + r4 + r6
```

```
det_rad = 2.54
det_len = 5.08
src_ht = 10

src_rho = [-i for i in r[::-1][:-1]] + r

parking_rho = [-i for i in r2[::-1][:-1]] + r2
parking_ht = 177.165

trials = [[2,4,1,2],
          [2,3,1,2],
          [5,0,1,2],
          [5,-0.5,1,2],
          [5,4,1,2],
          [0,1,1,2],
          [0,2,1,2],
          [0,3,1,2],
          [0,4,1,2],
          [0,5,1,2],
          [2,1,1,2],
          [3,1,1,2],
          [4,1,1,2],
          [5,1,1,2],
          [6,1,1,2],
          [2,-1,1,2],
          [3,-1,1,2],
          [4,-1,1,2],
          [5,-1,1,2],
          [6,-1,1,2]]


def S1(x, p):
    """
    Taylor Expansion of rho * cos(phi) + np.sqrt(1 - rho ** 2 * sin(phi) ** 2)
    """
    s1 = p + 1
    s2 = (1/2)*(p*(p + 1))*x**2
    s3 = (1/24)*(-3*p**4 + 4*p**2 + p)*x**4
    s4 = (1/720)*(p*(45*p**5 - 60*p**3 + 16*p + 1))*x**6
```

```
    s5 = ((-1575*p**8 + 2520*p**6 - 1008*p**4 + 64*p**2 + p)*x**8)/40320
    s6 = ((p*(99225*p**9 - 189000*p**7 + 105840*p**5 - 16320*p**3 + 256*p + 1))*x**10)/3628800
    s7 = (p*(-9823275*p**11 + 21829500*p**9 - 15800400*p**7 + 4055040*p**5 - 261888*p**3 +/
         1024*p + 1)*x**12)/479001600
    s8 = (-(33*p**14)/2048 + (21*p**12)/512 - (7*p**10)/192 + (5*p**8)/378 - (13*p**6)/7560 +/
         p**4/20790 - (2*p**2)/42567525 - p/87178291200)*x**14
    s9 = (-(429*p**16)/32768 + (77*p**14)/2048 - (203*p**12)/5120 + (43*p**10)/2304 -\
         (457*p**8)/120960 + (31*p**6)/118800 - (5461*p**4)/1702701000 + p**2/1277025750 +/
         p/20922789888000)*x**16

    return s1 - s2 + s3 - s4 + s5 - s6 + s7 + s8 + s9


def S2(x, p):
    """
    Taylor Expansion of rho * cos(phi) - np.sqrt(1 - rho ** 2 * sin(phi) ** 2)
    """
    s1 = (p - 1)
    s2 = (1/2)*(p - 1)*p*x**2
    s3 = (1/24)*p*(3*p**3 - 4*p + 1)*x**4
    s4 = (1/720)*p*(45*p**5 - 60*p**3 + 16*p - 1)*x**6
    s5 = (p*(1575*p**7 - 2520*p**5 + 1008*p**3 - 64*p + 1)*x**8)/40320
    s6 = (p*(99225*p**9 - 189000*p**7 + 105840*p**5 - 16320*p**3 + 256*p - 1)*x**10)/3628800
    s7 = (p*(9823275*p**11 - 21829500*p**9 + 15800400*p**7 - 4055040*p**5 + 261888*p**3 -/
         1024*p + 1)*x**12)/479001600
    s8 = ((33*p**14)/2048 - (21*p**12)/512 + (7*p**10)/192 - (5*p**8)/378 + (13*p**6)/7560 -/
         p**4/20790 + (2*p**2)/42567525 - p/87178291200)*x**14
    s9 = ((429*p**16)/32768 - (77*p**14)/2048 + (203*p**12)/5120 - (43*p**10)/2304 +/
         (457*p**8)/120960 - (31*p**6)/118800 + (5461*p**4)/1702701000 - p**2/1277025750 +/
         p/20922789888000)*x**16

    return s1 + s2 + s3 + s4 + s5 + s6 + s7 + s8 + s9


def T1(x, p):
    #return p * np.cos(x) + np.sqrt(1 - p**2 * np.sin(x)**2)
    return p * np.cos(x) + (1 - p**2 * np.sin(x)**2)**0.5
```

```
def case1(phi, h, p):
    """
    This is the solid angle contributed by the face of the cylinder
    when the source is inside the radius.
    """
    #return 1 / np.sqrt(h ** 2 + T1(phi, p) ** 2)
    return 1 / (h ** 2 + T1(phi, p) ** 2)**0.5


def case2(phi, h, p):
    #return 1 / np.sqrt(h ** 2 + 4 * np.cos(phi) ** 2)
    return 1 / (h ** 2 + 4 * np.cos(phi) ** 2)**0.5


def case3(phi, h, p):
    #return 1 / np.sqrt(h ** 2 + S2(phi, p) ** 2) - 1 / np.sqrt(h ** 2 + S1(phi, p) ** 2)
    return 1 / (h ** 2 + S2(phi, p) ** 2)**0.5 - 1 / (h ** 2 + S1(phi, p) ** 2)**0.5


def case4(phi, h, p):
    """
    This is the solid angle contributed by the side of the cylinder
    when the source is inside the radius.
    """
    #return 1 / np.sqrt(h ** 2 + S2(phi, p) ** 2)
    return 1 / (h ** 2 + S2(phi, p) ** 2)**0.5


def integrate(f, a, b, h, p, N=10000000):
    x = np.linspace(a, b, N)
    fx = f(x, h, p)
    area = np.sum(fx)*(b-a)/N
    return area


def solid_angle(rho, z, r, l):
    rho = abs(rho)
    z = z / r
    l = l / r
```

```
    if (rho < 1) and (-1 < z < 0):
        print("This source location is inside the detector")
    elif (rho <= 1) and ((z >= 0) or (z < -1)):
        if z < -1:
            z = abs(z) - 1
        ans = 2 * np.pi - 2 * z * integrate(f=case1, a=0, b=np.pi, h=z, p=rho)
        return float(format(ans, '0.6f'))

    elif (rho > 1) and ((z > 0) or (z < -1)):
        if z < -1:
            z = abs(z)
        part1 = 2 * z * integrate(f=case3, a=0, b=np.arcsin(1/rho), h=z, p=rho)
        part2 = 2 * (z+1) * integrate(f=case4, a=0, b=np.arcsin(1/rho), h=z+1, p=rho)
        part3 = 2 * z * integrate(f=case4, a=0, b=np.arcsin(1/rho), h=z, p=rho)
        ans = part1 + part2 - part3
        return float(format(ans, '0.6f'))

    elif (rho > 1) and (-1 < z <= 0):
        z = abs(z)
        part1 = 2 * z * integrate(f=case4, a=0, b=np.arcsin(1/rho), h=z, p=rho)
        part2 = 2 * (1-z) * integrate(f=case4, a=0, b=np.arcsin(1/rho), h=1-z, p=rho)
        ans = part1 + part2
        return float(format(ans, '0.6f'))

    else:
        print("I don't know what you want")

if __name__ == '__main__':

    """solid_angles = []
    for trial in trials[0:4]:
        ans = solid_angle(trial[0], trial[1], trial[2], trial[3])
        trial.append(ans)
        solid_angles.append(ans)"""

    """distance_test = []
    tests = [[r, 0, 1, 2] for r in np.linspace(1,1001, 101)]
    for test in tests:
```

```
    #ans = solid_angle(test[0], test[1], test[2], test[3])
    ans = solid_angle(*test)
    test.append(ans)
    distance_test.append(ans)"""

"""solid_angles = []
for r in src_rho:
    ans = solid_angle(r, src_ht, det_rad, det_len)
    solid_angles.append([r, src_ht, det_rad, det_len, ans])


with open('solid_angles_masket_rad={0}_len={1}_ht={2}.txt'.format(det_rad,
          det_len, src_ht), 'w') as f:
    f.write('det_rad,det_len,src_ht \n')
    f.write("{0}, {1}, {2} \n".format(det_rad, det_len, src_ht))
    f.write('radii,solid_angle')
    for i in solid_angles:
        f.write('\n')
        f.write('{0}, {1}'.format(i[0], i[-1]))"""

"""test_a, test_x, test_y = integrate(case3, 0, np.arcsin(1/5), 2, 5, 10)
fig, ax = plt.subplots()
ax.bar(test_x, test_y, test_x[1]-test_x[0], facecolor='gray', edgecolor='black', linewidth=1.0)
plt.xlabel('$\phi$')
plt.ylabel('Value')
plt.title('Riemann Approximation')"""

"""solid_angles = []
for i in parking_rho:
    ans = solid_angle(i, parking_ht, det_rad, det_len)
    solid_angles.append([i, parking_ht, det_rad, det_len, ans])


with open('solid_angles_masket_rad={0}_len={1}_ht={2}.txt'.format(det_rad,
          det_len, parking_ht), 'w') as f:
    f.write('det_rad,det_len,src_ht \n')
    f.write("{0}, {1}, {2} \n".format(det_rad, det_len, src_ht))
    f.write('radii,solid_angle')
    for i in solid_angles:
```

```
        f.write('\n')
        f.write('{0}, {1}'.format(i[0], i[-1]))"""
```

B.4 Python script used in MCS analysis

```
import pandas as pd
import numpy as np
import matplotlib.pyplot as plt
import scipy.optimize as opt


def angle_func(x, A, B, C, D):
#return 1 - ((A - D) / (1 + (x/C)**B) + D)
return D + (A - D) / (1 + (x/C) ** B)


def cust_mean(grp):
grp['mean'] = grp['option_value'].mean()
return grp


data = pd.read_csv('mcs_data.csv')

test_data = data[data.activity > 1].sample(5)


res_cols=['throttle', 'activity','trial_time','speed','ind_max','time_max','max_x','bkgd_cnts',
'currie_limit_cnt', 'currie_limit_1sec','net_peak', 'peak_sig', 'Detected']
results = pd.DataFrame(columns=res_cols)

for row in data.itertuples(index=True):

cnts = [1.002*int(c) for c in row.counts[1:-1].split(',')]
cnts_sigs = [c**0.5 for c in cnts]
ind_max = cnts.index(max(cnts))
max_time = ind_max * row.dwell_time

bkgd_cnts = cnts[10:60] + cnts[-60:-10]
```

```
bkgd_sigs = [np.sqrt(b) for b in bkgd_cnts]
bkgd_cnt = sum(bkgd_cnts) / len(bkgd_cnts)
bkgd_sig = np.sqrt(sum(bkgd_cnts))/len(bkgd_cnts)

currie_limit_cnt = bkgd_sig * 4.65 + 2.71
currie_limit_1sec = currie_limit_cnt * 50
net_cnts = [c - bkgd_cnt if c - bkgd_cnt > 0 else 0 for c in cnts]
net_sigs = [(a**2+bkgd_sig**2)**0.5 for a in cnts_sigs]

peak_cnts = net_cnts[ind_max-25:ind_max+25]
peak_sigs = [np.sqrt(p) for p in peak_cnts]
peak_cnt = 1.002*sum(peak_cnts)
peak_sig = 1.002*(sum([p**2 for p in peak_sigs]))**0.5

detected = True if peak_cnt - peak_sig > currie_limit_1sec else False

max_x = 606.36 * max_time / row.trial_time

holder = pd.DataFrame([[row.throttle, row.activity, row.trial_time, 606.36 / row.trial_time,
ind_max, max_time, max_x, bkgd_cnts, currie_limit_cnt, currie_limit_1sec, peak_cnt, peak_sig,
detected]], columns=res_cols)
results = results.append([holder], ignore_index=True)

avg_cols = ['throttle', 'activity', 'avg_trial_time', 'avg_speed', 'avg_max_time',
'avg_max_x', 'avg_net_peak', 'avg_eff', 'std_np', 'std_eff']
averages = pd.DataFrame(columns=avg_cols)



master_bkgd = [int(c) for c in data['counts'][(data['throttle'] == /
'\'centered\'') & (data['activity'] == 0)].tolist()[0][1:-1].split(',')]
bkgd_1s = 50 * master_bkgd

angle_opt = [0.0149, 1.5421, 52.5044, 0.0014]
angle_x = np.linspace(0, 120, 121)
angle_y = angle_func(angle_x, *angle_opt)

for a in 0, 1, 2, 3, 4, 5:
for t in '50', '75', '100', '125', '150', 'centered':
```

```
if t != 'centered':
avg_tt = results['trial_time'][(results['throttle'] == t) &/
(results['activity'] == a)].mean()
avg_sp = results['speed'][(results['throttle'] == t) &/
(results['activity'] == a)].mean()
avg_tm = results['time_max'][(results['throttle'] == t) &/
(results['activity'] == a)].mean()
avg_xm = results['max_x'][(results['throttle'] == t) &/
(results['activity'] == a)].mean()
avg_np = results['net_peak'][(results['throttle'] == t) &/
(results['activity'] == a)].mean()
std_np = results['net_peak'][(results['throttle'] == t) &/
(results['activity'] == a)].std()
if a == 0:
avg_eff = 0
std_eff = 0
else:
avg_eff = avg_np / (a * 33174.7 * 0.85)
std_eff = std_np / (a * 33174.7 * 0.85)

elif t == 'centered':
avg_tt = results['trial_time'][(results['throttle'] == t) &/
(results['activity'] == a)].mean()
avg_sp = 0
avg_tm = 'None'
avg_xm = 'None'
cnts = [int(c) for c in data['counts'][(data['throttle'] == '\'centered\'') &/
(data['activity'] == a)].tolist()[0][1:-1].split(',')]
avg_np = 50 * (np.mean(cnts) - np.mean(master_bkgd))
std_np = np.sqrt(avg_np)
if a == 0:
avg_eff = 0
std_eff = 0
else:
avg_eff = avg_np / (a * 33174.7 * 0.85)
std_eff = std_np / (a * 33174.7 * 0.85)

holder = pd.DataFrame([[t, a, avg_tt, avg_sp, avg_tm, avg_xm, avg_np,
avg_eff, std_np, std_eff]], columns=avg_cols)
```

```
averages = averages.append([holder], ignore_index=True)

combined_x = averages['avg_speed'][(averages['activity'] != 0)].tolist()[0:-1]
combined_y = [a / 1.0 for a in averages['avg_eff'][(averages['activity'] != 0)].tolist()[0:-1]]
combined_yerr = [a / 1.0 for a in /
[2 * y for y in averages['std_eff'][(averages['activity'] != 0)].tolist()[0:-1]]]

averages = averages[(averages['throttle'] != 'away') & (averages['throttle'] != 'toward')]

f, ax = plt.subplots()

ax.errorbar(combined_x, combined_y, yerr=combined_yerr, fmt='o', c='k', label='Robot Data')
ax.plot(angle_x, angle_y, c='k', label='Model Fit')
ax.legend()

plt.xlim([-5, 150])
plt.ylim([0, 0.02])
plt.xlabel('Speed (cm s$^{-1}$)')
plt.ylabel('Efficiency ($\epsilon$)')

f, ax = plt.subplots()

partial_results = averages[averages['activity'] == 0].sort_values('throttle', ascending=True)

x = partial_results['throttle'].tolist()
y = partial_results['avg_net_peak'].tolist()
yerr = partial_results['std_np'].tolist()

plt.errorbar(x=range(len(y)), y=y, yerr=[2*i for i in yerr],
linestyle='', c='k', marker='s', capsize=5, capthick=1)
plt.xticks(range(len(y)), x)
plt.xlabel('Throttle Setting')
plt.ylabel('Counts')
```